

Novel Implementations of Wideband Tightly Coupled Dipole Arrays for Wide-Angle Scanning

Dissertation

Presented in Partial Fulfillment of the Requirements for the Degree Doctor
of Philosophy in the Graduate School of The Ohio State University

By

Ersin Yetisir, B.S., M.S.

Graduate Program in Electrical and Computer Engineering

The Ohio State University

2015

Dissertation Committee:

John L. Volakis, Advisor

Nima Ghalichechian, Co-advisor

Chi-Chih Chen

Fernando L. Teixeira

© Copyright by

Ersin Yetisir

2015

Abstract

Ultra-wideband (UWB) antennas and arrays are essential for high data rate communications and for addressing spectrum congestion. Tightly coupled dipole arrays (TCDA) are of particular interest due to their low-profile, bandwidth and scanning range. But existing UWB ($>3:1$ bandwidth) arrays still suffer from limited scanning, particularly at angles beyond 45° from broadside. Almost all previous wideband TCDA have employed dielectric layers above the antenna aperture to improve scanning while maintaining impedance bandwidth. But even so, these UWB arrays have been limited to no more than 60° away from broadside.

In this work, we propose to replace the dielectric superstrate with frequency selective surfaces (FSS). In effect, the FSS is used to create an effective dielectric layer placed over the antenna array. FSS also enables anisotropic responses and more design freedom than conventional isotropic dielectric substrates. Another important aspect of the FSS is its ease of fabrication and low weight, both critical for mobile platforms (e.g. unmanned air vehicles), especially at lower microwave frequencies. Specifically, it can be fabricated using standard printed circuit technology and integrated on a single board with active radiating elements and feed lines.

In addition to the FSS superstrate, a modified version of the stripline-based folded Marchand balun is presented. As usual the balun serves to match the 50Ω coaxial cable to the high input impedance ($\sim 200\Omega$) at the terminals of array elements. Doing so, earlier

Wilkinson power dividers, which degrade efficiency during E -plane scanning, are eliminated. To verify the proposed array concept, 12x12 TCDA prototype was fabricated using the modified balun and the new FSS superstrate layer. The design and experimental data showed an impedance bandwidth of 6.1:1 with $VSWR < 3.2$. The latter VSWR was achieved even when scanning down to $\pm 60^\circ$ in the H -plane, $\pm 70^\circ$ in the D -plane and $\pm 75^\circ$ in the E -plane. All array components, including the FSS, radiating dipoles and the feed lines are placed on the same PCB, vertically oriented over the array ground plane, resulting in a low-cost and light-weight structure.

The effects of finite aperture sizes in presence of FSS or dielectric superstrates are also considered. Specifically, we compare the performance of finite TCDA with FSS or dielectric loading. The performance metric is beam pointing accuracy for moderate array sizes (~ 30 dBi gain) with various edge element terminations. It is shown that even terminating two unit cells at the array edges can provide effective suppression of edge-born waves and achieve excellent beam accuracy. This is the case when both the FSS elements and radiating dipoles are resistively loaded in the unit-cells along the aperture edges.

To my family

Acknowledgments

I would like to express my gratitude and respect for my advisor Prof. John L. Volakis. His constant support guided me throughout my time in ElectroScience Laboratory as a graduate student. His professional insight and ability to always see the big picture helped me become a researcher and engineering professional. I sincerely feel lucky to have him as my mentor. I would also like to thank Dr. Chi-Chih Chen and Dr. Nima Ghalichechian for being my co-advisors during the first and second half of my graduate studies, respectively. I learnt a lot from both of them on how to approach difficult problems and keep focused to become successful.

I would like to thank separately Prof. Waleed Khalil for being in my candidacy examination committee and Prof. Fernando L. Teixeira for being in my candidacy examination and dissertation committee.

Special thanks to Jim Moncrief and other staff members for their help on testing and measurement of various prototypes. Many times, they turned difficult tasks into trivial problems for me.

Most of all, I would like to thank my sister and my parents for providing constant support and love, making this possible.

Vita

December 2 1987Born - Igdır, TURKEY

2010.....B.S. Electrical and Electronics Engineering,
Bilkent University, Ankara, TURKEY

2010-2015Graduate Research Associate, The Ohio
State University

Publications

Journal Publications

E. Yetisir, N. Ghalichechian and John L. Volakis, "UWB Dual-polarized Tightly Coupled Dipole Array with 60° Scanning," *IEEE Antennas and Wireless Propagation Letters*, in preparation.

E. Yetisir, N. Ghalichechian and John L. Volakis, "Ultra-wideband Array with 70° Scanning Using FSS Superstrate," *IEEE Transactions on Antennas and Propagation* (Under Review).

E. Yetisir, C.C. Chen and J.L. Volakis, "UWB Low Profile Multi-port Antenna with Omnidirectional Pattern and High Isolation," *IEEE Transactions on Antennas and Propagation* (Under Review).

E. Yetisir, C.C. Chen and J.L. Volakis, "Low-Profile UWB 2-Port Antenna with High Isolation," *IEEE Antennas and Wireless Propagation Letters*, vol.13, pp.55-58, 2014.

Conference Publications

E. Yetisir, N. Ghalichechian and J. L. Volakis, "A Novel Array with 6:1 Bandwidth and 70° Scanning Using FSS Superstrate," *URSI National Radio Science Meeting*, Boulder, Jan. 2016 (Submitted).

D. Papantonis, E. Yetisir, N. Ghalichechian and J. L. Volakis, "Tunable Band Rejection In A Tightly-Coupled Array Using Varactor Diodes," *International Workshop on Antenna Technology (iWAT)*, Cocoa Beach, FL, 2016 (Submitted).

E. Yetisir, N. Ghalichechian and J. L. Volakis, "Wideband & Wide Angle Scanning Array with Parasitic Superstrate," *IEEE AP-S/USNC-URSI Symposium*, Vancouver, 2015.

E. Yetisir, C.C. Chen and J.L. Volakis, "Wideband Dual-polarized Omnidirectional Antenna with Very High Isolation Across 1.65–2.7 GHz," *IEEE AP-S/USNC-URSI Symposium*, Orlando, FL, 2014.

E. Yetisir, C.C. Chen and J.L. Volakis, "Wideband MIMO antennas with high isolation for personal communications," *IEEE AP-S/USNC-URSI Symposium*, Memphis, TN, 2013.

E. Yetisir, D. Psychoudakis and J.L. Volakis, "Small size conformal UWB arrays for MIMO and diversity applications," *IEEE AP-S/USNC-URSI Symposium*, Chicago, IL, 2012.

Fields of Study

Major Field: Electrical and Computer Engineering

Studies in:

Electromagnetics

Antenna Design and Measurement

Phased Array Antennas

Table of Contents

Abstract.....	ii
Dedication.....	iv
Acknowledgments.....	v
Vita.....	vi
List of Tables	x
List of Figures.....	xi
Chapter 1	Introduction..... 1
1.1	Wide-Angle Scanning Antenna Arrays 4
1.2	Wideband Arrays 7
1.2.1	Tapered Slot Antenna Arrays..... 8
1.2.2	Connected Antenna Arrays 9
1.3	Contribution of Dissertation 17
Chapter 2	Operational Principles and Analytical Models for Connected and Coupled Arrays 20
2.1	Operational Principles..... 20
2.2	Analytical Model for Connected Dipole Arrays..... 22
2.2.1	Application to Coupled Dipole Arrays..... 27
2.3	Approximate Model of Capacitively Coupled Dipole Arrays 32
2.4	Effect of Feeding Lines..... 37
2.5	Summary..... 41
Chapter 3	Frequency Selective Surfaces (FSS) as Superstrate for Tightly Coupled Dipole Arrays (TCDA)..... 43

3.1	Dipole Arrays with FSS	44
3.2	Vertical Patches as FSS superstrate	46
3.3	TCDA with Integrated Marchand Balun and FSS	51
3.4	Modified Marchand Balun for Improved Impedance Matching.....	57
3.5	Optimized Antenna: Geometry and Simulated Performance.....	59
3.6	Summary	63
Chapter 4	Fabricated Prototype and Measured Results.....	65
4.1	Fabrication of the Prototype.....	65
4.2	Measurement of the Prototype	68
4.3	Summary	77
Chapter 5	Dual-Polarized TCDA with Marchand Balun.....	80
5.1	Antenna Geometry with Dielectric Superstrate	81
5.2	Low Frequency Loop Resonance: Bandwidth Limitation	83
5.3	Optimized Array with Limited Bandwidth	89
5.4	Design of Matching Network: Stepped Impedance Transformer	91
5.5	Dual-Polarized TCDA with FSS Superstrate.....	97
5.6	Summary	100
Chapter 6	Scanning Performance of Finite TCDAs with FSS and Dielectric Superstrate.....	101
6.1	FSS Integrated TCDA with Modified Feed	103
6.2	Finite Array: Simulation Setup	105
6.3	Simulation Results for Pointing Accuracy: FSS vs Dielectric.....	107
6.4	Modified FSS with Resistive Terminations for Surface Wave Suppression.....	109
6.5	Summary	114
Chapter 7	Conclusions and Future Work	116
7.1	Summary of This Work	116
7.2	Future Work	118
7.2.1	Fast Optimization of TCDAs	119
7.2.2	Increasing Impedance Bandwidth of Dual-Polarized Dipole Arrays.....	119
7.2.3	FSS Designs for mm-Wave.....	121
7.2.4	Reducing Aperture Density.....	121
Bibliography	122

List of Tables

Table 1.1: Previously designed wideband, wide-scan antenna arrays	16
Table 5.1: Comparison of estimated and actual resonance frequency for different geometrical parameters. d_x and d_y is assumed to be 3.45cm for all cases.	87
Table 5.2: Optimized values of the design parameters for the infinite, dual-polarized array in Figure 5.10.....	94

List of Figures

Figure 1.1: Multifunctional radars. (a) MF-STAR Naval Multi-mission Radar, [2] (b) Agile-beam phased array radar for weather observations, [6].	2
Figure 1.2: Magnetic dipole array with capacitively loaded ground plane from [12]; (a) top view of the magnetic dipole array and (b) side view of the magnetic dipole array, showing the metallic pins and backing reflector.....	5
Figure 1.3: Circuit model of an array with connecting circuits from [16]. Actual connecting capacitors with susceptance jB are shown in (a). After calculating the currents I_u and I_d based on the potentials V_0 , V_a and V_{2a} ; the equivalent model with non-connected capacitors (jB_{eq}) is shown in (b).	6
Figure 1.4: UWB all-metal flared-notch array from [24], ©2010 IEEE. (a) The unit-cell model from side. (b) Fabricated dual-polarized prototype.....	8
Figure 1.5: Top view of a connected array without backing conductor, excited with ideal gap sources. Dipoles are electrically connected along E -plane.....	10
Figure 1.6: Ferrite loaded slot array from [33], ©2008 IEEE.	12
Figure 1.7: Tightly coupled dipole array with integrated balun from [46] , ©2013 IEEE.....	14
Figure 2.1: A tightly coupled dipole array with a backing conductor. The capacitors are implemented in edge-couple geometry, but overlapping or interdigital capacitors can also be used. (a) Physical geometry of a finite array with two-layer dielectric slab as superstrate loading, (b) Approximate circuit model of unit-cell of an infinite array.	21

Figure 2.2: Connected array from [39]. (a) Uniformly excited connected dipole array in free space. (b) Equivalent current distribution, \mathbf{j}_s . (c) Dipole array with ground plane and double feed in each unit-cell.....	23
Figure 2.3: Equivalent transmission line model for the TE and TM modes for a unit strength current element oriented along x-axis and placed at $z=0$	26
Figure 2.4: Double-feed connected array on a ground plane in [39]. For even mode excitation, $V_1=V_2=1V$; for odd mode, $V_1=-V_2=1V$	28
Figure 2.5: Double feed connected dipole array with a ground plane, represented as a lossy two-port component. (a) unit-cell of actual array. (b) two-port model with both ports active (c) port-1 is active and port-2 is terminated with capacitor (C).	29
Figure 2.6: HFSS model of the unit-cell of a capacitively coupled dipole array with a dielectric superstrate. The simulation range is $0.2f_0 - f_0$ (0.75-3.75GHz). Coupling capacitor (C) is 2.5pF and λ_0 is wavelength at f_0 . One of the two feeds is terminated by $C=2.5pF$	31
Figure 2.7: Input impedance of analytical model of (2.15) and full-wave model of unit-cell for the tightly coupled dipole array in Figure 2.6. The simulation range is $0.2f_0 - f_0$	32
Figure 2.8: Approximate ($L-C$) model of a tightly coupled dipole array with dielectric superstrate and air substrate. (a) The full-wave model with lump capacitor loading and ideal gap source, (b) Circuit model (c) Low frequency ($d_x, d_y < 0.4\lambda$) approximations to dipole's self reactance.	34
Figure 2.9: Input impedance of a capacitively coupled dipole array during (right) E and (left) H -plane scanning for $\epsilon_r = 2.5$, across normalized frequency range, 0.2 – 1. The scan angle is 45° . Unit-cell parameters refers to Figure 2.8 and are: $d_x = d_y = 0.5\lambda$, $h_{sub} = 0.35\lambda$, $w_d = 0.05\lambda$, $\delta_d = 0.05\lambda$ at highest frequency ($f = 1$)	36
Figure 2.10: Input impedance of a capacitively coupled dipole array during (right) E and (left) H -plane scanning for $\epsilon_r = 1.5$, across normalized frequency range, 0.2 – 1. The scan angle is 45° . Unit-cell parameters refers to Figure 2.8 and are: $d_x = d_y = 0.5\lambda$, $h_{sub} = 0.35\lambda$, $w_d = 0.05\lambda$, $\delta_d = 0.05\lambda$ at highest frequency ($f = 1$)	37
Figure 2.11: Side view of a dipole array with Marchand baluns as feeds. The shorted stub disrupts the uniformity of the substrate, making the analytical models for this region inaccurate during E -plane scanning	38

Figure 2.12: Comparison of analytical model and full-wave simulations (<i>HFSS</i>) for the infinite connected dipole array, shown in Figure 2.11. For simplicity, open stub is excluded. Array parameters; $d_x = d_y = 0.5\lambda_{\text{high}}$, $h_{\text{sub}} = 0.35\lambda_{\text{high}}$, $h_{\text{sup}} = 0.25\lambda_{\text{high}}$, $w_d = 0.05\lambda_{\text{high}}$, $L_{\text{short}} = 0.23\lambda_{\text{high}}$, $Z_{\text{short}} = 330\Omega$	40
Figure 2.13: Electric field vectors for 45° scan angle in <i>E</i> -plane. Uniform plane wave propagation is clearly visible in superstrate region and above. For substrate region, feed lines disturb the propagating fields. This is not accounted for in the analytical models.	41
Figure 3.1: Unit-cell of a dipole array with different superstrate layers (a) isotropic dielectric slab (b) Vertical metallic patches located on the same PCB with the dipoles. (c) Conformal metallic patch layers with air gap between them (d) Metallic patches embedded in a dielectric medium.	45
Figure 3.2: Impedance response of the dielectric loaded TCDA is shown for different dielectric constant and slab thickness when scan angle is less than 45° . Frequency range is 0.9-3.75GHz for all four cases.	47
Figure 3.3: Impedance response of the dielectric loaded TCDA is shown for different dielectric constant and slab thickness when scan angle is 60° . Frequency range is 0.9-3.75GHz for all four cases.	48
Figure 3.4: Impedance response of the FSS loaded TCDA is shown for different g_{FSS} values when scan angle is less than 45° . The height of the FSS layer, h_{FSS} , is 2cm and frequency range is 0.9-3.75GHz for all three cases.	49
Figure 3.5: Impedance response of the FSS loaded TCDA is shown for different g_{FSS} values when scan angle is 60° . The height of the FSS layer, h_{FSS} , is 2cm and frequency range is 0.9-3.75GHz for all three cases.	50
Figure 3.6: Unit-cell geometry of a TCDA with FSS superstrate and Marchand balun. All of the elements are implemented on a 3-layer PCB, vertically placed over a ground plane.	52
Figure 3.7: VSWR of the infinite array with and without the shorting pin.	54
Figure 3.8: The field distribution in the unit-cell without shorting pin, at resonance frequency. (a) Current distribution along the conductors. (b) Electric field inside the unit-cell volume	54

Figure 3.9: VSWR of the infinite array during scanning in E -plane and H -plane when the shorting pins are capacitively “coupled” or electrically “connected” to the dipoles.	55
Figure 3.10: VSWR of the optimized infinite array excited by ideal gap source. The source impedance is around 150Ω	56
Figure 3.11: The outer conductor of the stripline (going through the balun) is perforated to increase the characteristic impedance.	58
Figure 3.12: Characteristic impedance of the stripline with perforated outer conductor. The PCB board has 44mil total thickness, 3mm total width and a substrate with dielectric constant of 2.2.	58
Figure 3.13: Electric field distribution of unit-cell when scanning 60° in E -plane. The unit-cell size is 0.4λ	59
Figure 3.14: Impedance profile of 18 sections of stepped transformer that matches TCDA input to 50Ω	60
Figure 3.15: Physical dimensions of the fully optimized unit-cell.	60
Figure 3.16: Mismatch efficiency of optimized TCDA for various scan angles along principal and intercardinal plane.	62
Figure 3.17: Normalized X-pol radiation based on Ludwig’s 3 rd definition [61].	63
Figure 4.1: The fabrication steps of the 12x12 prototype.	66
Figure 4.2: Final version of the 12x12 prototype array (top) and the unit-cell elements (bottom) are shown.	67
Figure 4.3: Far-field measurement setup in The Ohio State University anechoic chamber.	69
Figure 4.4: Active elements of the 12x12 prototype during E , H and D -plane measurements are shown with dark color. For D -pane, only one row is used to acquire active element pattern, instead of radiation pattern of the full array.	70
Figure 4.5: Broadside gain of the prototype. Measured values agree well with the simulations (generated from infinite array simulations) at high frequencies. At low frequencies, realized gain exceeds the active aperture limit.	71

Figure 4.6: Schematic of 12x12 dipole array. Equal amplitude/phase element rows (1-to- 12) for H -plane are shown with rectangles. Outer 2-elements on each row are terminated.	73
Figure 4.7: Schematic of 12x12 dipole array. Equal amplitude/phase element rows (1-to-12) for E -plane are shown with rectangles. Outer 2-elements on each row are terminated.	74
Figure 4.8: H -plane patterns at different frequencies, normalized to broadside level. Up to 70° scan angle is verified by good agreement with simulated patterns.	75
Figure 4.9: E -plane patterns at different frequencies, normalized to broadside level. Up to 70° scan angle is verified by good agreement with simulated patterns.	76
Figure 4.10: Simulated and measured 2D active element patterns along D -plane. These were obtained by measuring single 6-element row along diagonal of the aperture, as shown in Figure 4.4c	78
Figure 4.11: Measured element gain (normalized) and cross-pol radiation along the D -plane, for all scan angles across full frequency bandwidth (0.5-3.2 GHz). These were obtained by measuring single 6-element row along diagonal of the aperture, as shown in Figure 4.4c	79
Figure 5.1: Unit-cell of dual-polarized TCDA with integrated Marchand balun.	81
Figure 5.2: VSWR of the array in Figure 5.1, after a quick optimization. The impedance anomalies can be observed around 0.85GHz, limiting the impedance bandwidth.	83
Figure 5.3: Current magnitude along the dipoles and baluns in the presence of the resonance (left) as compared to normal radiation in the absence of resonance (right).	84
Figure 5.4: Current vectors inside the unit-cell in the presence of the resonance: (a) along dipoles and baluns, (b) on the ground plane.....	84
Figure 5.5: Variation of low frequency resonance, as indicated by S_{12} , versus a) balun width, b) ground plane height and c) shorted stub length is shown by S_{12} plots. Cross-polarized radiation for a typical case is shown in d). The array is excited to scan to 45° in diagonal plane.....	86
Figure 5.6: Variation of resonance frequency with coupling between dipoles.....	88

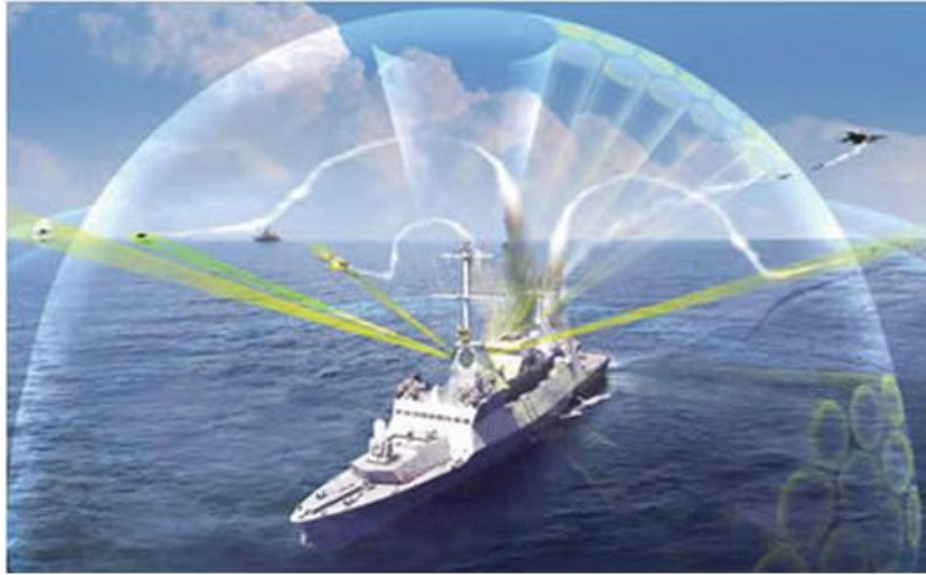
Figure 5.7: Approximate circuit model of the array in Figure 5.1. Marchand balun is modeled as a 2-stage transmission line with short and open stubs	90
Figure 5.8: VSWR values for the optimized infinite array in Figure 5.1, for $Z_{in}=200\Omega$. Unit-cell dimensions; $d_x = d_y = 0.5\lambda$ at $f = 4.35\text{GHz}$	90
Figure 5.9: The circuit, optimized in ADS for minimum S_{11} . The optimization parameters are Z_i and E_i , which are characteristic impedance and electrical length of each transmission line section.	91
Figure 5.10: The final geometry of the dual-pol array with the balun and impedance transformer. Transformer parameters (Z_i , E_i) are obtained via optimizations in ADS	92
Figure 5.11: Mismatch efficiency of the dual-pol array with integrated balun and impedance transformer, for different scan angles.....	95
Figure 5.12: Coupling (top) between input ports of the orthogonally polarized dipoles and the cross-pol radiation (bottom) from each polarization, during D -plane scanning.....	96
Figure 5.13: Dual-polarized TCDA (top) with FSS superstrate and the mismatch efficiency (bottom) for different scan planes. The unit-cell is excited by a 200Ω gap source. 3-layer PCB (RT/duroid 5880, 29mil thick) was used for implementation. Outer copper layers are shown with red color and middle layer is shown with black. The geometry is the same as Figure 5.1, except that the dipole elements on the top PCB are moved onto the vertical PCBs and the dielectric superstrate is replaced by FSS.	98
Figure 5.14: Port coupling and X-pol radiation for the infinite array in Figure 5.13.	99
Figure 6.1: Geometry and the modified TCDA with FSS. Marchand balun was removed from the design in Chapter 3. Instead, an unbalanced pair of coplanar striplines was used to feed the dipole, similar to [40]. 3-layer of copper was used on a 68mil PCB ($\epsilon_r = 2.64$)	103
Figure 6.2: Mismatch efficiency of the array in Figure 6.1 during E and H -plane scanning.	104
Figure 6.3: Semi-infinite array geometry for the E -plane scanning with (a) FSS superstrate and (b) dielectric superstrate. The array is finite along E -plane (scanning) and infinite along the H -plane (non-scanning).....	106

Figure 6.4: Magnitude of the beam pointing error is plotted for semi-infinite TCDA with (a) dielectric superstrate and (b) FSS superstrate. These plots are obtained for $N=19$ and $M=3$ (see Figure 6.3).....	108
Figure 6.5: Unit cell of the TCDA with FSS-v2 This design is only different than the previous one shown in Figure 6.1 in terms of superstrate.	109
Figure 6.6: Efficiency of the array from Figure 6.5 during E and H -plane scanning.	110
Figure 6.7: Semi-infinite array geometry of TCDA with FSS-v2. The active and parasitic dipoles at the array edges are loaded with resistors.	112
Figure 6.8: Beam pointing error for the semi-infinite array of TCDA with (a) FSS-v2 and (b) dielectric superstrate. The error values are plotted for $N=19$ and $M=3$ (see Figure 6.7).....	113
Figure 6.9: E -plane scanning patterns of the array of Figure 6.7 for $\theta \leq 60^\circ$	115
Figure 7.1: Suggested design process for faster optimization of TCDA. (a) Initial full-wave model, loaded with lump ports (b) Extracted S-parameters of the full-wave model (c) Tuning of the array by capacitive or inductive terminations, except the input, using a circuit simulator. (d) Implementation & validation of the optimized design via full-wave simulations. For simplicity, we excluded feed-lines from (a), (b) and (c).....	120

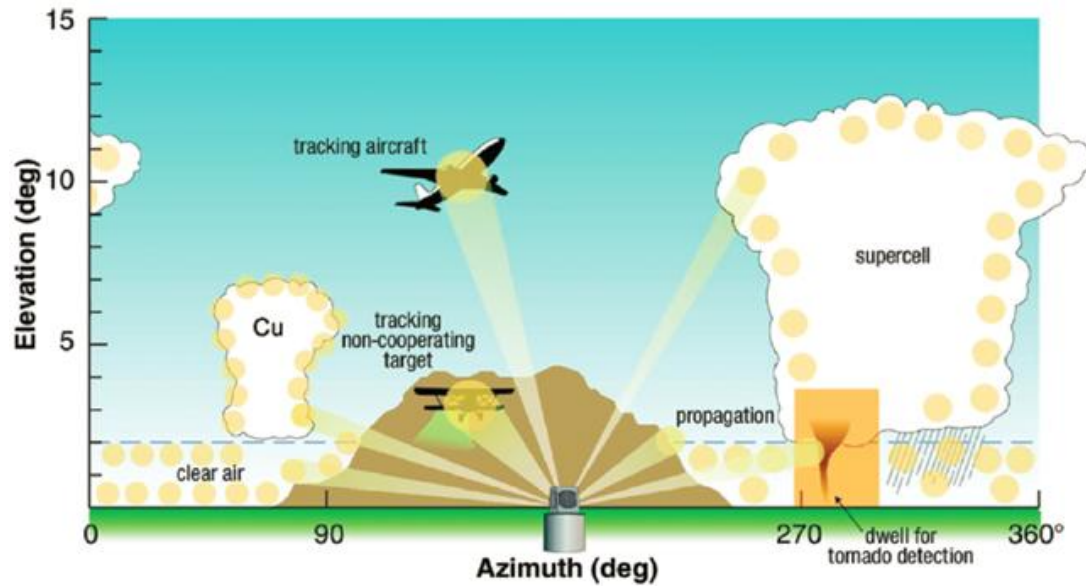
Chapter 1 Introduction

Future mobile and stationary communication platforms are expected to have multiple sensors to cover the desired frequency bands and/or scanning range. To address this issue, novel approaches like the Advanced Multifunction RF Concept (AMRFC) were proposed to reduce the number of antenna apertures and RF/digital hardware for communication, radar and electronic warfare [1]-[2]. Ideally, this concept requires a wideband phased array to provide single aperture for multiple operating frequencies and communication links in different directions (see Figure 1.1-a). In other words, a very wideband antenna array with large scan area is an essential component of such systems.

Software Defined Radio (SDR), which has become more and more popular recently, is another system employing ultra-wideband (UWB), active apertures [3]. For SDR, the antenna aperture might need to operate over large scan angles with agile/adaptive beam-forming in addition to UWB performance, implying the use of phased array antennas. Beam shaping and scanning capability can be particularly useful for hybrid ground terminals (with cognitive radio) communicating with both satellite and other terrestrial ground stations [5]. For these stations, frequency re-use can be possible to increase spectral efficiency but highly reconfigurable beam/patterns are needed to prevent



(a)



(b)

Figure 1.1: Multifunctional radars. (a) MF-STAR Naval Multi-mission Radar, [2] (b) Agile-beam phased array radar for weather observations, [6].

interference between satellite uplinks and ground-to-ground communication, implying a possible use of active, wide-scan antenna apertures. Other applications for wideband and/or wide-scan arrays include air traffic/weather surveillance [6]-[7], electronic warfare [8] and fire control [9].

A major challenge when designing wideband arrays with large scan range is the trade-off between the two goals. That is, for a given efficiency and overall array thickness; bandwidth and scan range of a well-designed array cannot be increased simultaneously [38]. As the scan area is increased, bandwidth is reduced, and vice versa. This is due to the mutual coupling between radiating elements, a phenomenon inherent to all ultra wideband (UWB) arrays with tightly coupled elements. Due to excessive inter-element coupling, *scan impedance* (also referred as *active impedance*: effective impedance seen by a single element when all array elements are excited) of each radiator depends on the phase & amplitude values of the neighboring elements. Therefore, as the element phases are changed during scanning, the scan impedance of each array element also changes. This implies the impedance of the feed-lines cannot be chosen to match to the input impedance of the radiators since their value is not constant during scanning (unless the feeding network is reconfigurable). The variation in scan impedance becomes greater as the range of scan angle increases, indicating that the original bandwidth for the non-scanning array is not going to be maintained. As an example, Wheeler discussed this change using waveguide models to predict the radiation resistance of dipoles in infinite planar arrays [10]. The radiation resistance (R_{rad}) changes with $\cos(\theta)$ and $1/\cos(\theta)$ during scanning in the E and H -plane respectively, where θ refers to the elevation angle from

aperture normal. If $\theta_{max} = 70^\circ$ and $R_{rad} = 377\Omega$ at broadside, then $129\Omega \leq R_{rad} \leq 1100\Omega$ across the entire scan range. Obviously, without any treatment of the array to compensate this variation, it is not possible to achieve simultaneous impedance matching at all scan angles of interest.

Another major challenge in wide-angle scanning arrays is avoiding surface waves. When the array is scanning to specific elevation angles, the radiated energy can couple to longitudinal modes (surface waves) that can be guided along the aperture without radiation, except the diffraction from the aperture edges. This will cause scan blindness in that angle. In [11], Pozar and Schaubert demonstrated a typical example for printed dipoles on a dielectric substrate backed by a conductor. They also provided a simple approach based on coupling from Floquet modes to surface wave modes to predict the direction of scan blindness. As an example, a printed array with $0.5\lambda \times 0.5\lambda$ unit-cell size was considered. The radiating elements were dipoles of 0.39λ length placed on conductor-backed substrate with 0.19λ thickness and $\epsilon_r = 2.55$. When scanned to $\theta = 46^\circ$ in the E -plane, this array excites a surface wave and the input reflection coefficient becomes unity. To increase the surface wave-free scan range, a lower contrast dielectric material with thinner profile over the ground plane is needed.

1.1 Wide-Angle Scanning Antenna Arrays

Although there is a common concern for surface wave problem in case of dielectric loading in substrate or superstrate layers of the array, scan blindness can occur for arrays without any dielectric material. Hannan and Litt [12] considered isolated element pattern of a magnetic dipole and noted that non-zero element gain near the end-fire direction in

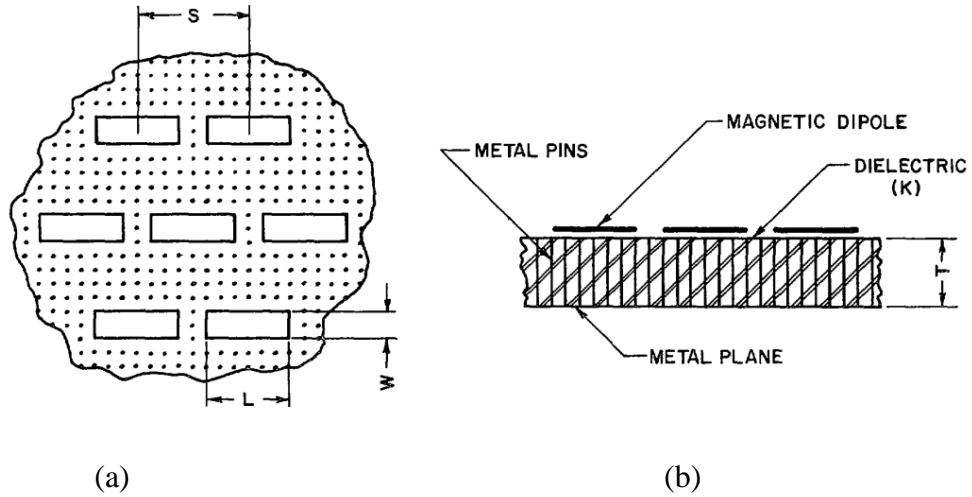


Figure 1.2: Magnetic dipole array with capacitively loaded ground plane from [12]; (a) top view of the magnetic dipole array and (b) side view of the magnetic dipole array, showing the metallic pins and backing reflector.

the E -plane caused coupling to a transverse magnetic (TM) mode along the array structure. As a solution, a capacitively loaded ground plane was proposed using vertical pins of length T ($\lambda/2 > T > \lambda/4$) along the backing conductor (see Figure 1.2). Due to this capacitive ground plane, the TM surface-wave was suppressed [13] and maximum scan angle was increased from 40° to 50° (grating lobe angle) in the E -plane. The same approach was shown to achieve 70° maximum scan angle for an actual slot array in [14].

As mentioned before, a major difficulty for wide angle scanning is the variation in the scan impedance due to mutual coupling. Even if there is no surface wave to cause total scan blindness, the elements should still be impedance matched across the entire scan range to radiate efficiently. However, this is not a trivial problem since the variation in scan impedance can be so great that it may not be possible for elements to be matched

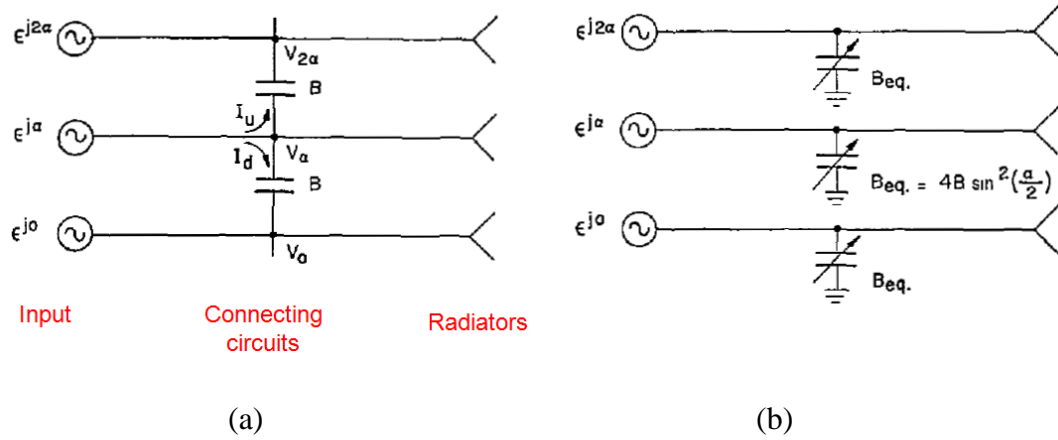


Figure 1.3: Circuit model of an array with connecting circuits from [16]. Actual connecting capacitors with susceptance jB are shown in (a). After calculating the currents I_u and I_d based on the potentials V_0 , V_α and $V_{2\alpha}$; the equivalent model with non-connected capacitors (jB_{eq}) is shown in (b).

simultaneously for all the scan angles of interest. Edelberg and Oliner [15] suggested vertical conducting baffles to isolate the array lattices along E -plane. This caused the electromagnetic field of substrate region to be confined under dipoles instead of coupling to neighboring elements during scanning along the E -plane. By using an equivalent circuit to optimize the array, the authors achieved 60° maximum scan angle with $VSWR < 2$.

Hannan et al. [16] proposed connecting circuits between feed lines of the radiating antennas, as depicted in Figure 1.3a. Instead of preventing coupling between neighboring radiators, authors created additional coupling paths between them so that the net port-to-port leakage between each unit-cell element was less problematic. The equivalent circuit model of the proposed approach is shown in Figure 1.3b. These additional paths include reactive elements and have no effect during broadside radiation. This is due to the fact

that all radiators are in phase and there is no potential difference between feed lines and connecting circuits of neighboring elements. When the array scans, each element has different phase, resulting in a potential difference between the terminals of connecting circuits. As a result, these circuits draw current from the feed lines of radiators and modify the scan impedance. Depending on the initial impedance of the unit cell elements across the scan range of interest, authors used capacitive or inductive components between neighboring feed lines to achieve 60° maximum scan angle with $VSWR < 1.7$.

Dielectric layers over the array aperture have been widely known to improve scanning. Magill and Wheeler proposed to use thin dielectric sheets ($< \lambda_g / 4$) as wide-angle impedance matching layers [17]. These sheets were approximated as angle dependent shunt susceptance. By optimizing the location and thickness of an alumina sheet ($\epsilon_r = 9.5$) above a waveguide array, the authors showed $\pm 56^\circ$ scanning with $VSWR < 1.8$.

Munk et al. [18] used stratified dielectric slabs, with relatively lower dielectric constant but thicker profile, to transform the radiation pattern of dipole and slot elements to vary as the cosine of the scan angle. A dipole array, sandwiched between two dielectric slabs and placed above a ground plane, was shown to have 80° maximum scan angle for $VSWR < 1.5$.

1.2 Wideband Arrays

One of the simplest printed wideband arrays is formed by aperture coupled stacked patch antennas [19]. With multi-layer designs and impedance matching via the aperture coupling, these arrays can provide $\pm 60^\circ$ scan angle and $\sim 2.5:1$ impedance bandwidth [20]. Since they are typically of very low profile, it is also possible to implement them on

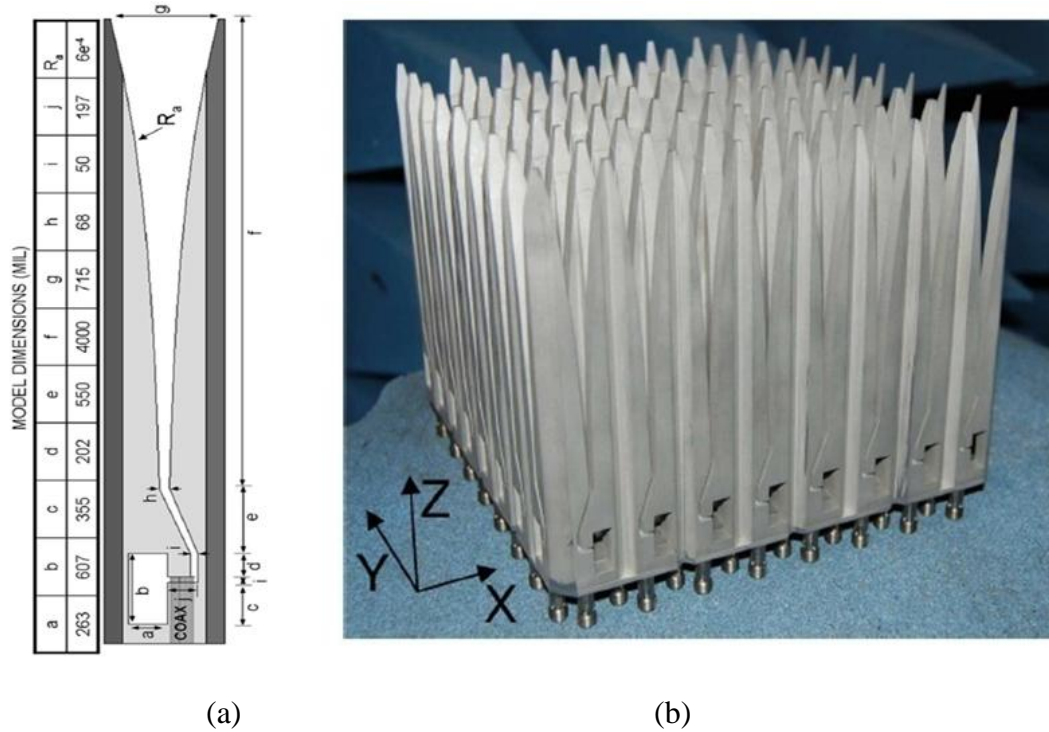


Figure 1.4: UWB all-metal flared-notch array from [24], ©2010 IEEE. (a) The unit-cell model from side. (b) Fabricated dual-polarized prototype

curved platforms in a conformal way by approximating the curved surface with small planar apertures [21]. However, in terms of very large bandwidth ($>3:1$), two classes of arrays have attracted strong interest in recent years: (1) Tapered slot antenna arrays and (2) Connected antenna arrays. In next sections we will discuss these UWB arrays.

1.2.1 Tapered Slot Antenna Arrays

A tapered slot array, also known as Vivaldi, is a popular wideband scanning antenna, which has been used for decades [22]. Different versions of this array focus on bandwidth, modularity, scanning or power handling [23], [24], [25]. Vivaldi arrays can achieve $>10:1$ impedance bandwidth at the expense of thickness [23]. Also scanning

down to $\pm 60^\circ$ has been reported [24]. However, they suffer from low polarization purity when scanning in the intercardinal plane, even for moderate elevation angles. Although correction algorithms have been proposed for dual-polarized arrays, they do not provide simultaneous coverage across the entire bandwidth and scan area [26].

More recently, low profile versions of Vivaldi arrays have been proposed to address the cross-polarization issue [27], [28]. One particular example is the decade bandwidth Balanced Antipodal Vivaldi Antenna (BAVA) array [28], using an impedance matching approach similar to Vivaldi. The total height is less than half a wavelength at the highest frequency of operation, resulting in improved polarization purity. However, the BAVA array has poor impedance matching when scanning across the H -plane, limiting their typical scanning range to 45° .

1.2.2 Connected Antenna Arrays

Another class of wideband arrays is referred to as connected arrays. Unlike tapered slots, connected arrays are usually arranged in a planar geometry (see Figure 1.5). They can be formed by dipoles or slots. The connection (via capacitive or inductive coupling) between neighboring elements helps to maintain a constant current along the elements, resulting in frequency independent input impedance. Input impedance of these arrays has very low reactance and almost constant resistance at low frequencies, where the lattice size is much smaller than the wavelength [10], [29]. In fact, the radiation resistance of a planar connected dipole array in free space can be calculated by the shape of the unit-cell (assuming no grating lobes);

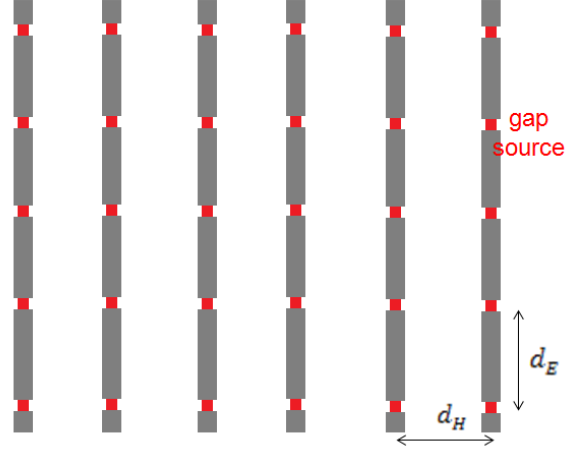


Figure 1.5: Top view of a connected array without backing conductor, excited with ideal gap sources. Dipoles are electrically connected along E -plane.

$$R_{rad} = \frac{d_E}{d_H} \frac{Z_0}{2 \cos\theta}, \quad \text{along } H - \text{plane} \quad (1.1)$$

$$R_{rad} = \frac{d_E}{d_H} \frac{Z_0}{2} \cos\theta, \quad \text{along } E - \text{plane}$$

Here, d_E and d_H refers to the lattice size of the array along E and H -plane. Z_0 is characteristic impedance of free space and θ is the elevation angle from the aperture normal. We observe that, there is no frequency dependence on the radiation resistance of an over-sampled array, indicating wideband behavior. When the array periodicity is very small, evanescent higher order Floquet modes will not be strongly excited, resulting in very low reactance. Therefore, (1.1) implies no cut-off at the low end of the frequency band for infinitely long connected arrays. However, for practical arrays, d_E and d_H are chosen to be $\sim \lambda_{high}/2$. Consequently, the exact value of the input impedance depends on both the fundamental and higher order Floquet modes.

Impedance behavior of infinitely long bi-directional slot arrays has been analyzed using Green's function approach in [30] and [31]. When the array periodicity is less than 0.4λ , input impedance is almost frequency independent with very small reactance. However, the bandwidth is reduced to less than 50% when the array is backed by a conducting plane. This is due to ground plane acting like a small shunt inductor, which shorts out the array at low frequencies.

Impedance matching along the feed lines of the array might help increasing the bandwidth of slot arrays up to 4:1 [32]. Ferrite loaded substrates, as depicted in Figure 1.6, can usually improve bandwidth even more. Due to the high characteristic impedance of these materials, the effect of ground plane can be significantly mitigated to achieve 10:1 impedance bandwidth with 60° scan angle [33]. Although the bandwidth is impressive, ferrites are typically heavy/bulky and increasingly lossy for higher frequencies.

Munk [34] proposed capacitively coupled dipoles instead of electrically connected radiators. The idea was to mitigate reactive (inductive) loading from the ground plane using capacitive coupling among neighboring elements. Dipoles are approximated as inductors and used together with the coupling capacitors as series L - C impedance matching stage [35]. Since the antenna elements are closely spaced and tightly coupled, the current on the dipoles is almost constant, realizing Wheeler's current sheet [10]. Munk's concept could achieve up to 4.5:1 impedance bandwidth [38], viz significantly better than electrically connected arrays (<50% bandwidth) with no inter-element capacitance. Adding two dielectric slabs above the array aperture can increase the



Figure 1.6: Ferrite loaded slot array from [33], ©2008 IEEE.

bandwidth to 9:1 with scan angles up to 60° [37]. However, external wideband 180° hybrids were required to avoid common mode resonances along the feed lines of the dipoles. As a result, the feed was bulky and expensive.

To avoid complex baluns, different approaches have been proposed. One approach is to place shorting pins between the dipole aperture and the ground plane to shift the common mode resonance out of the operational band [40], [41], [42], [43]. The planar ultrawideband modular array (PUMA), described in [41], provided 5:1 impedance bandwidth and $\pm 45^\circ$ scanning using a single layer of dielectric superstrate and a single stage matching circuit. The latter is printed after the feed lines and below the ground plane. When more impedance matching is used, the bandwidth can be increased to 6:1. The array is formed by multilayer printed structures, useful for frequency scalability. However, the radiating elements are embedded inside dielectric slabs having a relative dielectric constant of $\epsilon_r \geq 1.96$. The substrate and superstrate layers of the array combine to form a thick dielectric slab over the ground plane. This leads to surface waves, even

for moderate scan angles [11]. To address this issue, perforations across the dielectric layers were proposed (similar to [44]) to reduce the effective dielectric constant and push the onset of surface waves out of the intended scan range and frequency band. However, practical arrays are still limited to less than 60° , and therefore not suitable for wider angles.

Another tightly coupled dipole array (TCDA) design with an integrated feed was reported in [45]. The array has less than 0.4λ periodicity and uses air substrate, resulting in surface-wave free operation beyond 70° scan angle. A printed balun on the ground plane differentially feeds two vertical pins to excite the dipole elements. However, the impedance bandwidth is only 1.6:1 because of the limited performance of the balun. Also due to the air substrate, accurate placement of the feeding pins is not a trivial task, making the fabrication process laborious.

Munk's coupled dipole concept was recently enhanced with an integrated feed (see Figure 1.7) [46]. Specifically, a PCB implementation of folded Marchand balun [47] was used to excite the dipoles. The balun was in effect a 2-stage impedance matching circuit. It was optimized together with other array parameters to achieve an impressive 7.35:1 impedance bandwidth. However, scanning was limited to 45° . A single layer of dielectric superstrate was used to compensate impedance variation while scanning. It is important to note that the radiating elements in each unit cell were split into two small dipoles along the E -plane. This was done to reduce the input impedance for easier matching. The dipole pair was then fed by a Wilkinson power divider. However, this approach caused resistive loss while scanning in the E -plane. Although the reported resistive loss was less than

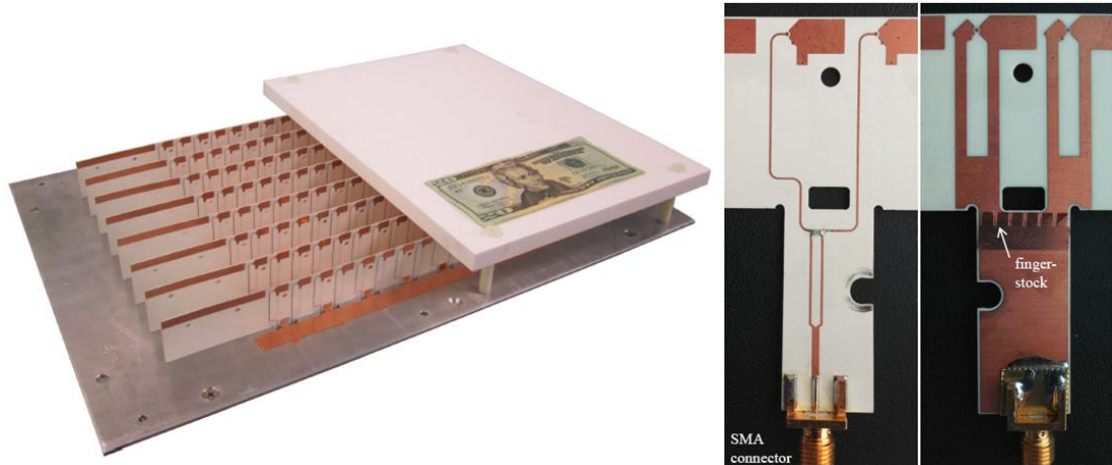


Figure 1.7: Tightly coupled dipole array with integrated balun from [46] , ©2013 IEEE

0.8dB up to 45° , it increases for larger elevation angles. Moulder *et al.* [48] used a similar feeding mechanism with a resistive FSS inside the substrate of the array. The bandwidth was 13.9:1 but increasing loss was again limiting wide angle scanning. To prevent losses due to the power divider, one can be tempted to use a fully reactive (lossless) power divider. However, these lossless splitters can cause resonances, particularly during *E*-plane scanning, resulting in scan blindness for certain elevation angles [49]. This is due to the loss of symmetry of the 2-port “scattering matrix” of the radiator inside the unit-cell. Therefore, having a lossy power divider is actually essential to keep the arrays with “split” unit-cell (e.g. [46], [48]) functional, implying these arrays cannot efficiently radiate during wide-angle scanning across *E*-plane.

Another type of connected arrays is referred as the “fragmented aperture” [50], [51]. These arrays can be considered as a hybrid of electrically connected and capacitively coupled arrays. A “pixelated” element is used instead of a simple dipole or slot radiator.

The exact shape of the pixilated radiator is obtained by optimization algorithms. However, this approach can typically help array performance at the very high end of the bandwidth, rather than at the low end. This is because, for lower frequencies, the unit-cell size is significantly smaller than half-wavelength and the shape of the planar radiating element has minimal effect on input impedance, as mentioned before. Therefore, for wide-scan and/or wideband performance of connected arrays, approaches like resistively loaded ground plane and dielectric superstrate are far more significant.

Spiral antennas, which are inherently wideband single element radiators, can also be used to design wideband arrays with circular polarization. One example is the Interwoven Spiral Array (ISPA) with 10:1 impedance bandwidth for broadside radiation [52]. The unit-cell spirals are tightly coupled to neighboring elements via interwoven arms, effectively making the antenna a connected array. However, the array does not have stable behavior during scanning, limiting its use to non-scanning applications. Another example of spiral elements used in phased array was reported in [53]. This particular example has an octave bandwidth and can scan up to $\pm 45^\circ$. Impedance anomalies during scanning are suppressed by employing non-symmetric spiral arms that prevents the formation of high amplitude standing waves. Overall, the spiral array in [53] can be used as a wideband circularly polarized scanning antenna array. However, it is still outperformed by most of the linearly polarized connected arrays in the literature.

Some of the wideband, wide-scan arrays discussed until now are summarized in Table 1.1. As can be seen, tapered slot arrays (TSAs, *e.g.* *Vivaldi*) can achieve wide-scan performance across $\sim 10:1$ impedance bandwidth but they are not of low profile and have

Table 1.1: Previously designed wideband, wide-scan antenna arrays

Design	VSWR	Bandwidth	Array Thickness	Maximum Scan Angle	Superstrate Type
TCDA [46]	2.65	7.35:1	$0.095 \lambda_{low}$	H-45° , E-45°	Dielectric
TCDA [45]	2	1.6:1	$0.3 \lambda_{low}$	H-60° , E-70°	Dielectric
BAVA [28]	4	10:1	$0.05 \lambda_{low}$	H-45° , E-45°	-
Flared Notch [24]	2 (2.6)	9.5:1 (7.6:1)	$0.37 \lambda_{low}$ ($0.43 \lambda_{low}$)	H-45° , E-45° (H-60° , E-60°)	-
TCDA [41]	2.9	5:1	$0.092 \lambda_{low}$	H-45° , E-45°	Dielectric

cross-polarization issues. Modified versions of these arrays (e.g. BAVA) with lower heights can also have bandwidths up to 10:1 but their efficiency degrades when scanning. Connected arrays, particularly tightly coupled arrays, have better scan performance with superstrate loading (e.g. dielectric).

Due to their superior scanning capability and large impedance bandwidths, this work focuses on tightly coupled dipole arrays (TCDA). Other than mitigating the variation in the input impedance during wide-angle scanning (which are required from all wide-angle arrays), the major challenges for TCDA are as follows;

- **Wideband & efficient feeding:** Widest bandwidth with $\pm 60^\circ$ scan angle for a TCDA was reported in [54]. The authors adopt split unit-cell approach and use a 2-way power divider to feed dipole pairs in each unit-cell with a single port. Although the maximum scan angle was reported to be 60° , total efficiency goes down to almost -2.5dB at high end of the frequency band (unit-cell size is

$\sim 0.4\lambda_h$). This is due to the lossy power divider. Therefore, it is necessary for a wide-angle array to have lossless feeding schemes for efficient radiation.

- **Impedance matching:** It is well-known that any type of feed for these arrays should be suitable to be used as an impedance matching circuitry for best performance. Also, since they need to be lossless for wide-angle scanning, it is more challenging to suppress resonant common modes along these feed-lines.
- **Surface waves:** Typically, TCDAs have good scanning performance if some type of superstrate loading (e.g. dielectric) is used. This might cause excitation of surface waves for large scan angles and when the unit-cell size becomes comparable to half-wavelength. Therefore, a novel superstrate design is needed to delay the onset of these surface waves as much as possible.
- **Bulky superstrate:** The dielectric slab(s) used for superstrate loading also has practical problems. It will cause significant increase in array weight, which might be especially critical for lower microwave frequencies and mobile applications. We also note that, the required dielectric constant is typically very low ($\epsilon_r < 2$). Since there are not many commercially available materials with this property, custom made materials might be needed, increasing the cost significantly.

1.3 Contribution of Dissertation

As mentioned before, this work focuses on TCDAs. The key contributions addressing the aforementioned challenges in previous section are as follows:

1. **FSS Loaded TCDA with $\pm 70^\circ$ Scan Angle (Chapter 3 - Chapter 4):** Printed FSS elements are employed to design a wideband array ($> 6:1$) with very large

scan range ($\pm 70^\circ$). The FSS, radiating dipoles and the feed lines are designed and fabricated on the same vertically-placed PCB, resulting in a low-cost and light-weight structure as opposed to other arrays with bulky dielectric slab(s). The approach is verified by fabricating & measuring a 12×12 prototype.

2. Modified Marchand Balun for Wide-Angle Wideband TCDA (Chapter 3):

As mentioned before, excitation of the TCDA without degrading their wideband performance is not a trivial task. To address this issue, we developed a folded Marchand balun with a modified implementation. The proposed design relaxes the stringent fabrication requirements on feeding lines, resulting in better matching, without employing split unit-cell geometries that were used in [46] and [48]. As a result, the proposed balun makes it possible to maintain the impedance bandwidth over wider scan ranges without excessive resistive loss.

3. Dual-pol TCDA with Marchand Balun (Chapter 5):

By employing the same modified balun, as mentioned above; a dual-pol TCDA with 4.5:1 bandwidth was designed. Maximum scan angle is 70° in the E -plane and 60° in H -plane.

4. Scalable TCDA with Unbalanced Feeding (Chapter 6):

TCDA designs are presented with $\pm 70^\circ$ scanning using different FSS superstrates. Instead of the Marchand balun, an unbalanced feed structure is employed to ease the fabrication and make the array scalable to higher frequencies (e.g. X & Ku-band).

The rest of the dissertation is organized as follows:

Chapter 2 reviews analytical models for connected/coupled dipole arrays. We discuss the accuracy of these models for different cases and how/when to use them during the design process.

Chapter 3 introduces the FSS loaded TCDA with the modified Marchand balun. The operational principals and design approach for the array and feed/transformer are provided. Chapter 4 presents a fabricated 12x12 prototype of the FSS-loaded array and its measured results.

In Chapter 5, we discuss how to design a dual-polarized TCDA using the same balun introduced in Chapter 3. However, we also show that, the main limitation on the bandwidth of the dual-polarized array is actually a resonance along the feed-lines rather than performance of the superstrate. Therefore, we will show that using FSS or dielectric superstrate does not make significant difference in terms of achievable bandwidth for this specific type of feeding scheme.

Chapter 6 studies the effect of finite array size on the main beam accuracy. To do this, we first modified the FSS unit-cells to have much better impedance matching during scanning (albeit with a fairly reduced bandwidth). Then we used this design in finite apertures to see the effect of using FSS or dielectric on the diffractions at the aperture edges and the resulting pattern degradations. In Chapter 7, we provide a summary of this work and discuss the opportunities for future work regarding wide-angle scanning arrays.

Chapter 2 Operational Principles and Analytical Models for Connected and Coupled Arrays

In this chapter, we discuss capacitively coupled dipole arrays in more detail. We will briefly discuss the operational principles and then review an analytical model [39] approximating the behavior of these arrays. In Section 2.3, we will compare a more popular but approximate model from [35] to the one in [39]. Then we will discuss the effect of vertically placed feed-lines of these arrays, which are typically ignored in these models.

2.1 Operational Principles

The simplest version of a tightly coupled dipole array (TCDA) that has no material loading is formed by small capacitively coupled dipoles, placed over a conducting ground plane. The ground plane distance is around 0.1λ at lowest frequency of operation and the total bandwidth is approximately 4:1 without any external matching circuits. UWB performance is achieved by tuning the capacitive gaps between neighboring dipole tips. This makes it possible to support an almost uniform current along the coupled dipoles across a wide frequency range so that the radiation resistance stays constant [10]. The

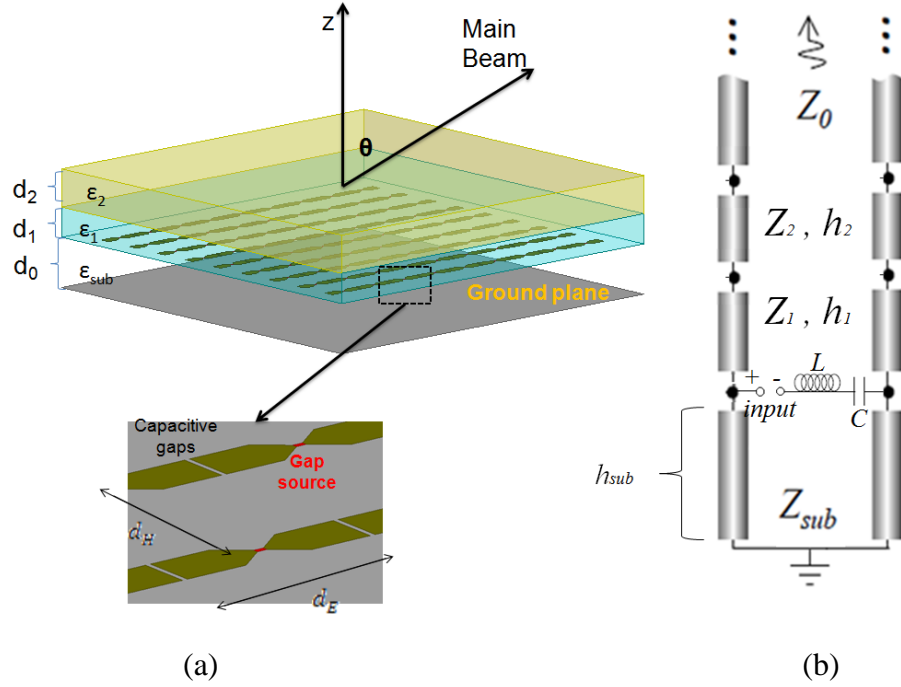


Figure 2.1: A tightly coupled dipole array with a backing conductor. The capacitors are implemented in edge-couple geometry, but overlapping or interdigital capacitors can also be used. (a) Physical geometry of a finite array with two-layer dielectric slab as superstrate loading, (b) Approximate circuit model of unit-cell of an infinite array.

capacitive loading also helps mitigating the reactive loading of ground plane. The distance of ground plane to dipole aperture is a very important parameter to have wideband operation. Reactive loading of a closely placed conducting ground plane is inductive. However, the capacitive coupling between dipoles can be tuned to an optimum value so that inductive effect of ground can be cancelled out. As the frequency goes higher, the distance from ground plane becomes more than quarter wavelength and its reactive loading to the dipoles becomes capacitive. Also, as the frequency increases, the self-inductance of small dipoles becomes dominant to the coupling capacitance. Thus, the self impedance of dipoles becomes inductive. This inductive impedance can again be

tuned to cancel out capacitive effect of ground plane at high frequencies. As a result, impedance matching can be achieved across the frequency range where ground plane distance changes from approximately 0.1λ to 0.4λ , which corresponds to 4:1 bandwidth. Of course, the actual available bandwidth depends on the required minimum mismatch efficiency of the array. For fundamental bandwidth limits, one can refer to [38]. To improve the bandwidth, dielectric slab(s) can be placed over the dipole aperture, reducing the radiation resistance such that the reactive loading due to ground plane can be mitigated (to some extent). A TCDA with two layers of dielectric superstrates are shown in Figure 2.1 with an approximate circuit model. More detail about operational principles and design approaches can be found in [35].

2.2 Analytical Model for Connected Dipole Arrays

In [39], a 2D planar array of connected dipoles (see Figure 2.2) with one or multiple feeding points in a unit-cell was analyzed. Radiating elements and any possible dielectric layers are all assumed to be placed in a stratified manner, parallel to x - y plane so that planar boundary conditions can be used when solving the integral equations. This is a reasonable approximation except the feed lines, which are usually placed vertically along z -axis. Authors simply assumed that the feeding structure does not support common modes at all so that they are invisible to any of the Floquet modes (propagating or evanescent) inside the substrate region. For most of practical wideband arrays (e.g. PUMA arrays with shorting pins [41], TCDA with Marchand balun [48] etc.), this is not true. There will be vertical conductors inside the substrate which will interact with any plane wave, even though they do not support a “resonant” common mode. However, for

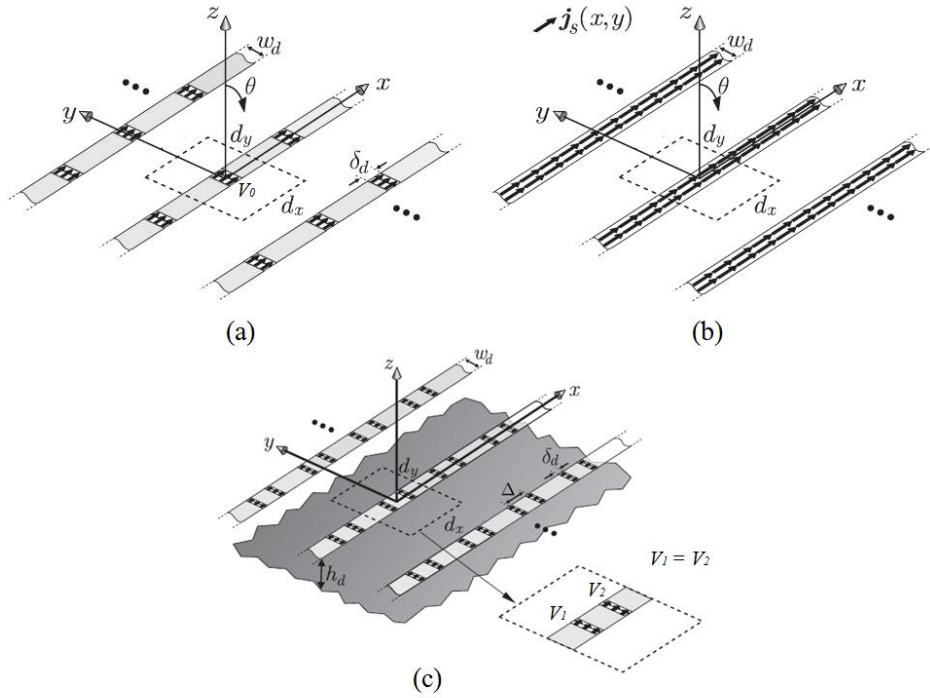


Figure 2.2: Connected array from [39]. (a) Uniformly excited connected dipole array in free space. (b) Equivalent current distribution, \mathbf{j}_s . (c) Dipole array with ground plane and double feed in each unit-cell.

now, we will briefly review the approach and results obtained in [39], [55] and discuss the problem with feed lines later.

In [39], the integral equation related to Figure 2.2a & b, after enforcing the continuity of tangential component of electric field along x -axis ($y = 0$), was expressed as follows;

$$\int_{-\infty}^{\infty} \int_{-\infty}^{\infty} g_{xx}^{EJ}(x - x', -y') j_x(x', y') dx' dy' = -e_x^i(x, 0) \quad (2.1)$$

Here, j_x represents the current along the dipoles ($\mathbf{j}_s(x, y) = j_x(x, y) \hat{\mathbf{x}}$), which is assumed to have no y -component. g_{xx}^{EJ} represents the spatial Green's function (GF) related with the x -oriented electric field at $z=0$ due to x -oriented current at $z=0$. The

impressed field is represented by $e_x^i(x, 0)$ which is uniform at feeding gaps and zero elsewhere. In other words, it is an infinite sum of rectangular functions, centered at feed points;

$$e_x^i(x, 0) = \sum_{n_x=-\infty}^{\infty} \frac{V_0}{\delta_d} \text{rect}_{\delta_d}(x - n_x d_x) e^{-jk_{x0} n_x d_x} \quad (2.2)$$

where $k_{x0} = k_0 \sin(\theta_0) \cos(\phi_0)$ due to the longitudinal excitation condition when the array is scanning to (θ_0, ϕ_0) . For the transverse direction during scanning to (θ_0, ϕ_0) , one would define $k_{y0} = k_0 \sin(\theta_0) \sin(\phi_0)$.

The function $j_x(x, y)$ is assumed to be separable such that $j_x(x, y) = i_x(x)j_t(y)$ where the transverse (y) component is chosen to satisfy the edge-singularity condition;

$$j_t(y) = \frac{2}{w_d \pi} \frac{1}{\sqrt{1 - \left(\frac{2y}{w_d}\right)^2}} \quad (2.3)$$

By using these assumptions above, the authors solve equation (2.1) in spectral domain to find the discrete current spectrum and then inverse Fourier transform of it to get the equivalent spatial current magnitude, $i_x(x)$. Then, they just express the input admittance (Y_{in}) as the average current across the feed gap divided by the impressed voltage (V_0). For a general case of multiple feeds per unit-cell, $i_x(x)$ is expressed as;

$$i_x(x) = \frac{1}{d_x} \sum_{m_x=-\infty}^{\infty} \frac{-E(k_x)}{D_{\infty}(k_{xm})} e^{-j x k_{xm}} \quad (2.4)$$

$$D_{\infty}(k_x) = \frac{1}{d_y} \sum_{m_y=-\infty}^{\infty} J_0\left(\frac{k_{ym} w_d}{2}\right) G_{xx}^{EJ}(k_x, k_{ym}) \quad (2.5)$$

$$E(k_x) = \int_{-d_x/2}^{d_x/2} e_x^i(x') e^{j x' k_x} dx' \quad (2.6)$$

Here, $k_{xm} = k_0 \sin(\theta_0) \cos(\phi_0) - \frac{2\pi m_x}{d_x}$ and $k_{ym} = k_0 \sin(\theta_0) \sin(\phi_0) - \frac{2\pi m_y}{d_y}$

represents the wave numbers for the Floquet mode (m_x, m_y) . $E(k_x)$ is 1-D Fourier transform of the impressed electric field, $e_x^i(x)$, of a unit-cell, which can be assumed uniformly distributed along the feed gap(s). After taking the average of $i_x(x)$ across the feed gap and dividing it by the impressed voltage, the resulting input admittance becomes;

$$Y_{in,p} = \frac{1}{V_p d_x} \sum_{m_x=-\infty}^{\infty} \frac{-E(k_x) \text{sinc}\left(\frac{k_{xm} \delta_d}{2}\right)}{D_{\infty}(k_{xm})} e^{-j x_p k_{xm}} \quad (2.7)$$

where $Y_{in,p}$ represents the input admittance for the input port p in the unit-cell. V_p is the impressed voltage value and x_p is the location of the same port. To actually evaluate the input admittance, one needs to calculate $G_{xx}^{EJ}(k_x, k_y)$, which is Fourier transform of the spatial Green's function g_{xx}^{EJ} in equation (2.1). For a shunt (directed along x -axis) current at $z = z'$, it is given as;

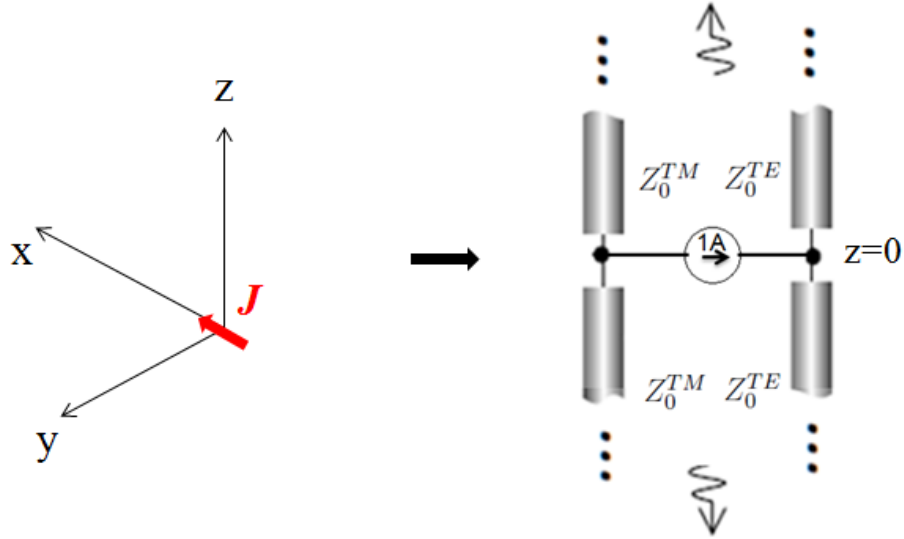


Figure 2.3: Equivalent transmission line model for the TE and TM modes for a unit strength current element oriented along x-axis and placed at $z=0$.

$$G_{xx}^{EJ}(k_x, k_y, z, z') = -\frac{k_x^2 v_{TM}^J(k_x, k_y, z, z') + k_y^2 v_{TE}^J(k_x, k_y, z, z')}{k_x^2 + k_y^2} \quad (2.8)$$

Here v_{TM}^J and v_{TE}^J represents the impressed voltage due to the transverse magnetic (TM) and transverse electric (TE) waves in the direction of (k_x, k_y) . These values depend on the actual geometry of the problem and cannot be written in a generic form. For the simplest case of a current element in free-space as shown in Figure 2.3, we have;

$$v_{TM}^J(k_x, k_y, z, z') = \frac{Z_0^{TM}(k_x, k_y)}{2} e^{-jk_z |z-z'|}, \quad (2.9)$$

$$v_{TE}^J(k_x, k_y, z, z') = \frac{Z_0^{TE}(k_x, k_y)}{2} e^{-jk_z |z-z'|}$$

$$Z_0^{TM} = Z \frac{k}{k_z}, \quad Z_0^{TE} = Z \frac{k_z}{k} \quad (2.10)$$

where $Z = Z_0 / \sqrt{\epsilon_r}$ is characteristic impedance of the medium. Similarly, $k = k_0 \sqrt{\epsilon_r}$ is the propagation constant of the medium. The propagation constant along z -axis is defined as $k_z = \sqrt{k^2 - k_x^2 - k_y^2}$. It can be imaginary, indicating an evanescent wave. However k_z should be chosen such that the wave exponentially decays as it propagates along the z -axis, instead of blowing up. We note that $z = z' = 0$ and the dielectric is air ($\epsilon_r = 1$), for our case (see Figure 2.2).

2.2.1 Application to Coupled Dipole Arrays

Input impedance of a connected array can be evaluated using equation (2.7). For more detail on how it is actually derived and the dispersion analysis for any possible poles in the admittance, one can refer to [39]. Equation (2.7) can also be used to analyze capacitively coupled dipole arrays (which are the main focus of this work), as suggested by [59]. Specifically, (2.7) can be used to extract the 2×2 admittance matrix of a double-feed connected dipole array. Then this matrix can be used to obtain the input admittance of a single feed, capacitively coupled dipole array.

To calculate input impedance of a tightly couple dipole array, we fist consider a double feed connected array (see Figure 2.4). If we look at the unit-cell centered at $x=0$, it can be seen that this cell has two feeding points at $x=\Delta/2$ and $x=-\Delta/2$ with the excitation voltages of V_1 and V_2 . If we assume $\Delta = d_x / 2$, then by (2.6), 1-D Fourier transform of the incident electric field inside this unit-cell can be expressed as follows;

$$E(k_x) = (V_1 e^{j k_x d_x/4} + V_2 e^{-j k_x d_x/4}) \text{sinc} \left(\frac{k_{xm} \delta_d}{2} \right) \quad (2.11)$$

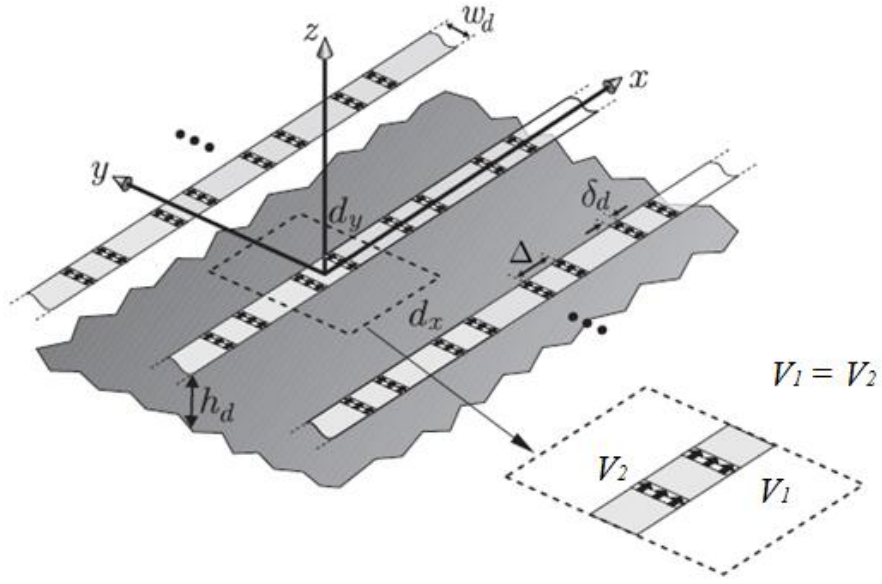


Figure 2.4: Double-feed connected array on a ground plane in [39].

If we plug (2.11) into (2.7), we have the electrical currents $I_1 = Y_1 V_1$ and $I_2 = Y_2 V_2$ flowing through port 1 and port 2 as follows;

$$\begin{aligned}
 I_1 &= - \sum_{m_x=-\infty}^{\infty} \frac{\left(V_1 e^{\frac{j k_x d_x}{4}} + V_2 e^{-\frac{j k_x d_x}{4}} \right) \text{sinc} \left(\frac{k_{xm} \delta_d}{2} \right)^2}{d_x D_{\infty}(k_{xm})} e^{-\frac{j k_x d_x}{4}} \\
 I_2 &= - \sum_{m_x=-\infty}^{\infty} \frac{\left(V_1 e^{\frac{j k_x d_x}{4}} + V_2 e^{-\frac{j k_x d_x}{4}} \right) \text{sinc} \left(\frac{k_{xm} \delta_d}{2} \right)^2}{d_x D_{\infty}(k_{xm})} e^{\frac{j k_x d_x}{4}}
 \end{aligned} \tag{2.12}$$

As mentioned before, we can also assume that this 2-feed unit-cell is represented by a 2×2 admittance matrix: $\mathbf{Y} = \begin{bmatrix} Y_{11} & Y_{12} \\ Y_{21} & Y_{22} \end{bmatrix}$ (see Figure 2.5a & b). Then we have the following relation between I_1, I_2 and \mathbf{Y} ;

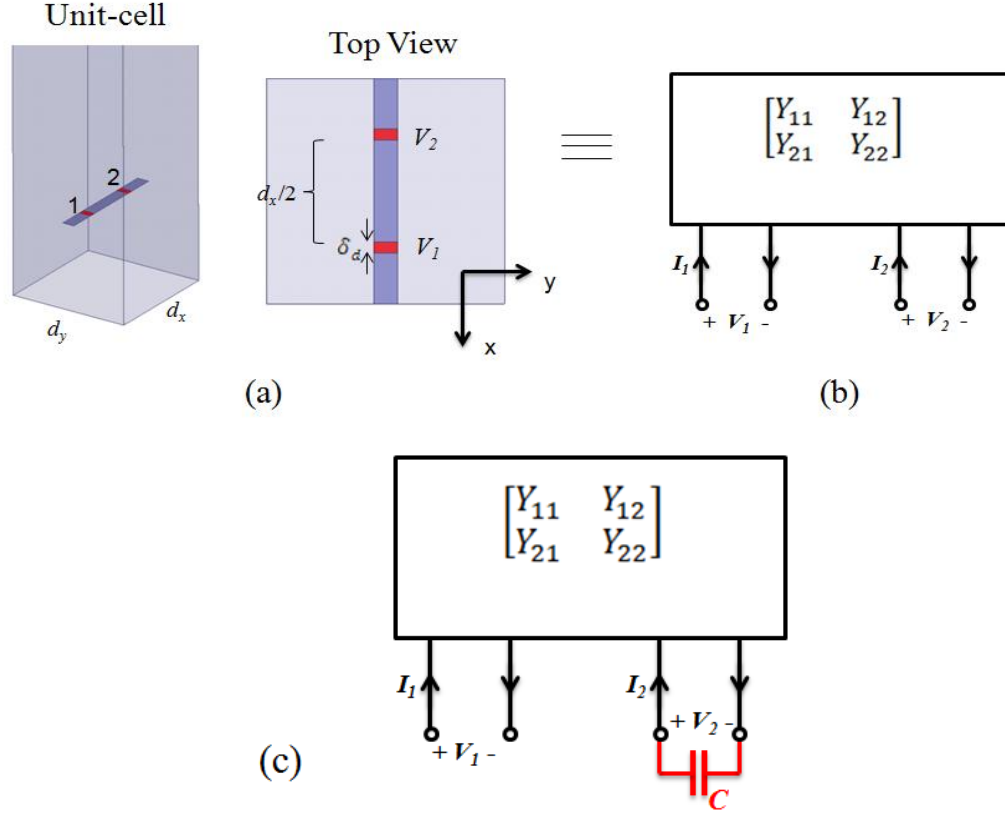


Figure 2.5: Double feed connected dipole array with a ground plane, represented as a lossy two-port component. (a) unit-cell of actual array. (b) two-port model with both ports active (c) port-1 is active and port-2 is terminated with capacitor (C).

$$\begin{bmatrix} Y_{11} & Y_{12} \\ Y_{21} & Y_{22} \end{bmatrix} \begin{bmatrix} V_1 \\ V_2 \end{bmatrix} = \begin{bmatrix} I_1 \\ I_2 \end{bmatrix} \quad (2.13)$$

$$I_1 = Y_{11}V_1 + Y_{12}V_2 \quad , \quad I_2 = Y_{21}V_1 + Y_{22}V_2 \quad (2.14)$$

A quick inspection of (2.12) and (2.14) reveals the 2×2 admittance matrix as;

$$Y_{11} = Y_{22} = - \sum_{m_x=-\infty}^{\infty} \frac{\text{sinc}\left(\frac{k_{xm} \delta_d}{2}\right)^2}{d_x D_{\infty}(k_{xm})} \quad (2.15)$$

$$Y_{12} = - \sum_{m_x=-\infty}^{\infty} \frac{e^{-\frac{j k_x d_x}{2}} \operatorname{sinc}\left(\frac{k_{xm} \delta_d}{2}\right)^2}{d_x D_{\infty}(k_{xm})} \quad (2.16)$$

$$Y_{21} = - \sum_{m_x=-\infty}^{\infty} \frac{e^{\frac{j k_x d_x}{2}} \operatorname{sinc}\left(\frac{k_{xm} \delta_d}{2}\right)^2}{d_x D_{\infty}(k_{xm})} \quad (2.17)$$

After evaluating (2.15) - (2.17), one gets the 2-port model of the unit-cell. This model can be used to design and optimize a tightly coupled dipole array. Specifically, one port of the model can be terminated with a capacitor (C), effectively turning the double-feed connected array into a single-feed capacitively coupled array. When port-1 is excited with V_1 and port-2 is terminated with a capacitor having admittance of $j\omega C$ (ω : angular frequency), we have the following relation;

$$\begin{bmatrix} Y_{11} & Y_{12} \\ Y_{21} & Y_{22} \end{bmatrix} \begin{bmatrix} V_1 \\ -I_2/j\omega C \end{bmatrix} = \begin{bmatrix} I_1 \\ I_2 \end{bmatrix} \quad (2.18)$$

After solving (2.18) for $Y_1^{in} = I_1/V_1$, we have;

$$Y_1^{in} = Y_{11} - \frac{Y_{12} Y_{21}}{j\omega C + Y_{22}} \quad (2.19)$$

Equation (2.19) gives the input impedance of a tightly coupled dipole array with the coupling capacitor C . When designing an actual array, this expression can be used to do a quick optimization as a starting point without referring to full-wave simulations. Extending this model to multiple loads per unit-cell is quite straightforward. To obtain an

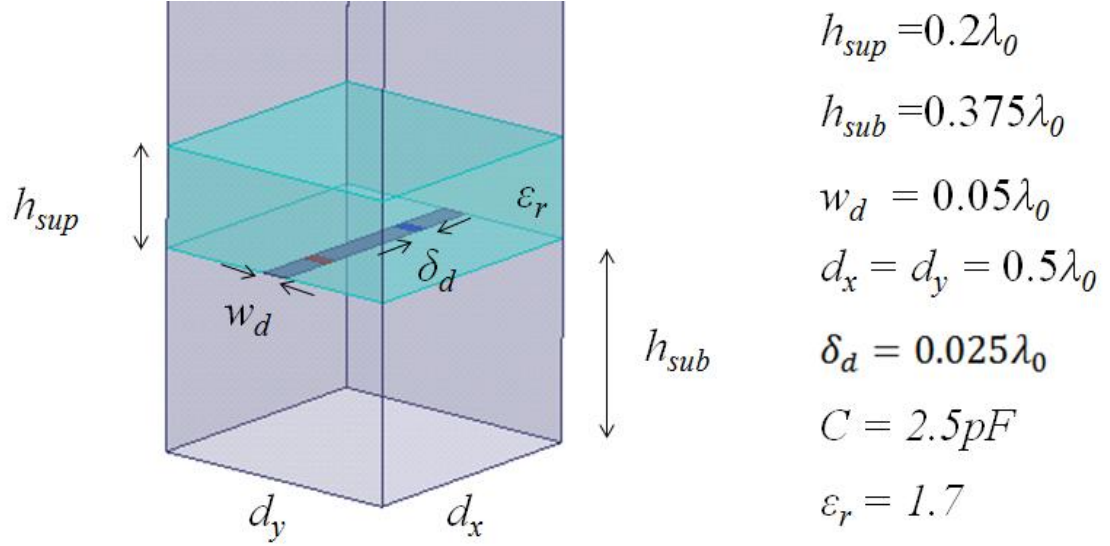


Figure 2.6: HFSS model of the unit-cell of a capacitively coupled dipole array with a dielectric superstrate. The simulation range is $0.2f_0 - f_0$ (0.75-3.75GHz). Coupling capacitor (C) is 2.5pF and λ_0 is wavelength at f_0 . One of the two feeds is terminated by $C=2.5pF$

array with two capacitive loads per unit-cell, one can simply assume a 3-feed unit-cell for a connected array, find 3x3 admittance matrix in a similar way and then excite only one feed port while terminating the remaining two.

As verification, we simulated an infinite capacitively coupled dipole array using *HFSS 15.0* [56] (which is based on vector finite element method [57]-[58]) and compared results with (2.19). The unit-cell is shown in Figure 2.6. Input impedance for different scan angles are plotted in Figure 2.7. As can be seen, the full-wave simulations (which, throughout this dissertation, refer to the results obtained by *HFSS 15.0*) and analytical results have excellent agreement for all scan angles. However, we note that the simulations assumed ideal gap sources and no feed lines, which will be discussed in Section 2.4.

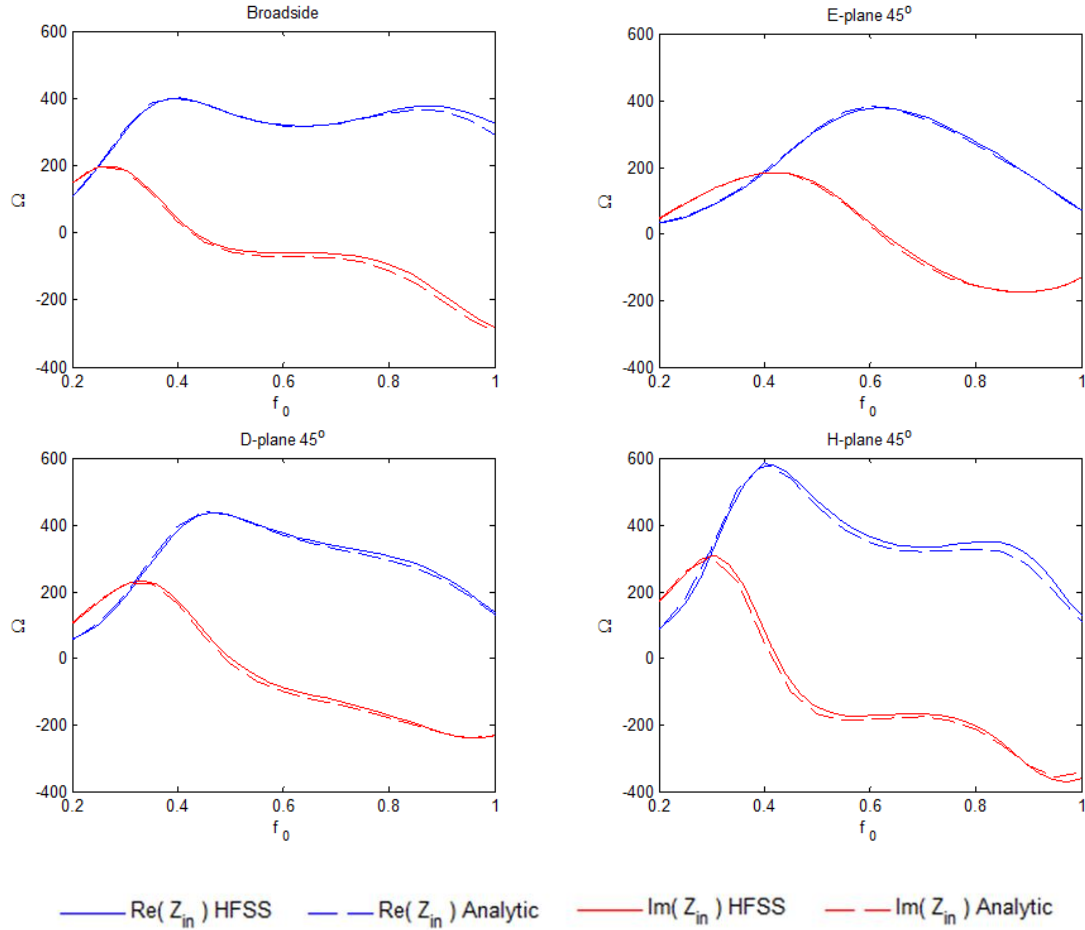


Figure 2.7: Input impedance of analytical model of (2.19) and full-wave model of unit-cell for the tightly coupled dipole array in Figure 2.6. The simulation range is $0.2f_0 - f_0$.

2.3 Approximate Model of Capacitively Coupled Dipole Arrays

In previous section, we reviewed an approach to analytically calculate the input impedance of a tightly coupled dipole array (TCDA). The results were accurate but the approaches provided in Section 2.2.1 or [59] do not give an explicit model like Figure 2.1b with separate components related to different geometrical parameters of the array. Therefore, (2.19) does not present much intuitive information.

Alternatively, we consider a more simplistic and popular model, proposed by Munk [35]. The dipoles are approximated as simple inductors. In the circuit model of the unit-cell, this inductance is connected in series with a capacitor resulting from the coupling to neighboring cells. This series L - C circuit is then connected to transmission lines representing the loading due to ground plane and radiation resistance (see Figure 2.1b). We note that this model [35] is proposed for only design process of broadband wire/dipole arrays. The verification of the results obtained from the circuit model was done rigorously [18], [36] by using a mixture of plane wave expansion and mutual impedance approaches. For the scanning array shown in Figure 2.1a, this L - C approximation can be used when the unit-cell size is less than 0.4λ , assuming low ϵ_1 and ϵ_2 values (< 2) and moderate scan angles ($< 45^\circ$). For higher frequencies and larger scan angles, the accuracy degrades since the operational band gets close to a surface wave frequency, at which the simple L - C model completely fails. The accuracy of this model can be improved by including a shunt capacitance at the active ports, in addition to series L - C . The shunt capacitance is caused by the feed gaps and especially critical for accuracy at high frequencies.

The unit-cell of a tightly coupled dipole array with single layer of superstrate is depicted in Figure 2.8a, with no feeding lines. The capacitor (C_{couple}) in the model is due to coupling between neighboring unit-cells. Z_s and Y_p are self-reactance (inductive) and self-susceptance (capacitive) of the dipole, resulting from higher order Floquet modes. Due to tight coupling between dipoles, we can assume the current along the aperture is almost uniform, making the array behave like a connected array, especially at high

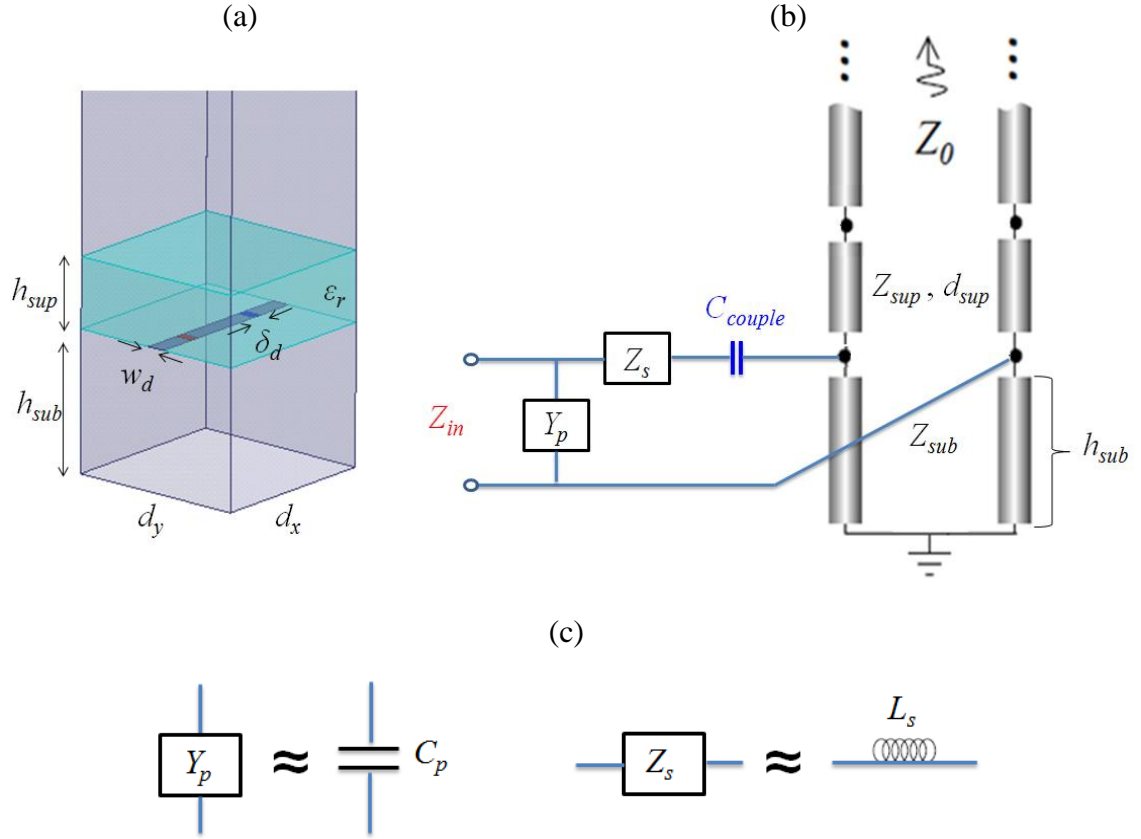


Figure 2.8: Approximate (L - C) model of a tightly coupled dipole array with dielectric superstrate and air substrate. (a) The full-wave model with lump capacitor loading and ideal gap source, (b) Circuit model (c) Low frequency ($d_x, d_y < 0.4\lambda$) approximations to dipole's self reactance.

frequencies. Therefore, the circuit model of an infinite TCDA should be the same with an electrically connected dipole array, except the coupling capacitor (C_{couple}). In other words, we can use (2.7) to calculate reactive part of dipole's input impedance. In fact, (2.7) can be used to extract Z_s and Y_p separately, following the procedure suggested by [39]. Z_s is simply the self inductance of dipole due to its length/width and Y_p is self capacitance due to the feed gap, which can be calculated as follows:

$$Y_p = \frac{1}{d_x} \sum_{m_x \neq 0}^{\infty} \frac{-\text{sinc}^2\left(\frac{k_{xm} \delta_d}{2}\right)}{D_{\infty}(k_{xm})} \quad (2.20)$$

$$Z_s = - \frac{d_x}{d_y \text{sinc}^2\left(\frac{k_{x0} \delta_d}{2}\right)} \sum_{m_y \neq 0}^{\infty} J_0\left(\frac{k_{ym} w_d}{2}\right) G_{xx}^{EJ}(k_{x0}, k_{ym}) \quad (2.21)$$

where $D_{\infty}(k_{xm})$ and $G_{xx}^{EJ}(k_{x0}, k_{ym})$ are calculated by (2.5) and (2.8). We note that $(Y_p + 1/Z_s)$ simply gives the part of (2.7) that is due to higher order modes. The remaining part of (2.7) is due to fundamental mode ($m_x = 0, m_y = 0$), which is represented by the transmission lines (Z_{sub}, Z_{sup}) and the radiation resistance (Z_0) in Figure 2.8b.

The validity of the approximate circuit model in Figure 2.8b was tested for different coupling capacitors and dielectric superstrates (see Figure 2.9 and Figure 2.10). As can be seen, the full-wave (Figure 2.8a) and approximate L - C model (Figure 2.8b) give very similar results for large coupling capacitance values. This is expected since our initial assumption was strong coupling between dipole elements. For small C_{couple} , this assumption obviously does not hold. The weak coupling between neighboring elements significantly alters the current distribution on dipoles such that it is not like the current profile along electrically connected dipoles. Then, using (2.20) and (2.21) for weakly coupled dipole arrays cannot provide accurate results since they give the reactance of electrically connected dipole arrays. However, weakly coupled dipoles are not in the scope of this work since they typically cannot achieve ultra-wideband performance. In other words, the approximate L - C model shown in Figure 2.8b is accurate enough for modeling the dipole elements of wideband arrays, considered in this work.

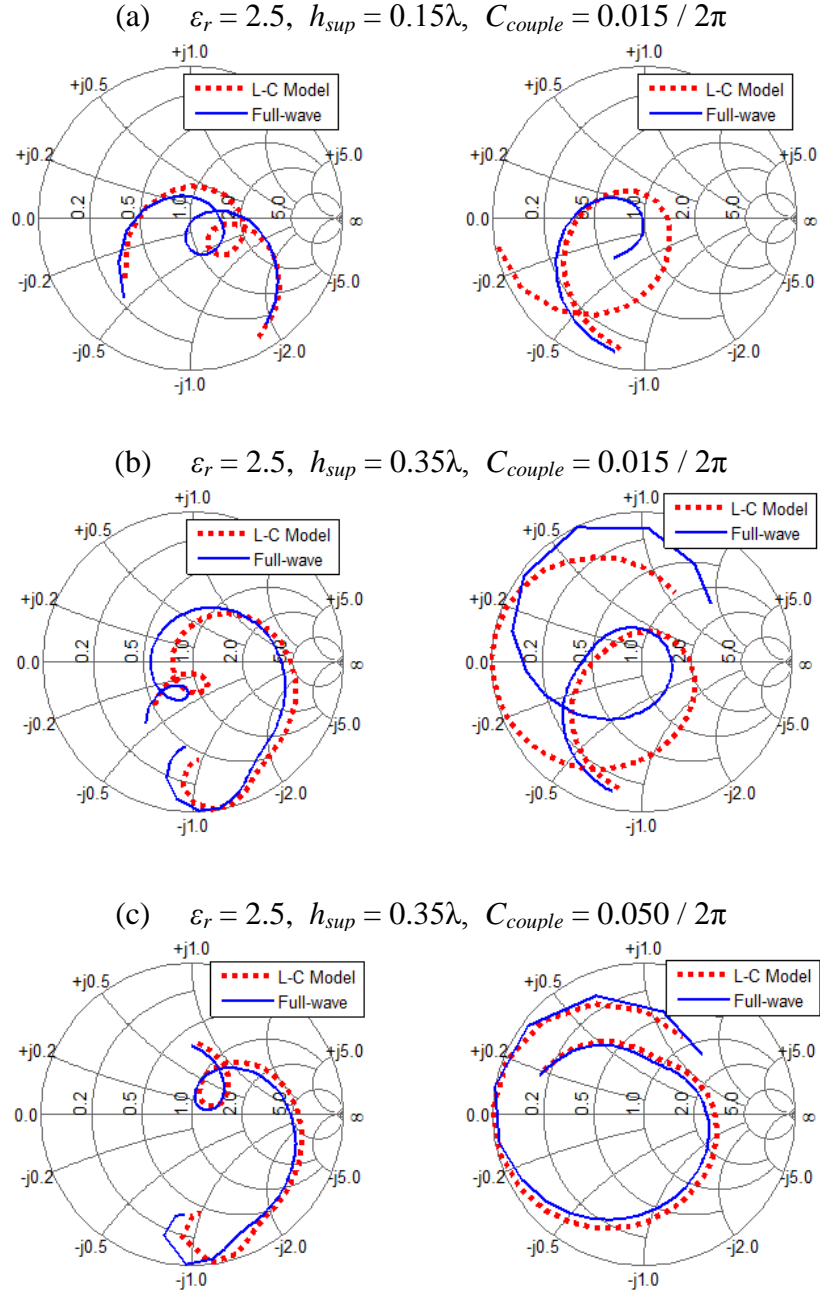


Figure 2.9: Input impedance of a capacitively coupled dipole array during (right) E and (left) H -plane scanning for $\epsilon_r = 2.5$, across normalized frequency range, $0.2 - 1$. The scan angle is 45° . Unit-cell parameters refers to Figure 2.8 and are: $d_x = d_y = 0.5\lambda$, $h_{sub} = 0.35\lambda$, $w_d = 0.05\lambda$, $\delta_d = 0.05\lambda$ at highest frequency ($f = 1$)

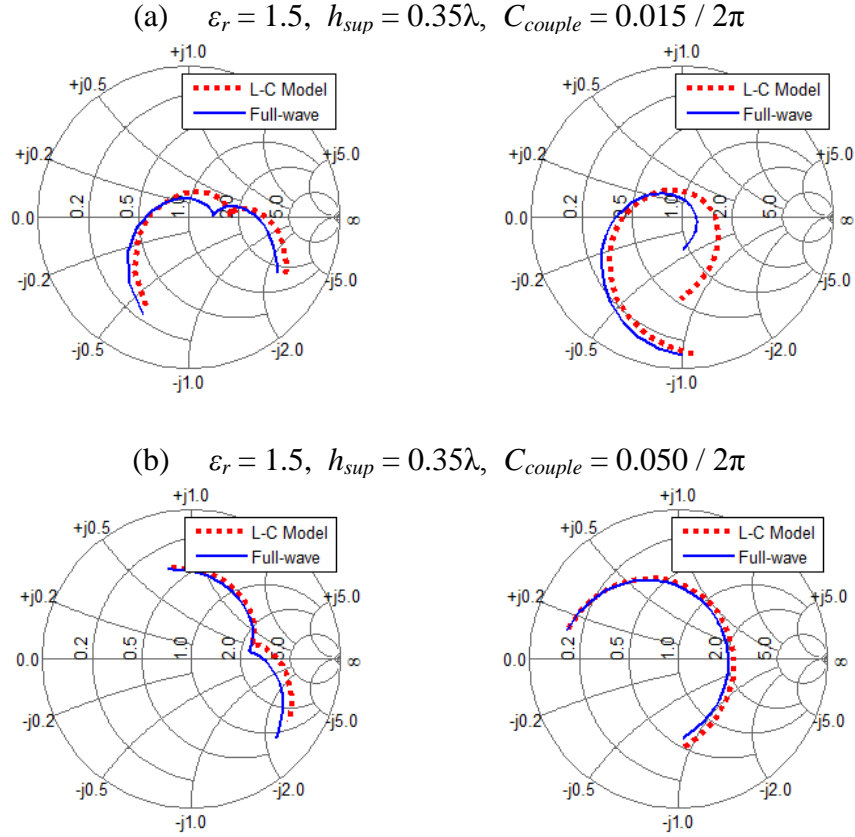


Figure 2.10: Input impedance of a capacitively coupled dipole array during (right) E and (left) H -plane scanning for $\epsilon_r = 1.5$, across normalized frequency range, $0.2 - 1$. The scan angle is 45° . Unit-cell parameters refers to Figure 2.8 and are: $d_x = d_y = 0.5\lambda$, $h_{sub} = 0.35\lambda$, $w_d = 0.05\lambda$, $\delta_d = 0.05\lambda$ at highest frequency ($f = 1$)

2.4 Effect of Feeding Lines

The analytical models, discussed in previous sections, ignored the presence of feeding transmission lines inside the substrate region. Typically, these are vertically placed conductor pairs and can perturb the plane waves propagating around them, unless they are perfect differential pairs and seem invisible to common modes. Common mode suppressing solutions have been proposed to achieve differential feed [40], [45], [46],

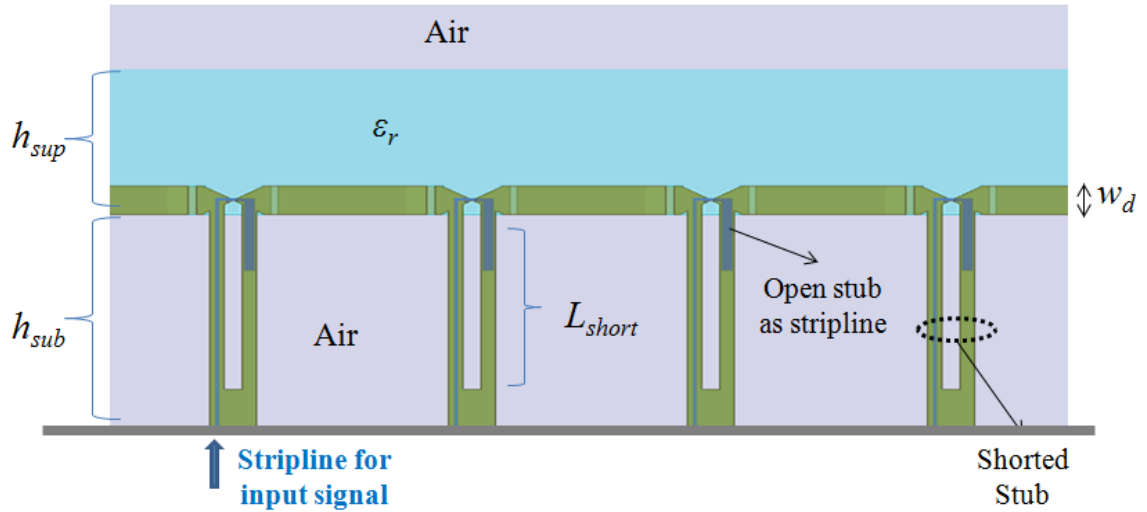


Figure 2.11: Side view of a dipole array with Marchand baluns as feeds. The shorted stub disrupts the uniformity of the substrate, making the analytical models for this region inaccurate during E -plane scanning

[60]. However, these approaches typically suppress the common mode “resonances” on the feed-lines but cannot make the conducting pairs (feed-lines) totally invisible to a propagating plane wave. As a result, the feed-lines will modify the response of the substrate region of the array and make the analytical approaches, presented in this chapter, inaccurate for a practical antenna array in some scanning cases.

One typical example to feed dipole arrays is using folded version of Marchand balun [47]. It basically has two sections of transmission line stubs: Open stub in series and shunt stub in parallel to the input of the antenna. The open stub can usually be implemented as a stripline inside the balun structure, shielded from the substrate region. Shorted stub, on the other hand, is placed vertically beneath the dipoles, therefore exposed to and interacting with the fields in this region.

A generic dipole array with this kind of balun is shown in Figure 2.11 and the simulation results for analytical and full-wave models are plotted in Figure 2.12. For the analytical model, a shorted stub was added in shunt to the input admittance obtained by equation (2.7). As it can be seen, the analytic and full-wave simulations agree fairly well for broadside and H -plane scanning. Only exception is that the actual full-wave model supports a very narrowband common mode along its feed-lines around $f=0.8$, which we do not include in the plots for simplicity since these modes can be suppressed with shorting pins (as will be discussed in the next chapter). For E and D -planes, the results do not match across the entire frequency range, hence exposing the drawbacks of the analytical models for a practical array.

The reason for the mismatch between analytic model and the full-wave simulations can be seen in Figure 2.13. For E -plane scanning, the electric field vectors are fairly uniform along superstrate region and above. For substrate region, there is strong interaction between the balun structure and the propagating fields, resulting in modification of the input impedance of the dipoles.

In summary, one cannot blindly use the analytical models (unless the feed lines are rigorously included in the analysis) to make accurate predictions about impedance response of connected arrays. For an initial prediction, these models can be used to characterize scan conditions that involve TE or TEM modes (H -plane or broadside scanning), for which typical feed lines are almost invisible. For TM modes (E and D -plane) only crude approximations can be acquired. Therefore, a few full-wave simulations should be performed to extract the effects of interaction between feed-lines

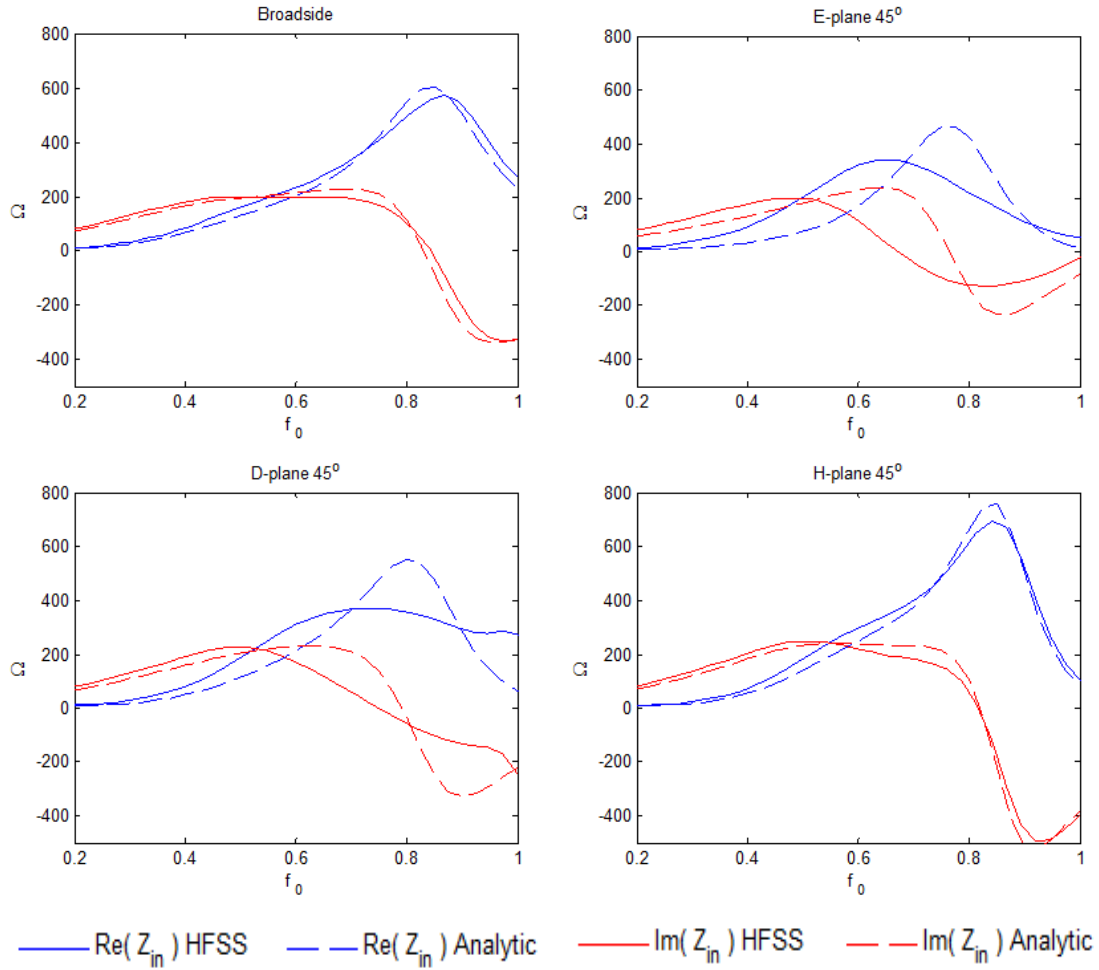


Figure 2.12: Comparison of analytical model and full-wave simulations (*HFSS*) for the infinite connected dipole array, shown in Figure 2.11. For simplicity, open stub is excluded. Array parameters; $d_x = d_y = 0.5\lambda_{\text{high}}$, $h_{\text{sub}} = 0.35\lambda_{\text{high}}$, $h_{\text{sup}} = 0.25\lambda_{\text{high}}$, $w_d = 0.05\lambda_{\text{high}}$, $L_{\text{short}} = 0.23\lambda_{\text{high}}$, $Z_{\text{short}} = 330\Omega$

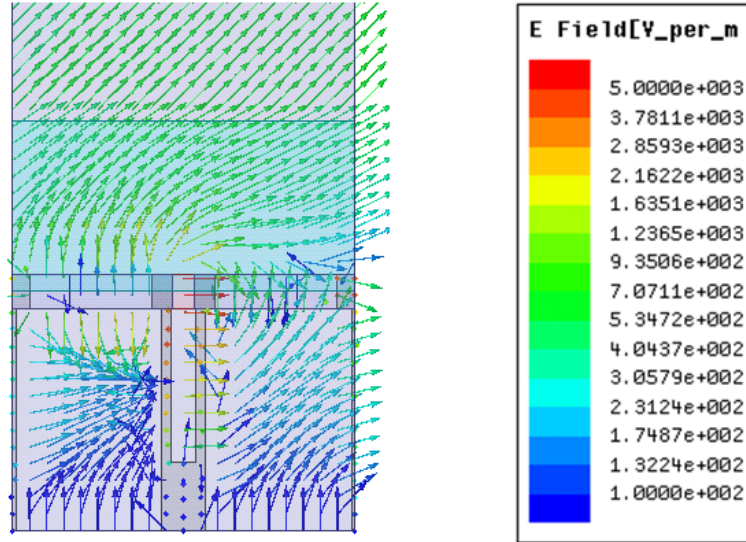


Figure 2.13: Electric field vectors for 45° scan angle in E -plane. Uniform plane wave propagation is clearly visible in superstrate region and above. For substrate region, feed lines disturb the propagating fields. This is not accounted for in the analytical models.

and TM modes for the antenna geometry of interest. After these initial full-wave simulations, a better estimation of impedance behavior due to feed-lines can be acquired and inserted into the circuit models for optimization.

2.5 Summary

In this chapter, tightly coupled dipole arrays were discussed in detail. Recent analytical models from the literature were reviewed and compared for different design considerations. Since these models do not consider vertically placed feed-lines inside unit-cell volumes of the arrays, we also did full-wave simulations to check their accuracy for more realistic cases. Based on these simulations, we verified that, feed-lines have minimum effect when the fundamental Floquet mode does not have electric fields with vertical components. In other words, the analytical models can be used with high

accuracy for TE and TEM modes (H -plane and broadside scanning) but not for TM modes (E and D -plane scanning). This is due to the fact that, vertically placed feed-lines in the substrate region interact with vertical components of the electric field, which is only the case if the propagating plane wave has a TM component (unless the wave is pure TEM, indicating broadside radiation).

Chapter 3 Frequency Selective Surfaces (FSS) as Superstrate for Tightly Coupled Dipole Arrays (TCDA)

In Chapter 1, we discussed some of the challenges and solution approaches for designing wideband, wide-angle connected/coupled arrays and mentioned that a typical dipole array employs dielectric layer(s) above aperture for wide-angle impedance matching. In this chapter, we discuss how printed parasitic elements, instead of dielectric materials, can be used as superstrates. Throughout this dissertation, we will refer to these elements as frequency selective surfaces (FSS), even though the ones considered here are working below their cut-off frequency and has capacitive response.

This chapter is organized as follows: First we will provide a few examples of different FSS geometries. In Section 3.2, we will investigate one of these structures together with a dipole array over a ground plane. Then, in Section 3.3, we will discuss how to design a fully operational TCDA with FSS loading and integrated feed. In Section 3.4, we will propose a modification to the well-known folded Marchand balun to improve its matching efficiency when used in a practical dipole array. In Section 3.5, we will present simulated performance of the optimized FSS-loaded array with integrated balun. Our conclusions are given in Section 3.6

3.1 Dipole Arrays with FSS

Distributed, metallic structures with electrically small periodicities have been used as artificial dielectrics in various applications. They were employed to design delay lines and obtain light-weight lenses as early as 1940s [68]. Simple operational principle can be understood if one considers small metallic particles as distributed shunt capacitive loads for a propagating wave. The equivalent response can be modeled by a medium with equivalent dielectric constant, which is higher than the case where there is no metallic particles [68]-[69].

Recently, printed versions of these structures have been used to improve antenna gain/pattern [70] or to suppress surface waves [72] in connected arrays (e.g. long slot antennas). Accurate analytical models have also been proposed [71]-[72] to represent these structures with equivalent anisotropic dielectric mediums. This can be helpful during preliminary antenna design process. However, these models assume extremely small lattice size for the periodic elements (as small as 0.01λ), which may not be practical to implement for many antenna arrays. Therefore, we will not consider these layers with small lattice sizes. Instead, we will focus on FSS structures with only a few layers. Furthermore, we will study the cases where antennas (dipoles) and the FSS layers are integrated together, rather than analyzing them separately.

In Figure 3.1, a connected dipole array is shown together with various superstrate layers. Some of the interesting features of these geometries are as follows: The ones in Figure 3.1-(b) and (c) are light-weight structures due to the lack of a thick dielectric slab. FSS layer of Figure 3.1-(b) is simplest to fabricate since it can be placed on the same

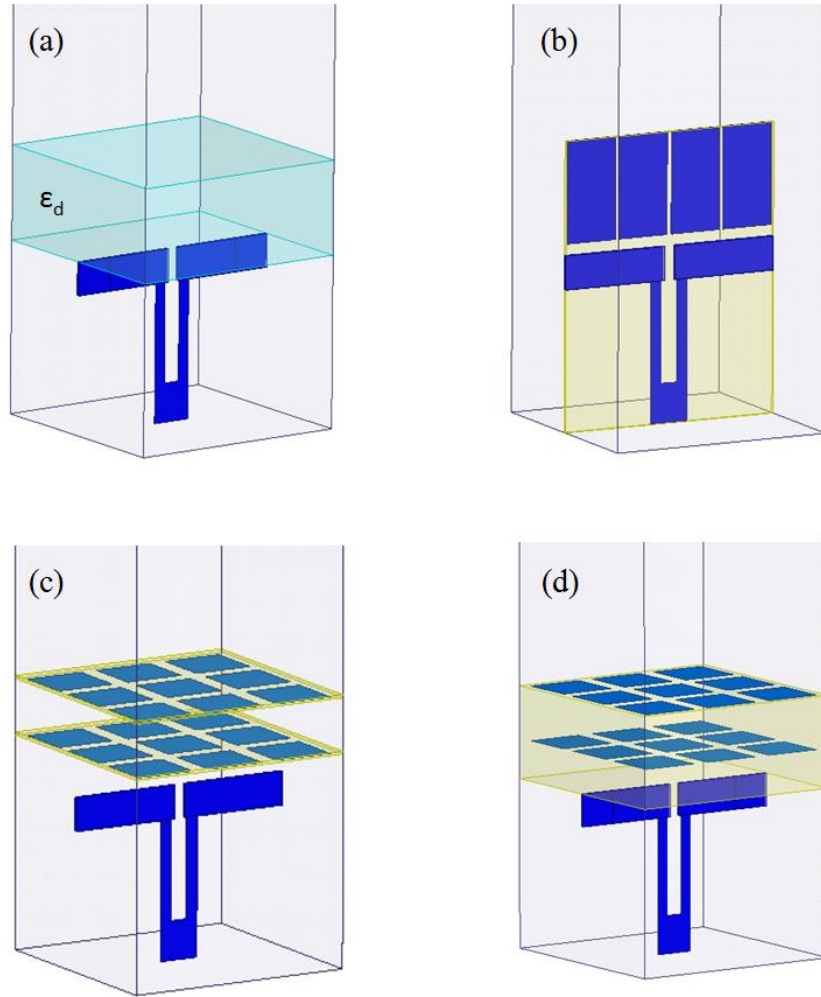


Figure 3.1: Unit-cell of a dipole array with different superstrate layers (a) isotropic dielectric slab, (b) Vertical metallic patches located on the same PCB with the dipoles, (c) Conformal metallic patch layers with air gap, (d) Metallic patches embedded in a dielectric medium.

printed circuit board (PCB) with the dipole and balun. We also note that Figure 3.1-(c) and (d) are the same geometries discussed in [71], only with larger lattice sizes for superstrate layers. These structures are anisotropic and have different response to TE and TM waves, providing more freedom when designing the antenna to be simultaneously impedance matched for E and H -plane scanning.

3.2 Vertical Patches as FSS superstrate

In this section, we further investigate the tightly coupled antenna-FSS pair (see Figure 3.1-b) using *HFSS 15.0*, and compare its performance with the reference case of Figure 3.1-(a). For simplicity, we did not include the feed lines and just studied coupled dipoles with the superstrate layers, assuming PEC for the conducting surfaces. We note that using copper instead of PEC for the FSS causes $\sim 0.1\text{dB}$ extra ohmic loss, indicating minimal efficiency degradation. This is due to the fact that FSS layer is always operating below its resonance frequency implying that there is no strong resonant currents along its surface. We also note that if FSS is going to be used instead of the dielectric superstrate in an antenna array, then it needs to have at least similar (if not better) frequency/angular response in the array environment.

During parametric full-wave simulations, only the superstrate layers were modified. Ground plane height and dipole dimensions were all the same and kept constant for both arrays. Some of these constants are as follows: $0.9\text{GHz} < f < 3.75\text{GHz}$, $d_x=d_y=4\text{cm}$, $h_{sub}=3.5\text{cm}$ and $w_d=4\text{mm}$ (see Figure 3.2 - Figure 3.5). Note that d_x, d_y are half-wavelength at the highest frequency, which is typical for a wideband phased array. The changing parameters were ϵ_d and h_l for dielectric slab and g_{FSS} for FSS layer.

The simulation results for the input impedance response of both arrays are depicted in Figure 3.2 - Figure 3.5. Comparison of the two sets of plots reveals that impedance locus of the FSS array is more confined compared to the dielectric-loaded array, implying better efficiency during scanning. More detailed inspection shows the main difference is at the higher end of the band. As the frequency increases, dielectric-loaded arrays detune

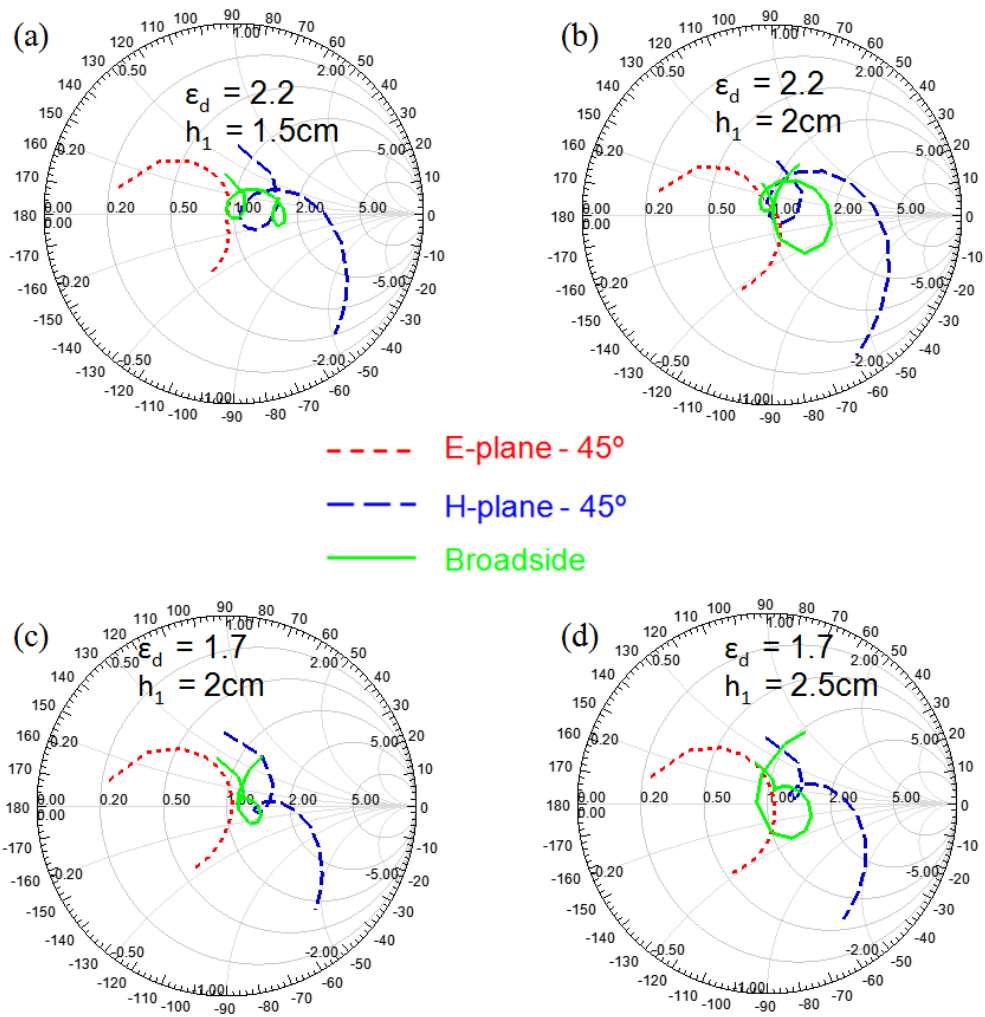
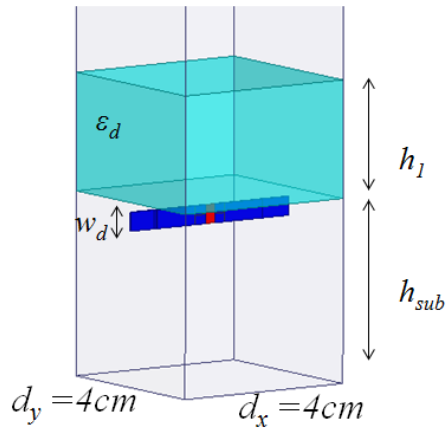


Figure 3.2: Impedance response of the dielectric loaded TCDA is shown for different dielectric constant and slab thickness when scan angle is less than 45°. Frequency range is 0.9-3.75GHz for all four cases.

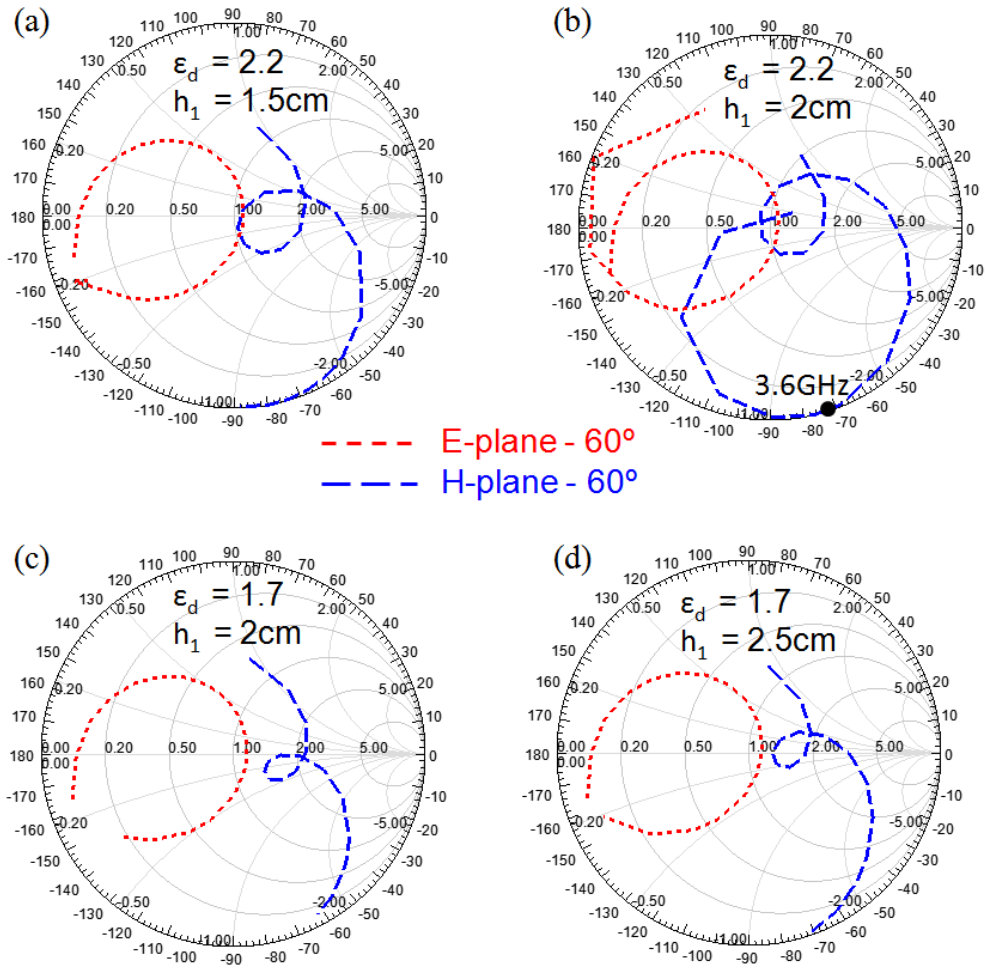
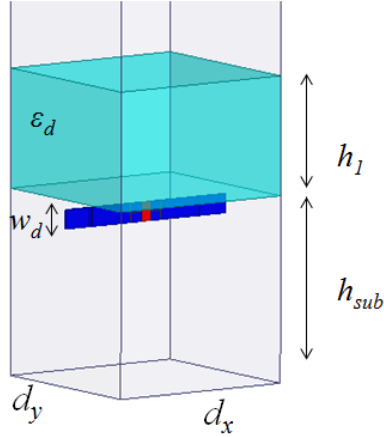


Figure 3.3: Impedance response of the dielectric loaded TCDA is shown for different dielectric constant and slab thickness when scan angle is 60° . Frequency range is 0.9-3.75GHz for all four cases.

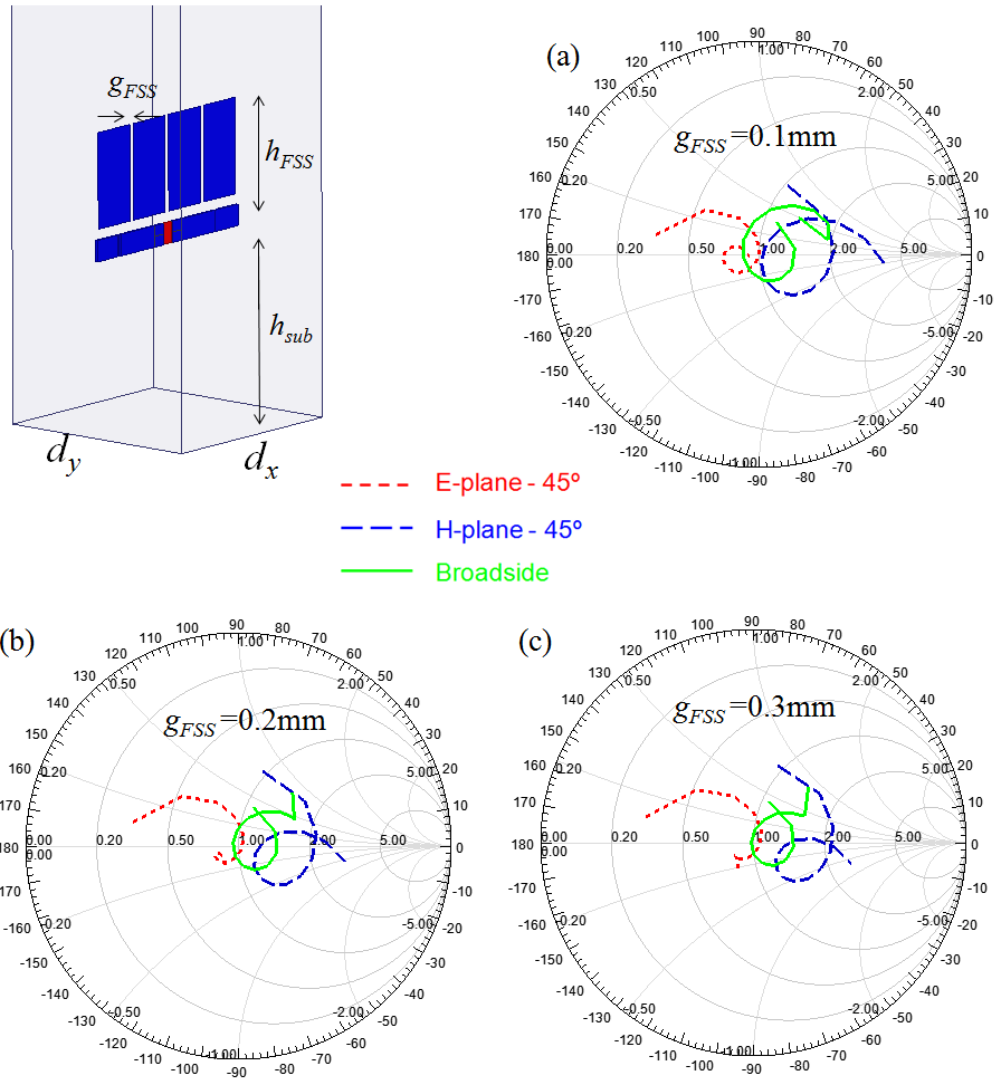
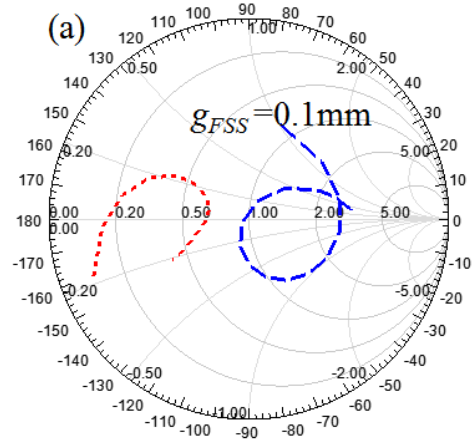
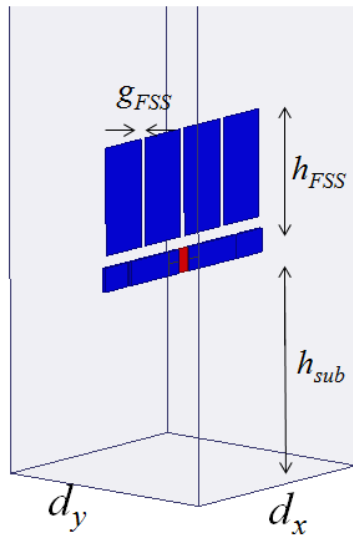


Figure 3.4: Impedance response of the FSS loaded TCDA is shown for different g_{FSS} values when scan angle is less than 45° . The height of the FSS layer, h_{FSS} , is 2cm and frequency range is 0.9-3.75GHz for all three cases.



- - - E-plane - 60°
 - - - H-plane - 60°

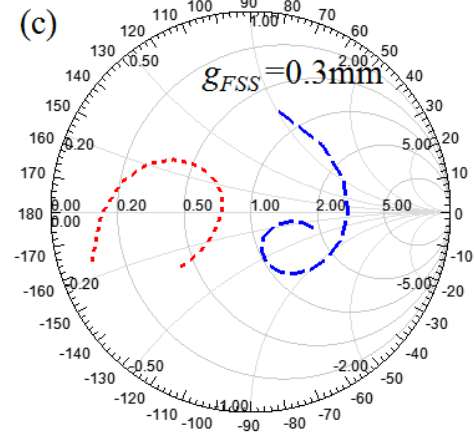
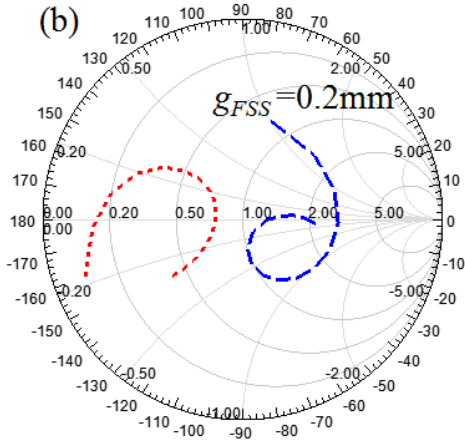


Figure 3.5: Impedance response of the FSS loaded TCDA is shown for different g_{FSS} values when scan angle is 60° . The height of the FSS layer, h_{FSS} , is 2cm and frequency range is 0.9-3.75GHz for all three cases.

since higher order modes start to dominate. Detuning is more obvious at larger scan angles (60°), particularly for higher contrast dielectric ($\epsilon_r = 2.2$), as the reflection coefficient becomes unity at higher end of the band. This is expected since it is easier for any higher order mode to couple to a guided surface wave mode when the substrate or superstrate material is thicker or has higher dielectric constant [11]. This results in no radiation and total impedance mismatch.

3.3 TCDA with Integrated Marchand Balun and FSS

Based on the results from previous section, the FSS shown in Figure 3.1-(b) can provide better scanning performance than a conventional isotropic dielectric slab. In this chapter we will present a fully operational array, including feed lines integrated with the dipoles (active) and FSS (parasitic) elements.

A major challenge in designing a wideband phased array is implementing practical differential feed structure in limited space. Typically, these are vertical conductors that are required to fit inside the substrate region, under the radiating elements. One of the recent approaches is using folded Marchand balun, as suggested in [46] and [48]. However, the unit-cell of these TCDA usually has two small dipoles (*split unit-cell*), hence two baluns, which are fed by a 2-way power divider. As discussed before in Chapter 1, this will cause resistive losses during E -plane scanning. Therefore we will use single dipole/balun in each unit-cell to avoid these ohmic losses.

Unit-cell of the proposed TCDA with FSS superstrate is depicted in Figure 3.6. It is a single-pol array, implemented using three-layer PCB technology. Three copper layers are hosted by two RT/duroid[®] 5880 (20mil, $\epsilon_r = 2.2$) substrates. These layers are bonded

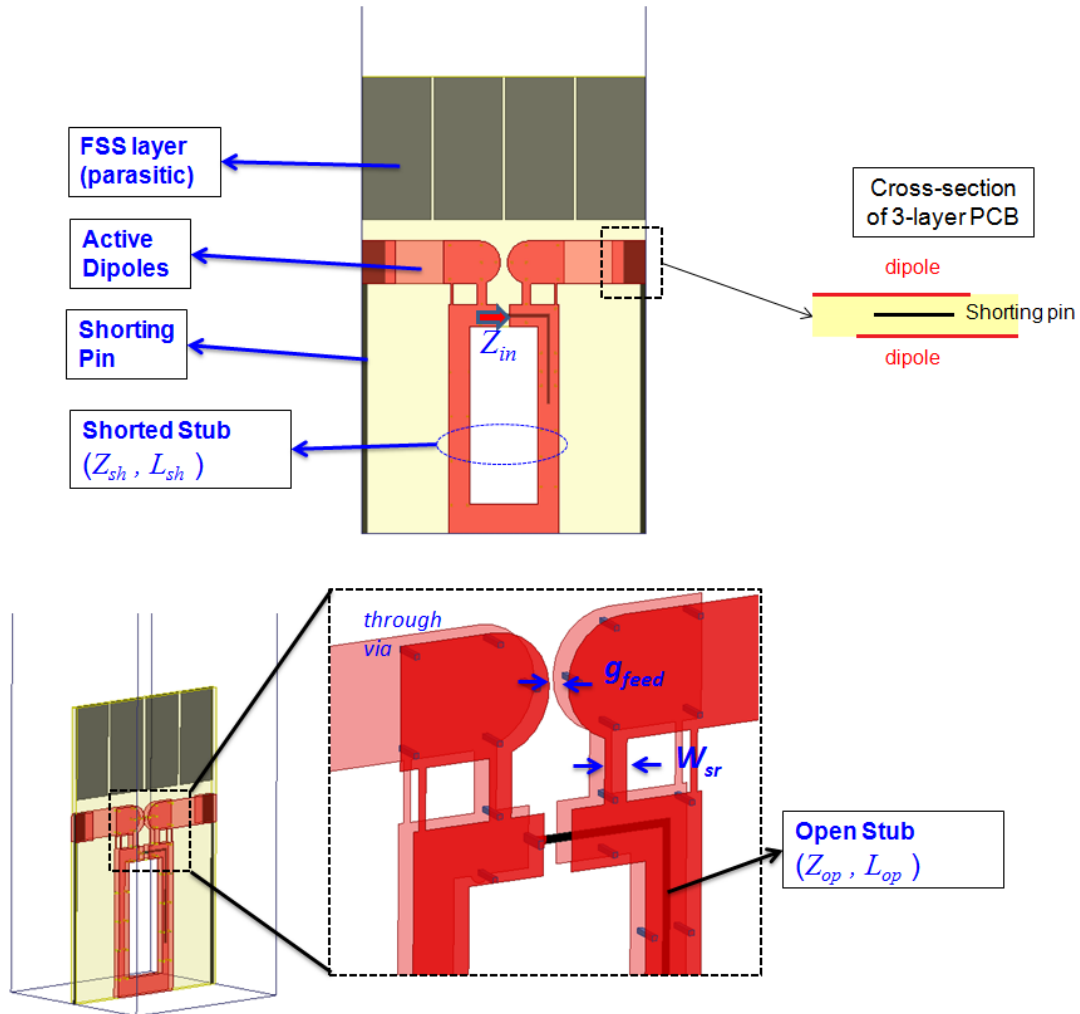


Figure 3.6: Unit-cell geometry of a TCDA with FSS superstrate and Marchand balun. All of the elements are implemented on a 3-layer PCB, vertically placed over a ground plane.

using a 4mil polyflon material, resulting in 44mil overall thickness. The open stub of Marchand balun is implemented as a stripline, shielded inside the shorted stub. The FSS superstrate and the shorting pins are printed on the middle copper layer. The dipoles are on the outer layers, overlapping along the top side of shorting pin to achieve capacitive coupling to each other and to the shorting pin. Below are the summary of the function of each unit-cell element;

- **FSS Superstrate:** Used for wide-angle and wideband impedance matching, similar to a dielectric slab, by providing capacitive loading (depending on the gap between vertical conductors forming the FSS) to the dipoles. It reduces the variation in scan impedance seen by the dipole aperture and mitigates the effect of ground plane.
- **Marchand Balun:** Provides balanced excitation to the dipoles. It also serves as a 2-stage impedance matching circuit. The parameters (Z_{sh} , L_{sh} , Z_{op} , L_{op}) of the shorted and open stub can be tuned together with other elements to improve impedance bandwidth.
- **Shorting Pins:** These are used to suppress common mode resonances at the higher end of the frequency band, as discussed in [42] and [43]. Even though the balun provides differential excitation for most of the bandwidth, there can still be resonating common modes if the separation between neighboring baluns/feed-lines is big enough. These shorting pins are basically used to “crowd” the ground plane so that the distance between vertical conductors along the ground plane is smaller. This way the resonance frequency can be pushed to higher values, out of the band of interest.

Before discussing the design of the impedance transformer, we further elaborate on the function of shorting pins. To show its effect, the infinite array is simulated with/without the pins and the resulting VSWR is depicted in Figure 3.7. We observe that the absence of shorting pins causes a very sharp peak in VSWR when the unit-cell size is about 0.4λ . The reason for this is that the feed lines support a strong non-radiating common mode

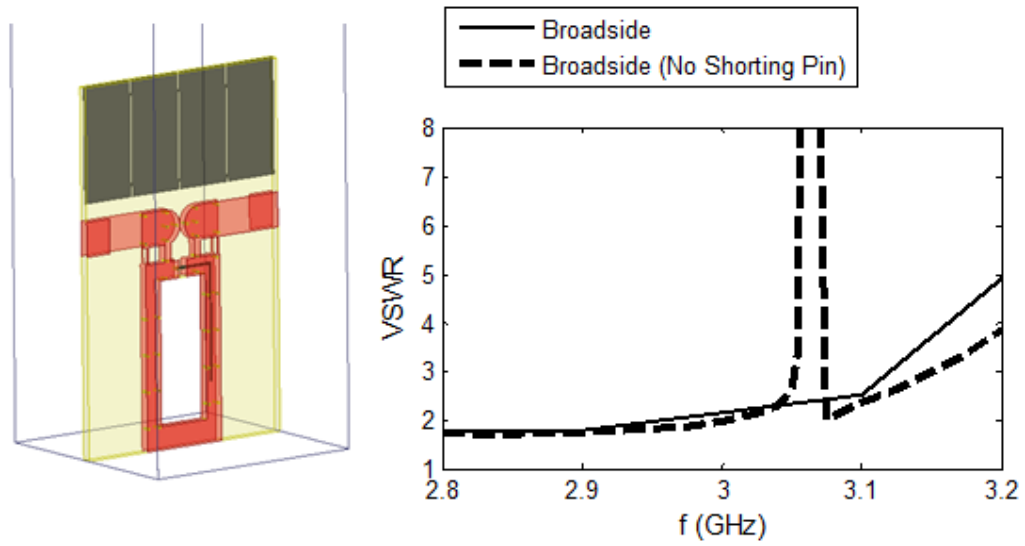


Figure 3.7: VSWR of the infinite array with and without the shorting pin.

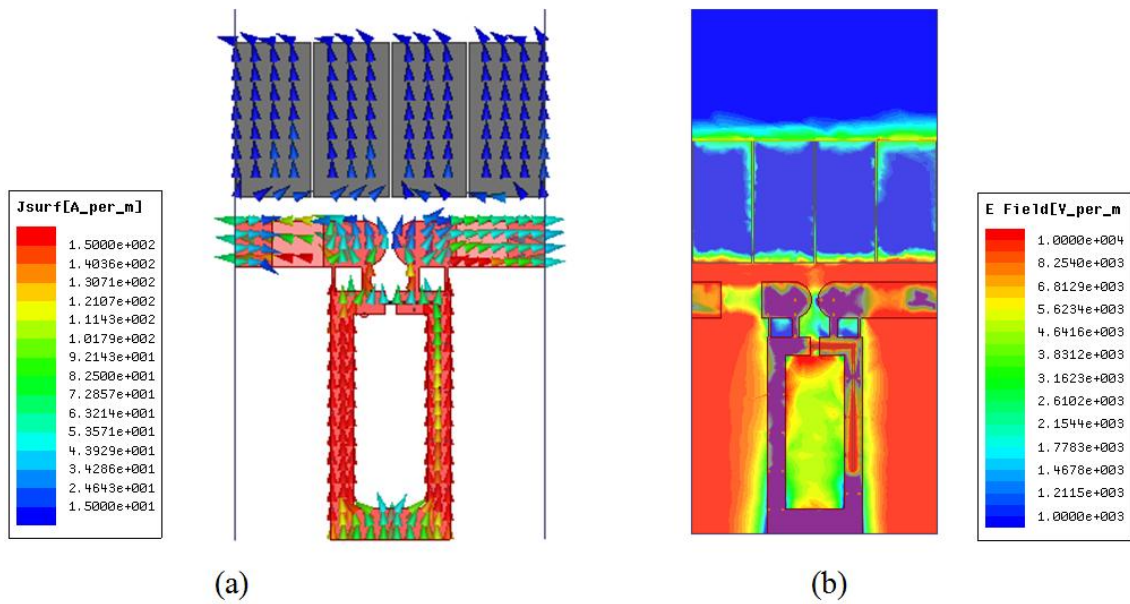


Figure 3.8: The field distribution in the unit-cell without shorting pin, at resonance frequency. (a) Current distribution along the conductors. (b) Electric field inside the unit-cell volume

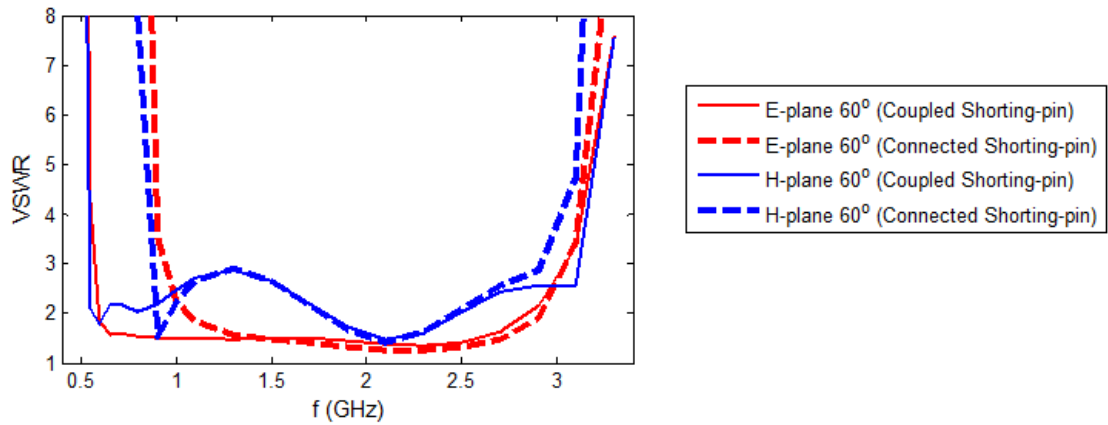


Figure 3.9: VSWR of the infinite array during scanning in E -plane and H -plane when the shorting pins are capacitively “coupled” or electrically “connected” to the dipoles.

along them, causing the impedance to be purely reactive. The resulting electric field distribution in the unit-cell is shown in Figure 3.8. It can be seen that there is no radiation and the electric-field is mostly confined to the substrate region.

As mentioned before, the shorting pins are placed in the middle layer of the PCB, without any contact to the dipoles. Instead of electrical connection, they are capacitively coupled to the dipole arms on outer layers, similar to [43]. This helps the performance of the dipoles on lower end of the bandwidth: When the shorting pins are electrically connected to the dipole arms, they create resonant loops with the balun and ground plane at low frequencies, as discussed in [41]. However, when placed on the middle layer, they are practically along the virtual ground of differentially excited neighboring dipole arms. Therefore, coupling to pins is minimal and has not as much effect on impedance behavior of the dipoles. The reduced bandwidth due to the loading from electrically connected

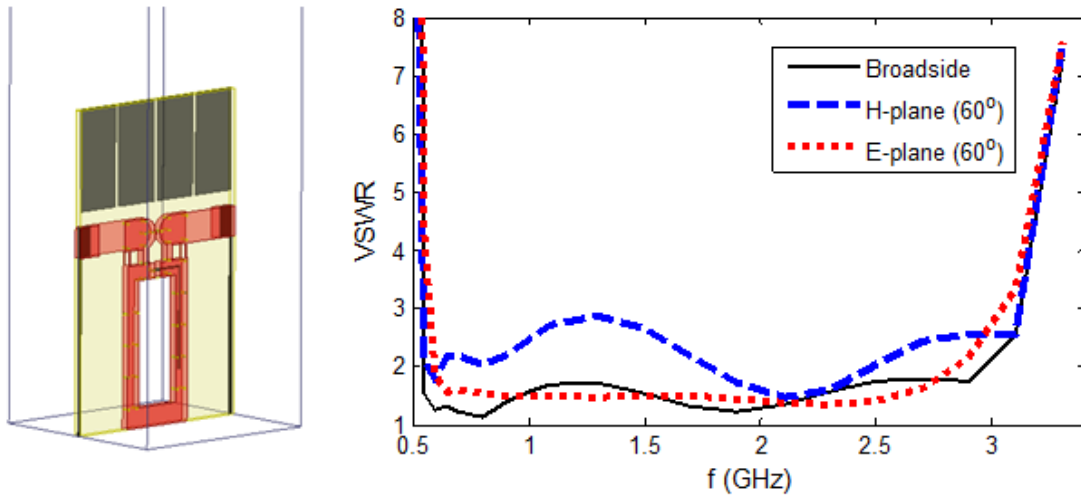


Figure 3.10: VSWR of the optimized infinite array excited by ideal gap source. The source impedance is around 150Ω .

shorting pins is shown in Figure 3.9. Capacitively coupled pins move the lowest frequency from 0.9GHz to 0.5GHz, hence extending the available bandwidth.

Wideband impedance performance was achieved by co-designing and tuning capacitively coupled dipoles, ground plane height, printed FSS layer and the Marchand balun. We note that the FSS superstrate was chosen to operate well below its resonance frequency. This is necessary as it is intended to provide shunt capacitance for a plane wave propagating along (or close to) the z -axis. This reduces the characteristic impedance of the medium, in the same manner as a dielectric superstrate does. Added capacitance mitigates the inductive loading due to the ground plane.

The array is excited by a gap source at this point; no realistic feed-lines for connection to a standard 50Ω source are included. Optimum value of input impedance for the gap source, shown as Z_{in} in Figure 3.6, is around 150Ω . So the balun, dipoles and FSS are

tuned to maximize the bandwidth for this impedance value. The resulting VSWR data for different scan angles are shown in Figure 3.10. As it can be seen, the bandwidth is more than 6:1 when scanning 60° from broadside. Instead of the gap source, a tapered strip-line can be employed to transform 150Ω down to standard 50Ω , which will be discussed in next sections.

3.4 Modified Marchand Balun for Improved Impedance Matching

In the previous section, the optimum value for Z_{in} was found to be around 150Ω . This value should be tapered down to 50Ω by a stripline, going through the Marchand balun and below the ground plane. However, 150Ω is too high for a practical stripline. Typically the highest characteristic impedance (Z_0) values are around 100Ω . To address this problem, we placed rectangular perforations (see Figure 3.11) on the two ground layers of a stripline to increase the achievable characteristic impedance (Z_0). Corresponding Z_0 values for different perforation dimensions are shown in Figure 3.12. As it can be seen, the maximum characteristic impedance can be easily increased from 110Ω to more than 160Ω for the same fabrication tolerances.

A possible drawback of the perforated stripline is the lack of shielding for the inner conductor. This may cause coupling to the substrate region and excitation of a resonant common mode. To examine this, we simulated the TCDA using a perforated balun for multiple scan angles. The resulting electric field distribution inside the signal line of the balun and the substrate region is depicted in Figure 3.13. This plot refers to the case of 60° scan angle in the E -plane with 0.4λ unit-cell size, which was around the common mode frequency (Figure 3.7) in case of no shorting pins. As shown, the electric field of

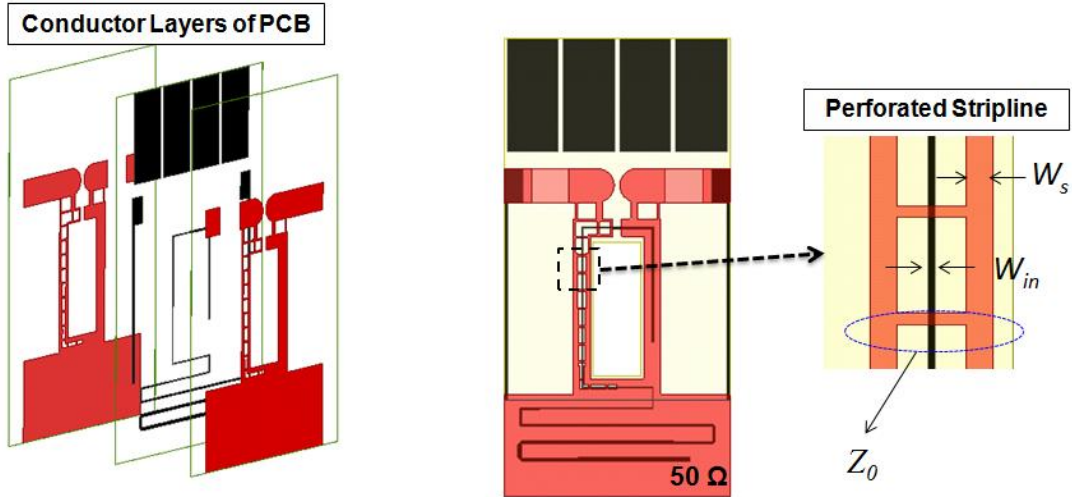


Figure 3.11: The outer conductor of the stripline (going through the balun) is perforated to increase the characteristic impedance.

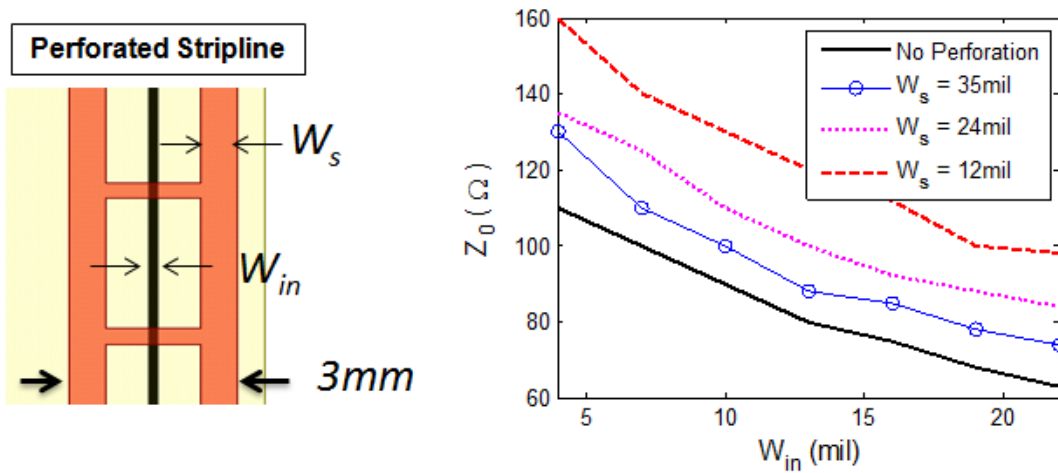


Figure 3.12: Characteristic impedance of the stripline with perforated outer conductor. The PCB board has 44mil total thickness, 3mm total width and a substrate with dielectric constant of 2.2.

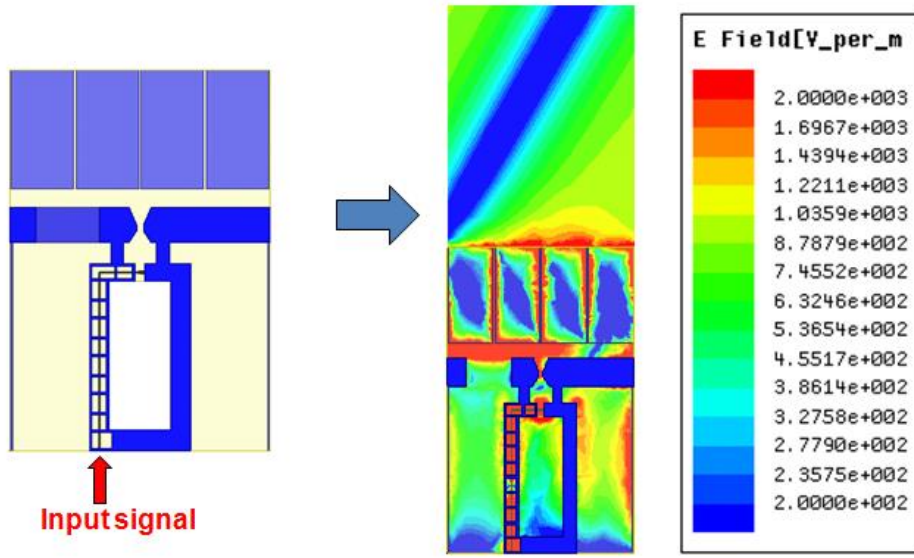


Figure 3.13: Electric field distribution of unit-cell when scanning 60° in E -plane. The unit-cell size is 0.4λ

the incoming stripline is well confined inside the balun. This indicates that perforating the balun may not be an issue. However, resonances can still exist if the separation between feed lines of neighboring unit-cells is large enough to support a common mode. To address this, we used shorting pins at the boundaries of the neighboring unit cells (as mentioned before), in an effort to suppress possible resonant common modes.

3.5 Optimized Antenna: Geometry and Simulated Performance

In previous sections, the optimum input impedance for the tuned array was found to be around 150Ω . To match this array to 50Ω , we designed an 18-section stepped transformer as part of the stripline feed. The electrical length of each section was 18° at 1GHz, making them 1cm each for the PCB substrate ($\epsilon_r = 2.2$). This 18cm-long transformer included the meandered line below the ground and the perforated stripline on one side of

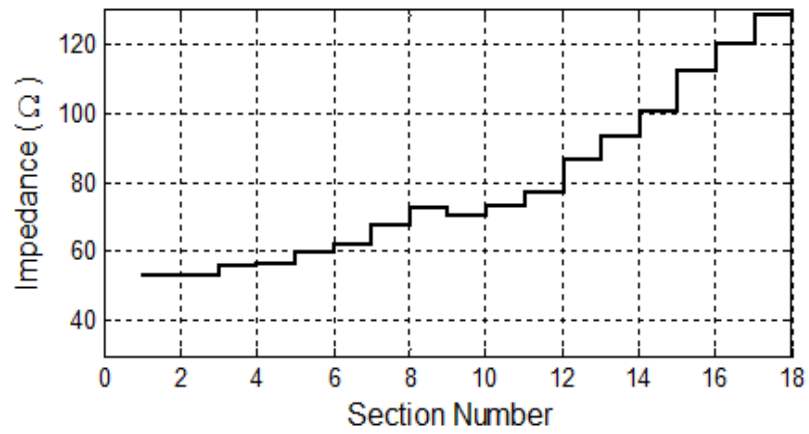


Figure 3.14: Impedance profile of 18 sections of stepped transformer that matches TCDA input to 50Ω.

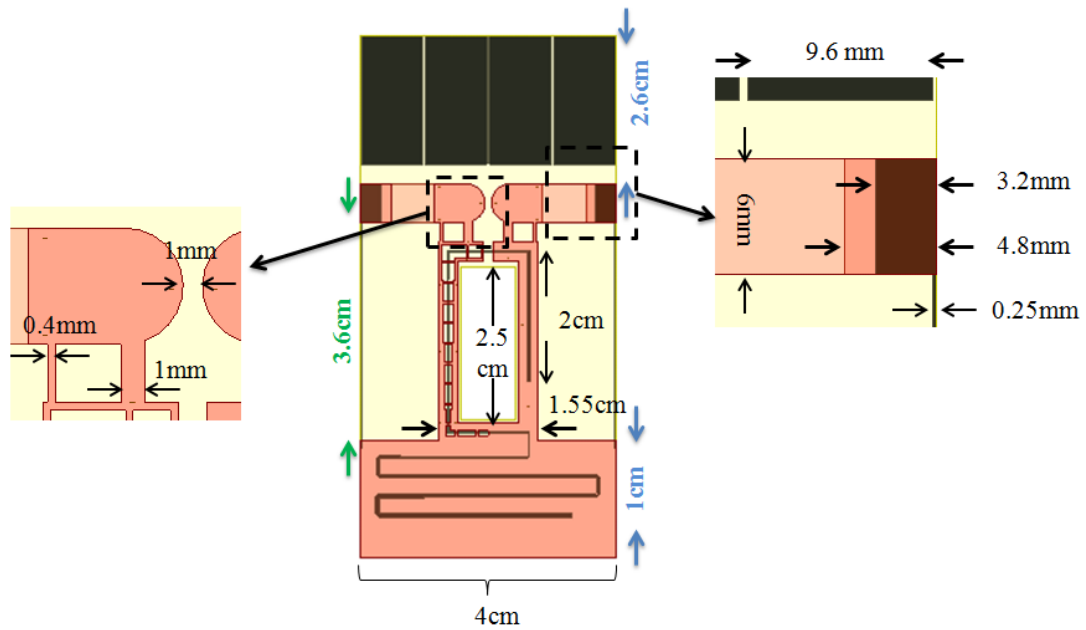


Figure 3.15: Physical dimensions of the fully optimized unit-cell.

the balun (Figure 3.11). The impedance profile of the transformer is plotted in Figure 3.14. As shown, the optimized curve resembles an exponential function, indicating that a continuous, exponentially tapered line could also be used. The physical dimensions of the fully optimized array are shown in Figure 3.15. We note that the TCDA array and the transformer were designed separately. Because of this, there is a small decrease in efficiency as compared to the case when the TCDA is excited by a gap source. This is because the meandered feed line is not an ideal transition between 50Ω and 150Ω . We also note that the meandered line is much longer than it would have been if it was designed synergistically with the other elements (dipole, FSS etc.) of the unit-cell. Therefore, the performance of the array in terms of overall height and efficiency can be further improved. However, the scope of this work is not miniaturizing the array thickness and the achieved bandwidth/efficiency performance is sufficient to demonstrate the potential of the proposed FSS superstrate.

The simulated mismatch efficiency of the TCDA with the FSS, balun and transformer is given in Figure 3.16. We observe that for scan angles of $\theta \leq 45^\circ$, the bandwidth is 6.5:1 (0.5-3.25GHz) with $VSWR < 3.2$ (1.4dB mismatch loss). For $\theta \leq 60^\circ$, the bandwidth reduces to 6.4:1 assuming the same efficiency level. When scanning beyond 60° , we observe some additional mismatch losses, up to 2.5dB for the H -plane. Concurrently, E & D -plane mismatch efficiency is still better than -1dB for most of the bandwidth.

The normalized cross-polarized gain in the D -plane was calculated using Ludwig's third definition [61] and is shown in Figure 3.17. As seen, the normalized cross-pol gain is around -14dB at 45° and -9dB at 60° scans except at the very high end of the 0.5-

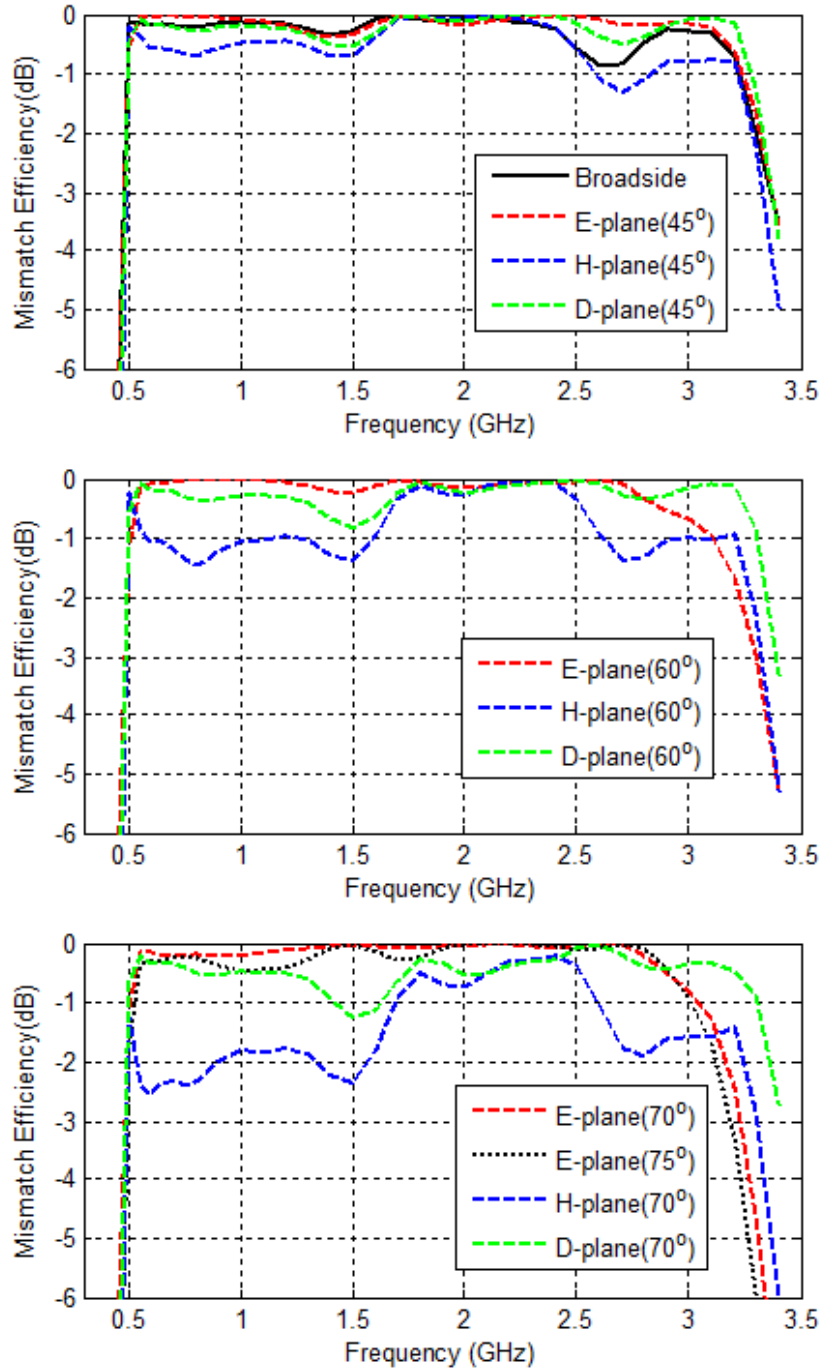


Figure 3.16: Mismatch efficiency of optimized TCDA for various scan angles along principal and intercardinal plane.

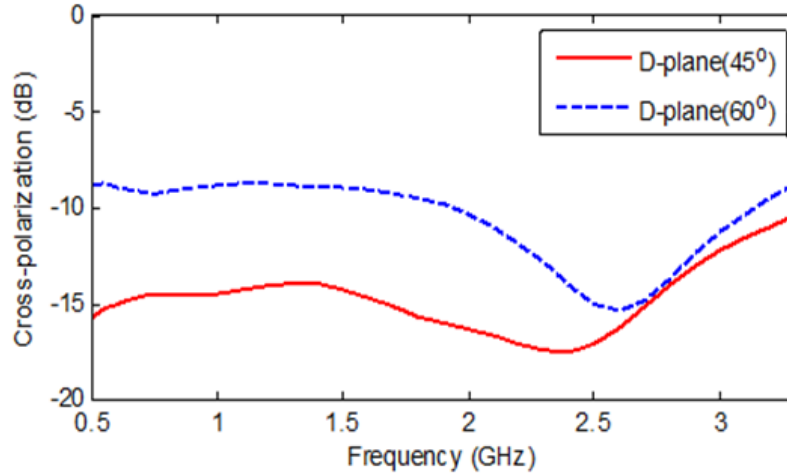


Figure 3.17: Normalized X-pol radiation based on Ludwig's 3rd definition [61].

3.25GHz band. These values are close to the ideal linearly polarized dipole apertures where the cross-pol levels are -15dB and -10dB, at 45° and 60° respectively. Degradation of 1dB is due to the vertically oriented conducting sheets in the FSS layer. However, reduced polarization purity above 2.7GHz is caused by the feed structure starting to support common modes due to a resonance around 3.5GHz (out of the intended band). As already noted, this issue can be addressed by small reduction in the distance between the shorting pins and the balun legs, and re-tuning the unit-cell parameters for the same bandwidth. However, for the scope of this chapter, the cross-pol level below -9dB for scan range $\theta \leq 60^\circ$ was acceptable and no further attempts for improvement were made.

3.6 Summary

A novel tightly coupled dipole array with integrated feed and FSS superstrate was presented. The feed structure was the widely used folded Marchand balun, but modified to facilitate wideband matching at large scan angles. The impedance bandwidth was

found to be more than 6:1 when scanning 75° in E -plane and 60° in H -plane. The FSS consisted of one conducting layer, which can be placed on the same PCB as the radiating elements and the feed lines. No dielectric slab was used for scan impedance compensation, implying a simple, light-weight and low-cost array structure. We note that, additional circuitry for T/R modules or phase shifters can be placed on the same PCB extending below the ground plane, providing an extremely compact/integrated scanning array.

To our knowledge, the proposed TCDA is the first low-profile design to achieve more than 6:1 bandwidth with such wide scan angles (75° in E -plane and 60° in H -plane). This capability was achieved without using a bulky dielectric material over the aperture, making the proposed approach more attractive, especially at lower microwave frequencies and for mobile applications (e.g. UAVs).

Chapter 4 Fabricated Prototype and Measured Results

In this chapter, we present measured results for the wideband array with FSS introduced in Chapter 3, experimentally validating the large scan range and impedance bandwidth. The fabrication process of the prototype is discussed in Section 4.1. Then the measurement setup and the array performance are presented in Section 4.2. It is shown that the 12×12 prototype array is operational across $\sim 6.5:1$ bandwidth for broadside radiation. The prototype can scan $\pm 50^\circ$ for most of the bandwidth. The scan angle goes up to 70° at the higher end of the frequency band, where the aperture size becomes large enough to approximate the infinite array performance [62].

4.1 Fabrication of the Prototype

As mentioned in previous chapter, the array elements are designed using RT/duroid[®] 5880 ($\epsilon_r = 2.2$) with 3-layer copper. Two dielectric layers between the conductors are 20mil each. Together with the bonding material (4mil), total thickness of the printed circuit boards (PCBs) is 44mil. All 12 elements along E -plane are fabricated on the same PCB. Since the prototype is 12×12 , we fabricated 12 pieces of PCBs (each 48cm-long). These boards are placed vertically on a ground plane to form the full array. Below, we

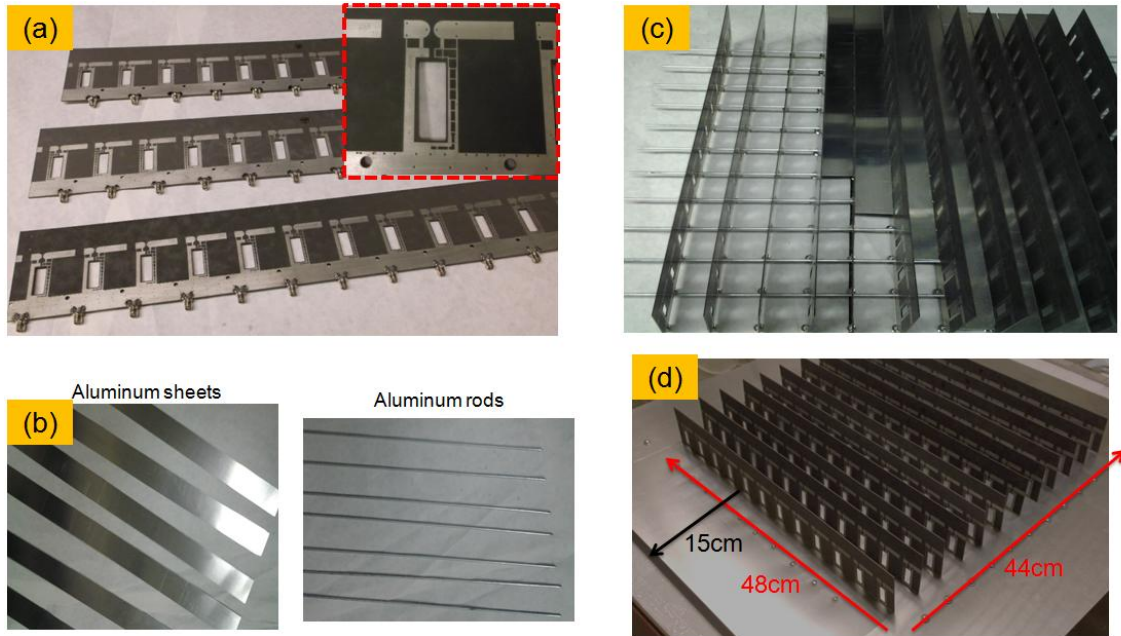


Figure 4.1: The fabrication steps of the 12x12 prototype.

summarize the fabrication/assembly process of the prototype array:

a. PCB board fabrication: 12 pieces of PCB boards including FSS, dipole, balun, tapered lines are fabricated. 50Ω edge-mount SMA connectors are also placed at the edges of the PCBs for connection to standard coaxial cables (see Figure 4.1a).

b. Aluminum rods and sheets: 60cm long aluminum rods and 4cm x 60cm aluminum sheets are prepared to align the PCBs and form a ground plane (see Figure 4.1b).

c. Assembly of the PCBs, Rods and Sheets: The aluminum rods are placed through the holes in the PCBs for accurate alignment and stabilization of the boards. The aluminum sheets are placed between neighboring PCBs and on the metal frame formed by aluminum rods such that they form the ground plane for the array (Figure 4.1c).

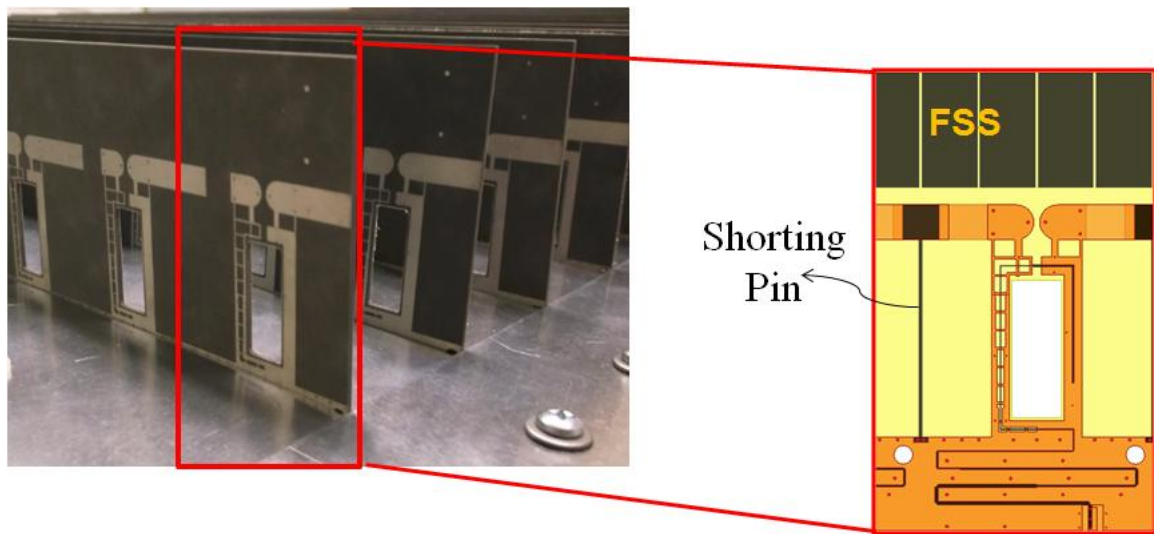
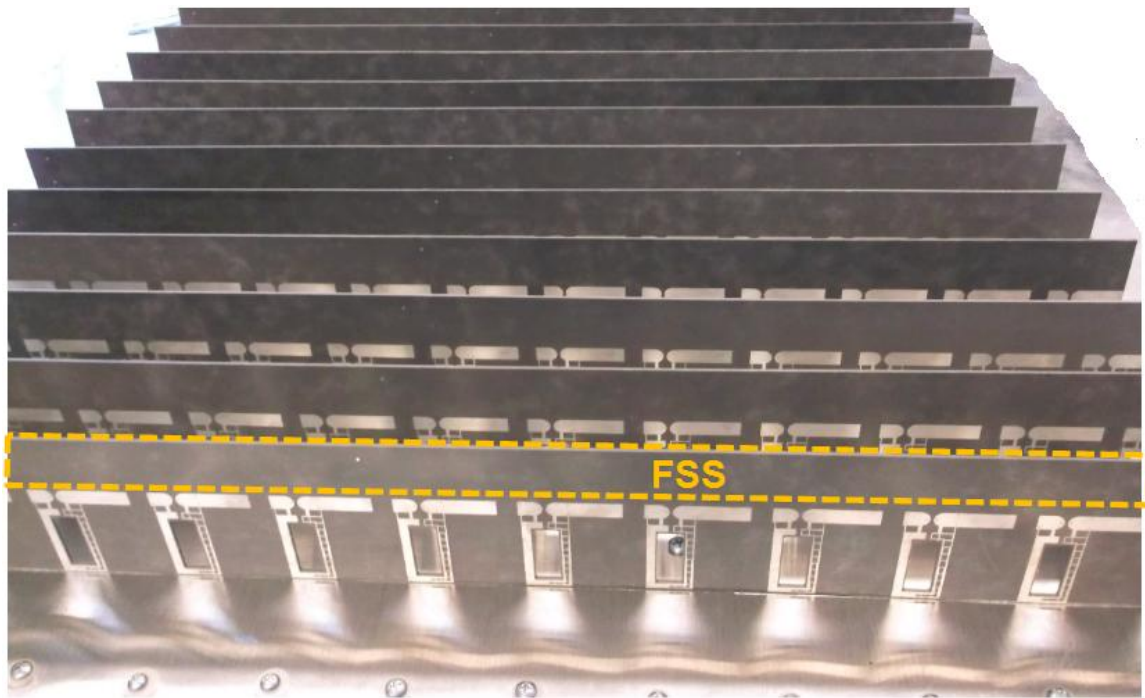


Figure 4.2: Final version of the 12x12 prototype array (top) and the unit-cell elements (bottom) are shown.

Copper tapes are also used to ensure electrical connection between aluminum sheets and outer conductors of the PCBs.

d. Ground plane extension around the aperture: After the metal frames between PCBs are fully covered with metal sheets, 15cm wide aluminum plates are used as ground plane extensions to reduce back-lobe and isolate back-end components (power divider, feed cables etc.) from the active array aperture.

4.2 Measurement of the Prototype

The Ohio State University anechoic chamber was used for pattern measurements (see Figure 4.3). The active part of the aperture was chosen to be 8x12 with the longer side aligning in the scanning plane (see Figure 4.4a & b). The measured realized gain at broadside is depicted in Figure 4.5. As can be seen, the simulated and measured data agree well for most of the bandwidth. At lower frequencies, the measured gain exceeds the active aperture area limit and reaches up to total area (12x12) directivity. This was expected since prototype antenna is electrically small at the lower end of the frequency band. Therefore, even if the edge elements are not excited, they still contribute to the array radiation due to coupling from active elements. The ground plane can also cause unintended radiation since it extends only a quarter wavelength (at 500MHz) away from the aperture and has no edge- treatment. The predicted normalized cross-polarization (X-pol) isolation was 34dB, but measured data was only 26dB. This was due to the feed antenna (*ETS Lindgren Dual Polarized Horn 3164-03* [63]) used during the measurements. The polarization purity of this horn antenna is reported to be 26dB, limiting the X-pol measurement. Nevertheless, the bottleneck for the X-pol performance

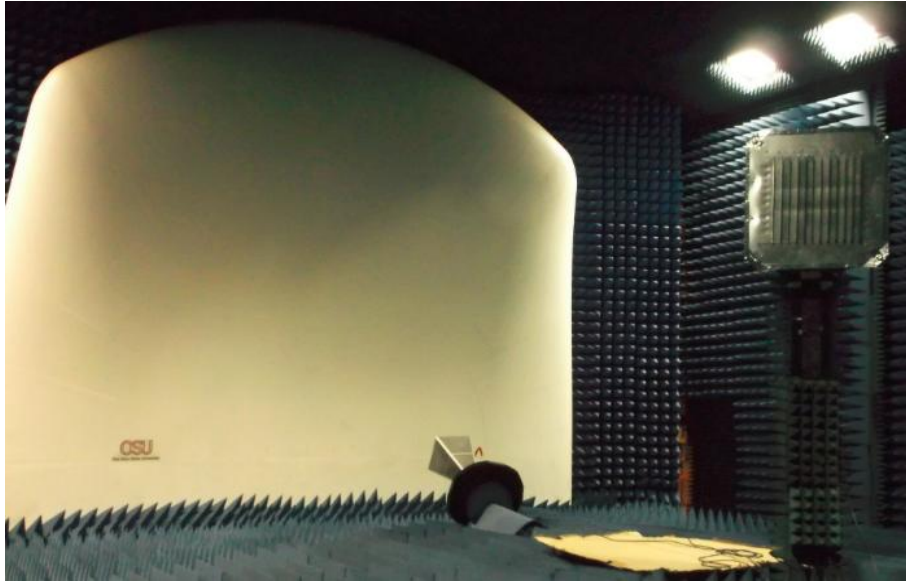


Figure 4.3: Far-field measurement setup in The Ohio State University anechoic chamber.

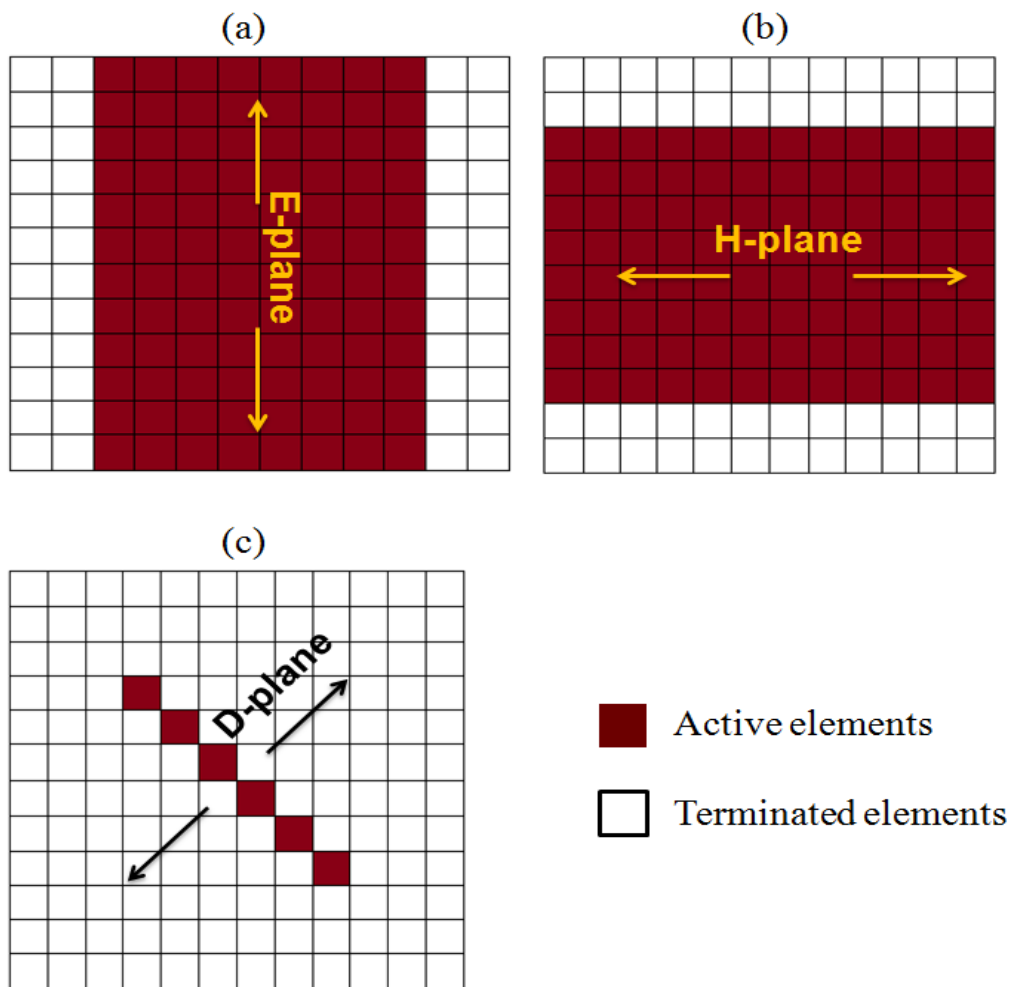


Figure 4.4: Active elements of the 12x12 prototype during E , H and D -plane measurements are shown with dark color. For D -pane, only one row is used to acquire active element pattern, instead of radiation pattern of the full array.

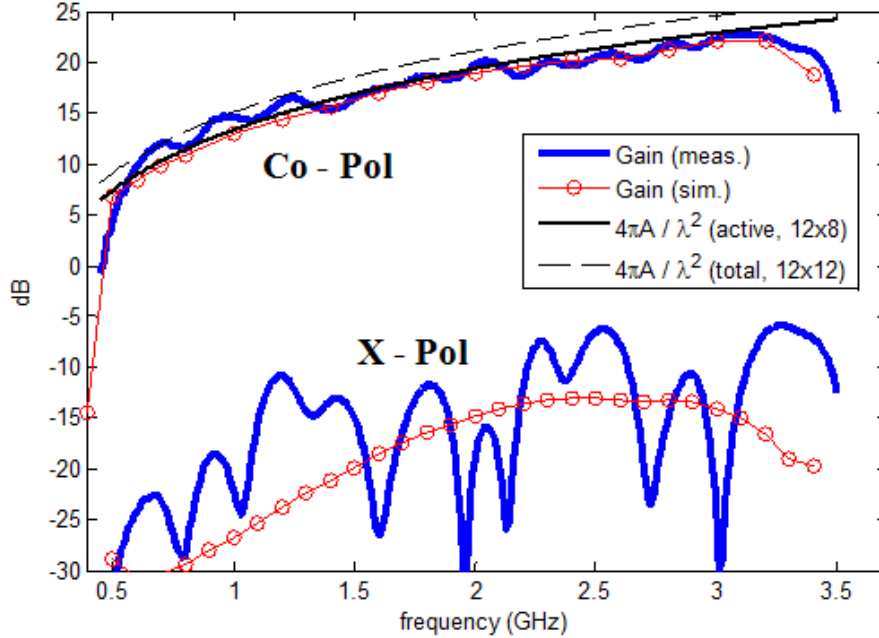


Figure 4.5: Broadside gain of the prototype. Measured values agree well with the simulations (generated from infinite array simulations) at high frequencies. At low frequencies, realized gain exceeds the active aperture limit.

is the D -plane. Our simulated values for the normalized X-pol radiation during D -plane scanning ($\theta \leq 60^\circ$) were approximately -10dB. This indicates that 26dB cross-polarization isolation for the feed antenna was sufficient.

The measured scanning patterns of the array in E and H -plane were obtained using unit-excitation active element pattern (UEAEP) method [67]. For this method, UEAEP of each radiating element should be measured and combined during post-processing. UEAEP of an element is the complex valued, $g(\theta, \phi)$, electric field pattern when only that element is excited and all other input ports of the array is terminated. Then, the fully excited array pattern can be obtained by vector summing UEAEP of each element as shown below;

$$\vec{E}_{total}(\theta, \phi) = \sum_{n=1}^N A_n \vec{g}_n(\theta, \phi) \quad (4.1)$$

where, \vec{E}_{total} represents the total electric field vector when all of the elements are activated for a specific scan angle. A_n is the required phase/amplitude coefficient for the elements and N is the total number of active elements.

As mentioned before, this method requires measuring each element's active pattern so that one can obtain the pattern of the fully excited array for any scan angle. However, when only specific scanning-planes are of interest (e.g. principal planes: E and H), then some of the elements can be measured together with a power divider, rather than separately. This is due to the fact that, some elements of uniform arrays have same excitation constant (A_n) with each other for all elevation angles in certain scanning planes. Therefore they can be excited together during the measurement process, rather than in post-processing.

For our 8x12 rectangular array, we consider E and H planes as the scan planes of interest. We note that an 8-element dipole row on a single PCB is basically a linear array with its elements aligned along an axis that is orthogonal to H -plane (see Figure 4.6). Therefore, during H -plane scanning, all radiators on this 8-element row will always have equal magnitude and phase, assuming uniform array excitation. In other words, their active element patterns do not have to be measured separately. Instead, they can be excited by an in-phase, equal amplitude power splitter and the measured pattern can be directly inserted into (4.1) as if it is a single element. This way, the measurement time required for a single scan-plane can be significantly reduced. For E -plane, a similar

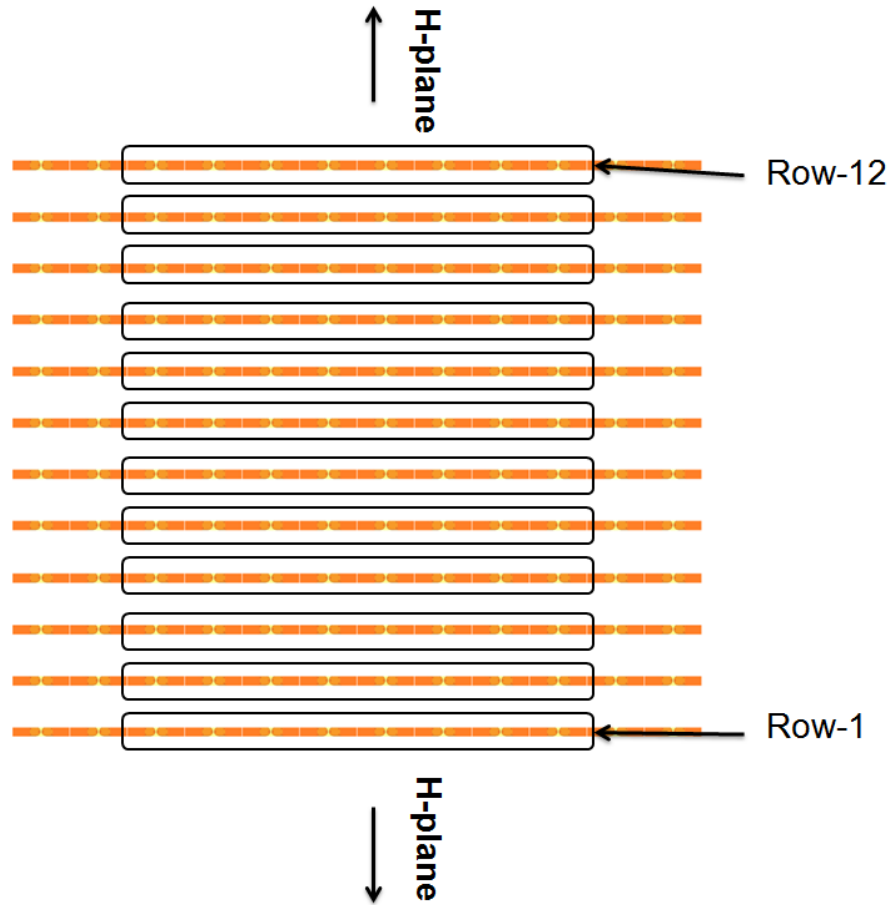


Figure 4.6: Schematic of 12x12 dipole array. Equal amplitude/phase element rows (1-to-12) for H -plane are shown with rectangles. Outer 2-elements on each row are terminated.

approach can be employed, but this time the equal amplitude/phase rows are the ones that are orthogonal to the E -plane (see Figure 4.7).

Based on the aforementioned analysis, the measurement process for E and H -planes are performed as following: Active part of the aperture was chosen to be 8×12 where longer side of the active array aligns in the scanning plane and the shorter side is in the orthogonal plane (as shown in Figure 4.6 and Figure 4.7). An 8-way power divider (Mini-

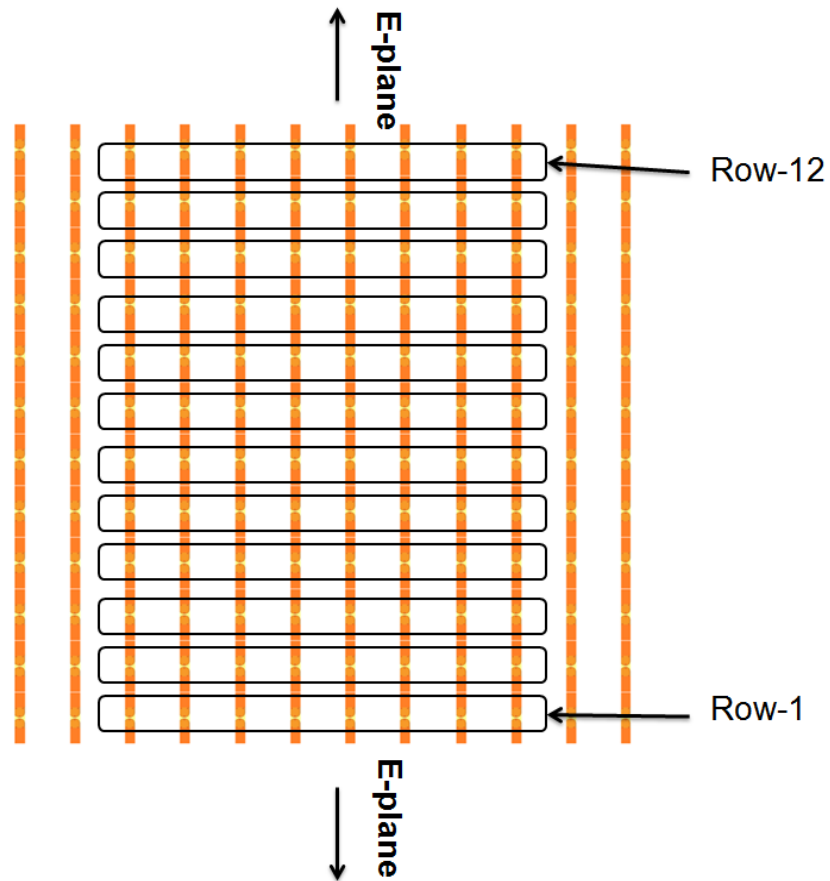


Figure 4.7: Schematic of 12x12 dipole array. Equal amplitude/phase element rows (1-to-12) for E -plane are shown with rectangles. Outer 2-elements on each row are terminated.

Circuits ZN8PD1-53+ [64]) was used to measure 8-elements at a time. Since the active array is formed by twelve of these 8-element rows, 12 measurements for each scanning plane (E and H) and polarization were performed. After the measured data were collected, field pattern of each 8-element row was inserted into (4.1) to calculate full array pattern. We note that feeding the array with a complete 1×144 power divider network was not considered due to the associated cost.

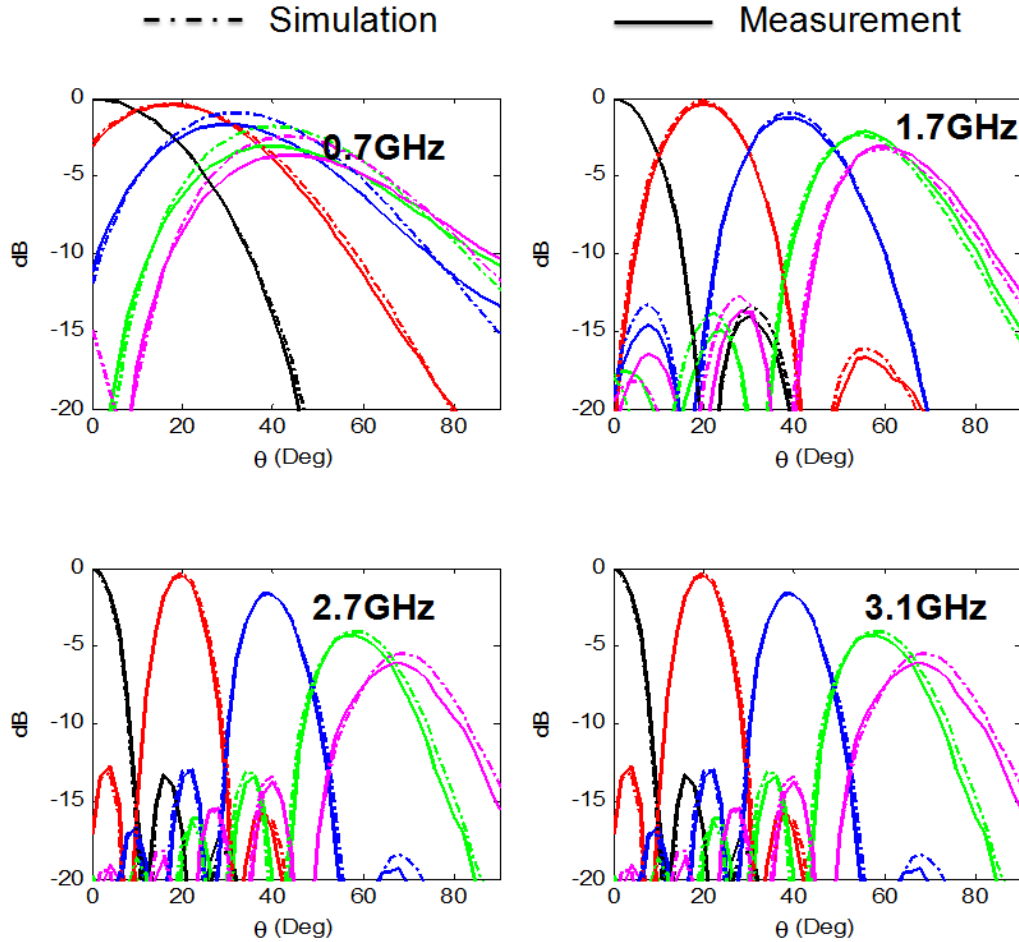


Figure 4.8: H -plane patterns at different frequencies, normalized to broadside level. Up to 70° scan angle is verified by good agreement with simulated patterns.

Measured and simulated H and E -plane patterns of the prototype are depicted in Figure 4.8 and Figure 4.9 respectively. At each frequency, the 2D patterns are normalized to the broadside gain. Beam-widths and gain levels of the measured and simulated patterns are in very good agreement. As expected, when the array aperture is electrically small, the antenna can only scan up to moderate angles. However, the prototype can scan up to 70° at higher frequencies. We observe that side-lobes are at -13dB for angles close

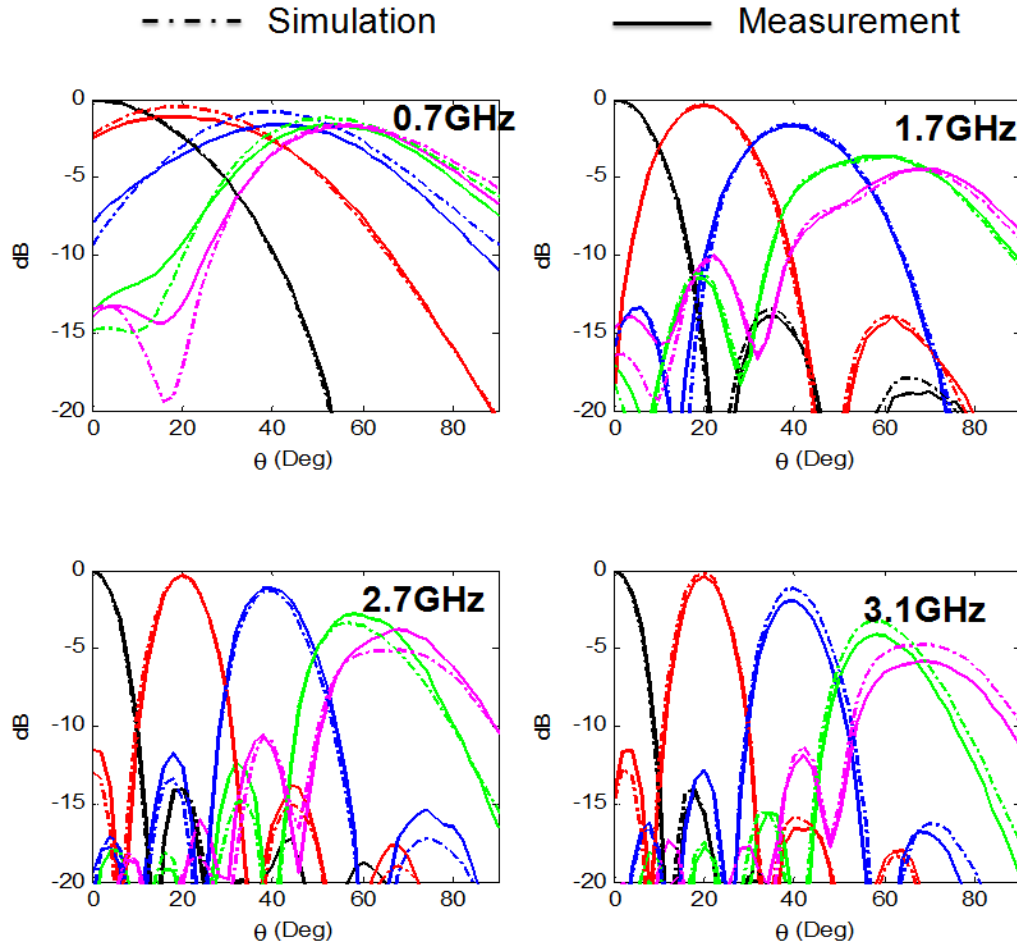


Figure 4.9: E -plane patterns at different frequencies, normalized to broadside level. Up to 70° scan angle is verified by good agreement with simulated patterns.

to broadside as expected for a uniformly excited aperture but increases for larger angles. We also note that the main beam broadens more than one might expect in the E -plane at 70° . We believe that these degradations are due to the surface waves being stronger at larger scan angles. These surface waves are not guided waves and only exist in finite arrays due to reflections from the aperture edges [73], [74], [75]. They can interfere with

the fundamental Floquet mode currents and cause standing wave-like distribution along the aperture, causing efficiency/pattern degradation. It is possible to mitigate them by terminating a few elements from the edges with appropriate resistors as proposed in [73]. But since our array was already very small at the lower end of the frequency band, we did not employ such edge termination.

Since we already verified the pattern and maximum scan angles for E and H -plane, we only measured one central row for D -plane scanning. The resulting pattern should be the same as active element pattern of a single unit-cell, along the diagonal plane. It is compared with the element pattern of a unit-cell in an infinite array (see Figure 4.10). Excellent agreement is observed for Co-pol gain values, verifying the infinite array simulations for D -plane scanning. However, measured X-pol is higher than predicted at lower end of the band, for large scan angles. In fact X-pol values approach Co-pol gain for $\theta > 60^\circ$ and $f < 2\text{GHz}$. We believe this is due to small ground plane which can be radiating itself at lower frequencies, causing X-pol radiation due to currents flowing along its edges. At higher frequencies, the measured X-pol levels align with the simulated values, since the excited fields along the array surface die out before they reach the end of the aperture and the ground plane. Measured data for the entire frequency bandwidth and scan area is provided in Figure 4.11.

4.3 Summary

In this chapter, a prototype of a TCDA with FSS superstrate was fabricated, tested and compared to the simulations. The fabrication procedure of a 12x12 prototype was described. Then the measurement setup/approach was discussed and the measured results

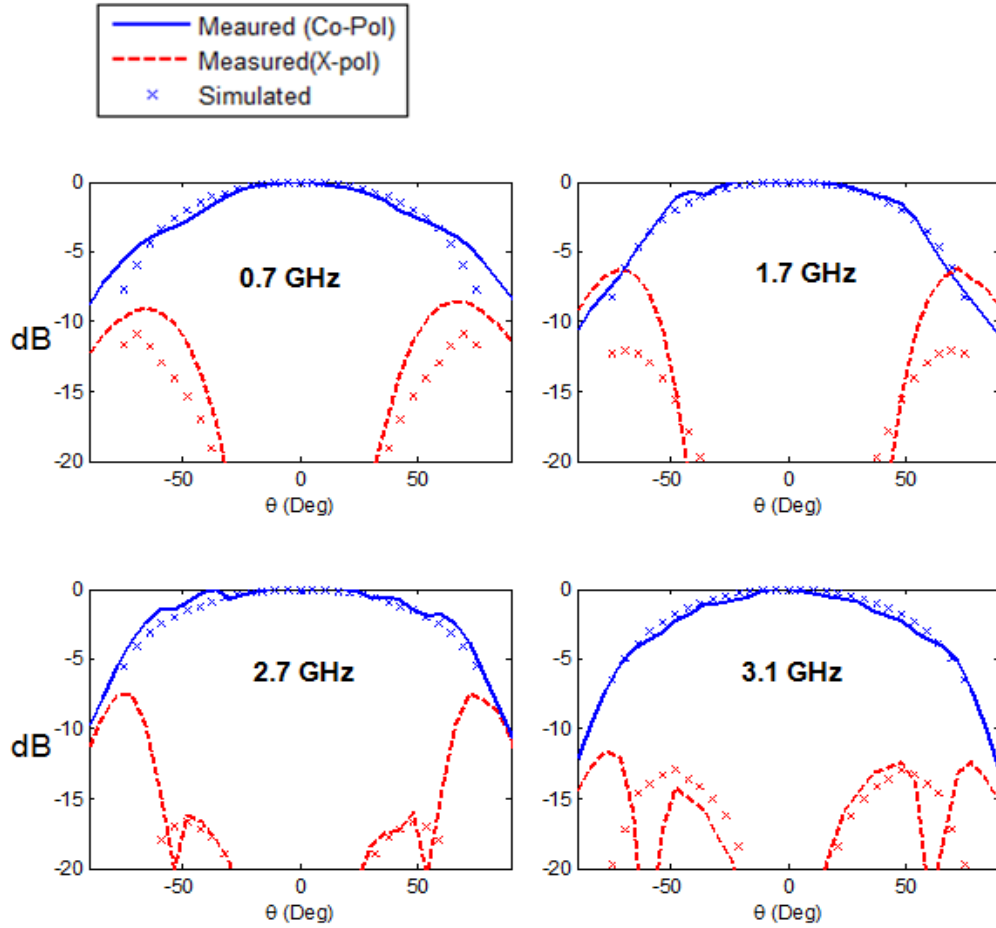


Figure 4.10: Simulated and measured 2D active element patterns along D -plane. These were obtained by measuring single 6-element row along diagonal of the aperture, as shown in Figure 4.4c

were presented. Excellent agreement between simulations and measurements were observed. The 3dB (compared to aperture directivity limit) gain bandwidth of the prototype was 6.9:1 for broadside radiation. Maximum scan angle was limited to about 50° due to electrically small size of the prototype at the lower end of the frequency band. At higher frequencies, the $\pm 70^\circ$ scanning capability was verified for the two principal planes and the diagonal plane.

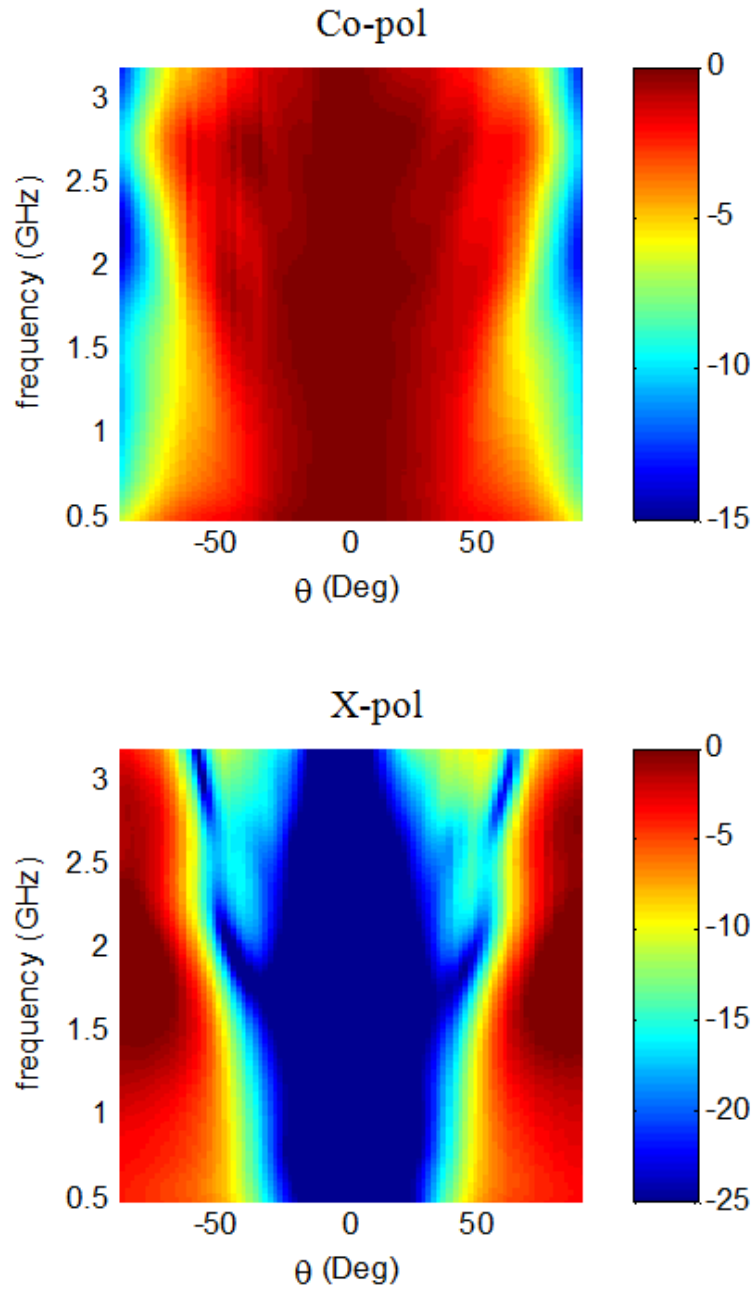


Figure 4.11: Measured element gain (normalized) and cross-pol radiation along the D -plane, for all scan angles across full frequency bandwidth (0.5-3.2 GHz). These were obtained by measuring single 6-element row along diagonal of the aperture, as shown in Figure 4.4c

Chapter 5 Dual-Polarized TCDA with Marchand Balun

In this chapter, we discuss the design of a dual-polarized TCDA using the balun introduced in Chapter 3. The focus will be on additional challenges in realizing the dual-polarized array and achieving performance similar to the single-pol geometry. As will be shown, the major challenge is the coupling between dual-polarized elements, especially at lower frequencies. This causes a low frequency loop resonance, similar to the one described in [41]-[42], limiting the frequency bandwidth from the lower end. We will show that using dielectric or FSS as superstrate over the active aperture does not make a significant difference in terms of overall bandwidth.

The chapter is organized as follows: First we will describe the geometry of the dual-pol array with integrated balun and a dielectric superstrate. Then, in Section 5.2, we will discuss the resonance problems due to coupling between orthogonally polarized dipoles. In Section 5.3, we will present the achievable bandwidth after considering the effect of these resonances. In Section 5.4, we will describe the procedure to design the impedance transformer for matching dipole input impedance down to 50Ω . In section 5.5, we will present a very similar dual-pol TCDA with FSS superstrate, achieving almost the same impedance bandwidth. Our conclusions will be given in Section 5.6.

5.1 Antenna Geometry with Dielectric Superstrate

The unit-cell of dual-polarized TCDA is shown in Figure 5.1. Unlike the FSS array in Chapter 3, the dipoles for both polarizations are placed on a PCB at the top of the baluns and on a plane parallel to the ground. The Marchand baluns are implemented in vertically oriented PCBs and make a connection to the dipoles in the top PCB from below. As superstrate, a low-contrast dielectric slab was used.

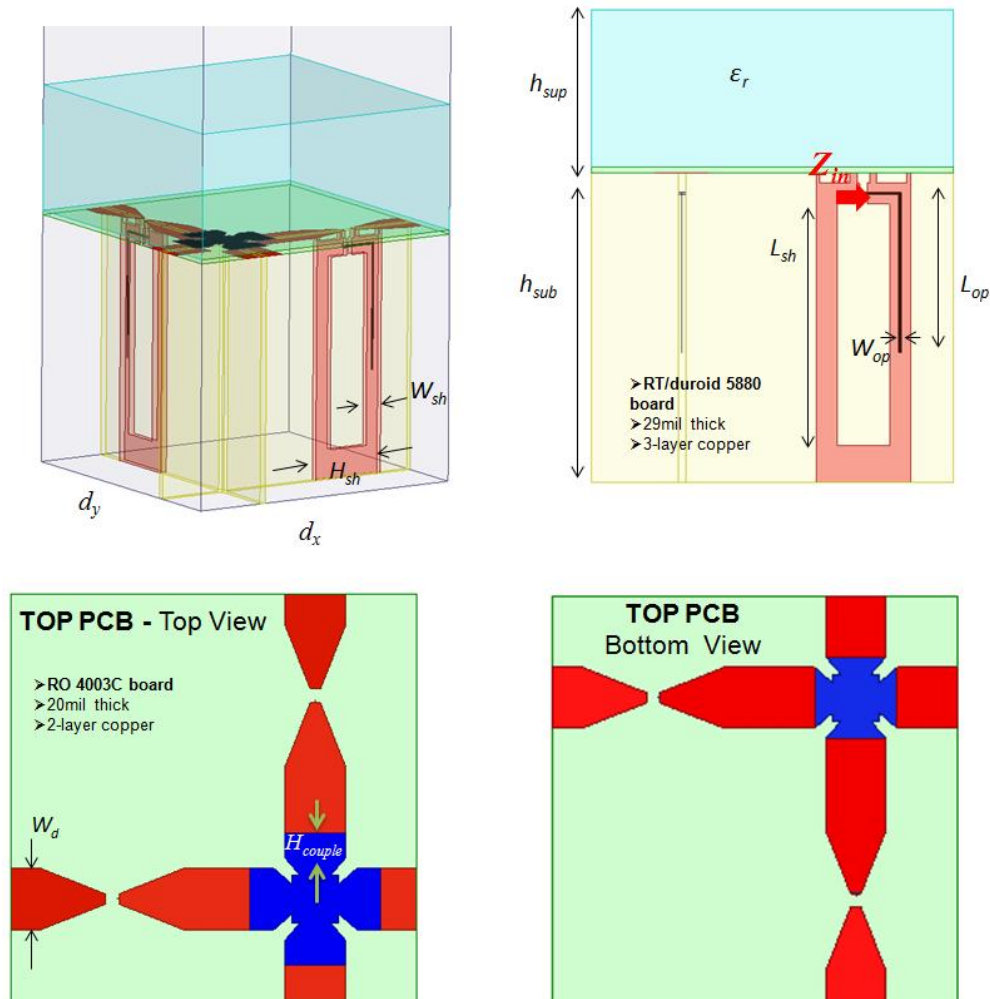


Figure 5.1: Unit-cell of dual-polarized TCDA with integrated Marchand balun.

The design parameters are the substrate and superstrate height (h_{sub} , h_{sup}), reactive loading due to the balun (W_{sh} , L_{sh} , H_{sh} , W_{op} , L_{op}) and the capacitive coupling (H_{couple}) between adjacent dipoles. Dipole width (W_d) was not considered for optimizations. Typically, wider dipoles provide better bandwidth but degrade polarization purity, especially when scanning. Therefore, we set W_d to $0.15d_x$ and tuned other parameters to improve impedance matching. We also note that the dielectric constant of the superstrate was fixed. Typically, a low-contrast ($\epsilon_r < 2$) material is needed to avoid surface waves when scanning wide angles. However, there are not many commercially available materials with this property. Therefore we chose “ECCOSTOCK[®]LoK” ($\epsilon_r < 1.7$), which has low loss and stable dielectric constant up to 10 GHz [65]. Although we will not present a fabricated prototype of the array, these choices ensure the array can be easily fabricated with commercially available components.

Both dipoles are excited by ideal gap sources with impedance, Z_{in} (see Figure 5.1). After a quick optimization, $\sim 5:1$ impedance bandwidth (BW) with 45° scan angle can be achieved, as shown in Figure 5.2. However, the reason for the bandwidth to be relatively low (compared to $6.5:1$ BW of the FSS-loaded TCDA in Chapter 3) is not due to using a dielectric superstrate (instead of an FSS). In fact, the main limiting factor is a low frequency resonance, which causes an anomaly in the impedance response of the array around 0.85 GHz. The anomaly is especially obvious for E and D -plane scanning. This is discussed in more detail in the next section.

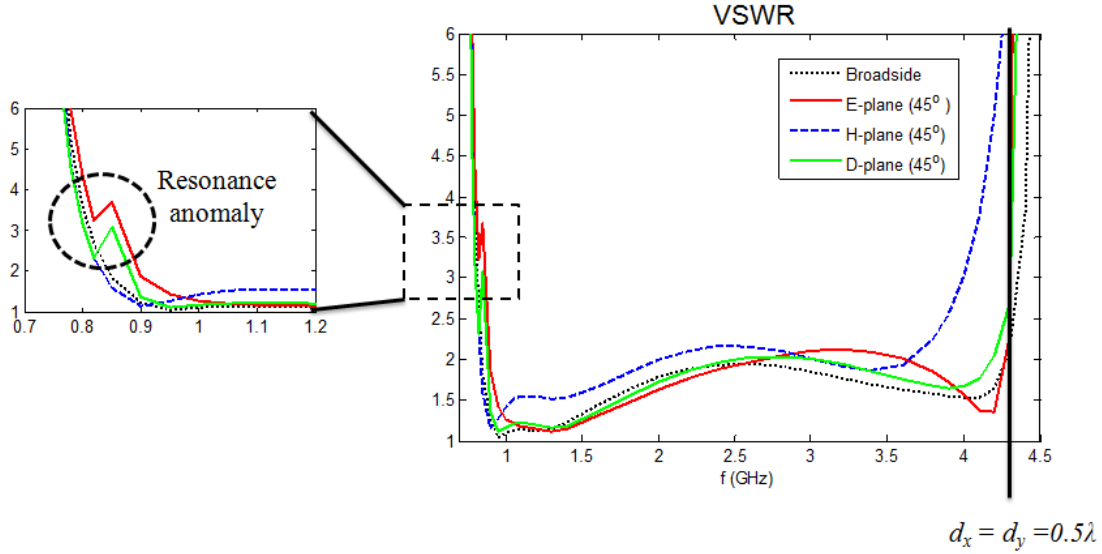


Figure 5.2: VSWR of the array in Figure 5.1, after a quick optimization. The impedance anomalies can be observed around 0.85GHz, limiting the impedance bandwidth.

5.2 Low Frequency Loop Resonance: Bandwidth Limitation

The magnitude of the electrical current on the conductors of the unit-cell is shown in Figure 5.3. The current distribution at the resonance frequency ($f_{res} = 0.804$ GHz) is compared to a non-resonant case (0.83GHz). As can be seen, at f_{res} , we observe high magnitude of current flowing through both active and terminated dipoles and baluns. For the non-resonant structure, the electrical current (much weaker as compared to the resonant case) is mostly confined to the active element. Therefore, we conclude that the reason for the impedance anomaly (see Figure 5.2) is coupling between cross-polarized elements.

The current vectors inside the unit-cell, at resonance, are shown in Figure 5.4. Marchand baluns that are intended to provide differential currents to the dipoles mostly

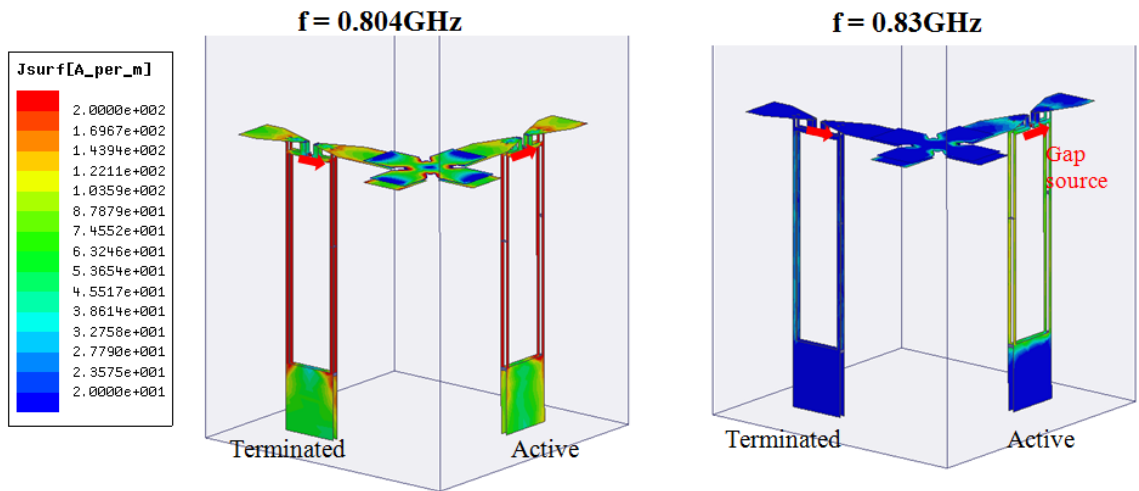


Figure 5.3: Current magnitude along the dipoles and baluns in the presence of the resonance (left) as compared to normal radiation in the absence of resonance (right).

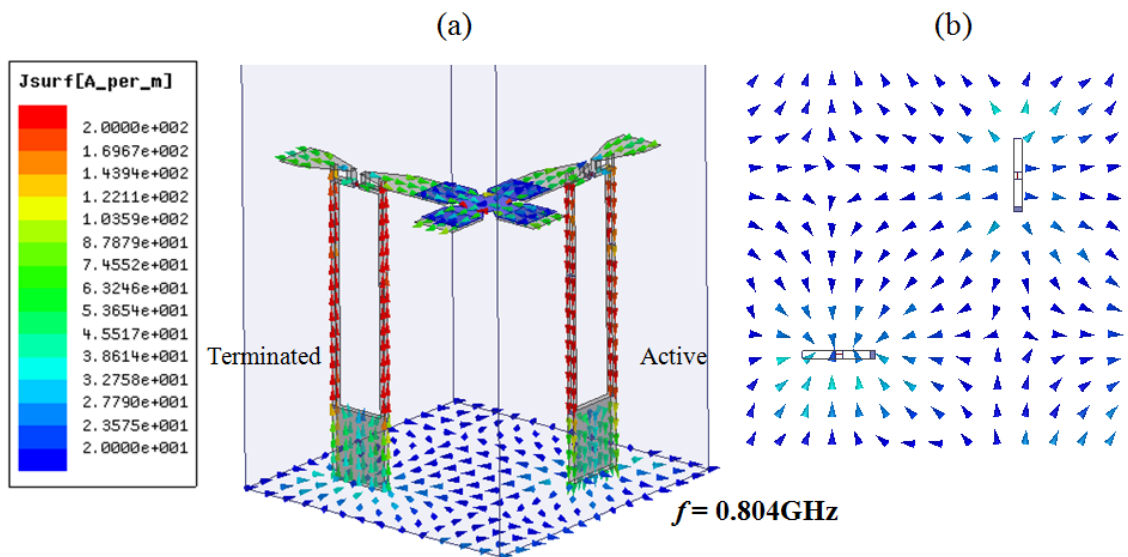


Figure 5.4: Current vectors inside the unit-cell in the presence of the resonance: (a) along dipoles and baluns, (b) on the ground plane.

carry common modes. We observe that the currents on the active and passive baluns are flowing in opposite directions (Figure 5.4-a), indicating the two orthogonally polarized dipoles with the baluns form a resonating loop. This is also supported by the current vectors on the ground plane (Figure 5.4-b), where the active – passive baluns seem like a source – sink pair.

To examine the parameters that affect f_{res} , we observed the change in port-to-port coupling (S_{12}) between orthogonal dipoles versus different geometrical parameters (H_{sh} , L_{sh} , h_{sub}) from Figure 5.1. Since the superstrate and the PCB substrates can modify the electrical length of the dipole and balun, we removed these dielectric materials during parametric simulations. The resulting S_{12} plots are provided in Figure 5.5. In this figure, $H_{couple}=4\text{mm}$, $L_{sh} = 2.5\text{cm}$, $h_{sub} = 3.5\text{cm}$, $H_{sh} = 0.7\text{cm}$ and $d_x = d_y = 3.45\text{cm}$, unless stated otherwise. As can be seen, decreasing the balun width (H_{sh}) and increasing the ground plane height (h_{sub}) lowers f_{res} . We also note that shorted stub length (L_{sh}) does not have a significant effect. This further verifies that the resonating currents flow on the dipoles and through the outer edges of the baluns to form a loop, rather than passing through the shorted stub. Although the coupling seems to be still acceptable at this resonance, the real problem is in the radiated fields. The cross-polarization purity (at 45° in the D -plane) goes down to 0dB at $f = f_{res}$ (see Figure 5.5d), since the effective radiating element is now a resonant loop formed by orthogonal dipoles rather than a single linear dipole.

A similar resonance was reported in [42] for the case of unbalanced feeding of the cross-pol dipoles with via pins. It is interesting to note that even a balanced feed (Marchand balun) cannot avoid this resonance. This indicates that the dominating factor

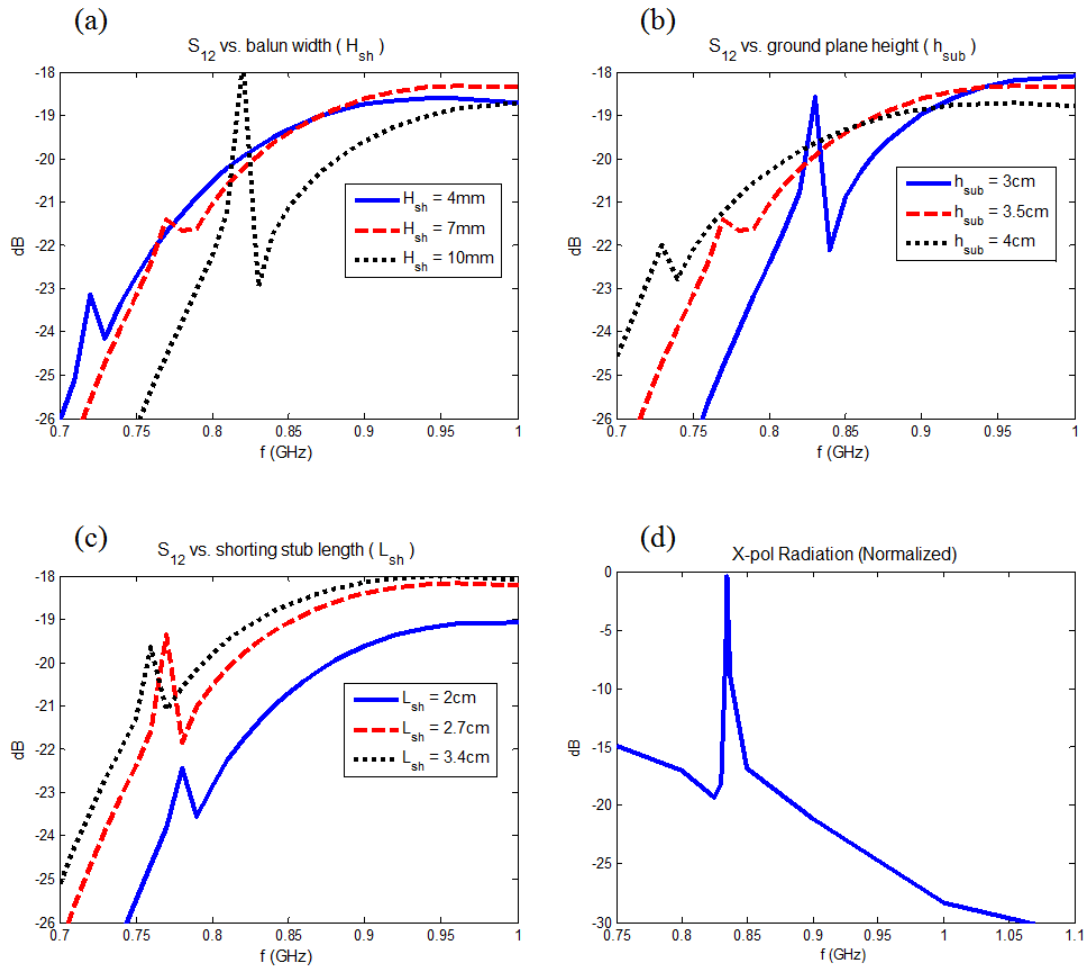


Figure 5.5: Variation of low frequency resonance, as indicated by S_{12} , versus a) balun width, b) ground plane height and c) shorted stub length is shown by S_{12} plots. Cross-polarized radiation for a typical case is shown in d). The array is excited to scan to 45° in diagonal plane.

in causing excitation of this type of common mode is the geometry and size of the whole unit-cell rather than the quality of the differential feeding elements. Similar to [42], we can estimate the resonance frequency (f_{res}) as follows;

$$f_{res} = \frac{c}{2\sqrt{\varepsilon_{eff}}(2d_x + 4h_{sub} - H_{sh})} \quad (5.1)$$

Here, ε_{eff} represents the effective dielectric constant for the resonant path, which is unity for Figure 5.5 since there is no dielectric material loading. We also assumed a square unit-cell ($d_x = d_y$). The estimated value of f_{res} and its actual value obtained from full-wave simulations are listed in Table 5.1 for different parameters. The estimation error is less than 7% for all the six cases considered.

Table 5.1: Comparison of estimated and actual resonance frequency for different geometrical parameters. d_x and d_y is assumed to be 3.45cm for all cases.

H_{sh}	L_{sh}	h_{sub}	f_{res} (estimated)	f_{res} (actual)
0.4cm	2.5cm	3.5cm	0.73 GHz	0.72 GHz
0.7cm	2.5cm	3.5cm	0.74 GHz	0.77 GHz
1.0cm	2.5cm	3.5cm	0.75 GHz	0.82 GHz
0.7cm	2.5cm	3.0cm	0.82 GHz	0.83 GHz
0.7cm	2.5cm	4.0cm	0.68 GHz	0.73 GHz
0.7cm	3.4cm	3.5cm	0.74 GHz	0.76 GHz

Although (5.1) gives good estimation of f_{res} , it does not include any dependence on the capacitive coupling (depends on H_{couple}) between dipoles. But we note that if H_{couple} gets smaller, f_{res} will go up and vice versa. To demonstrate this, we simulated two cases where H_{couple} is 2mm and 4mm. The resulting S_{12} plots are given in Figure 5.6, after normalization with S_{11} . As can be seen, decreasing capacitance moves the resonance frequency from 0.81GHz to 0.96GHz. Therefore, (5.1) should include an additional term to account for the capacitive coupling to provide more accurate estimations of f_{res} , as suggested by [42]. However, the predicted values are still good as an initial estimation and therefore no further effort will be spent on modification of (5.1).

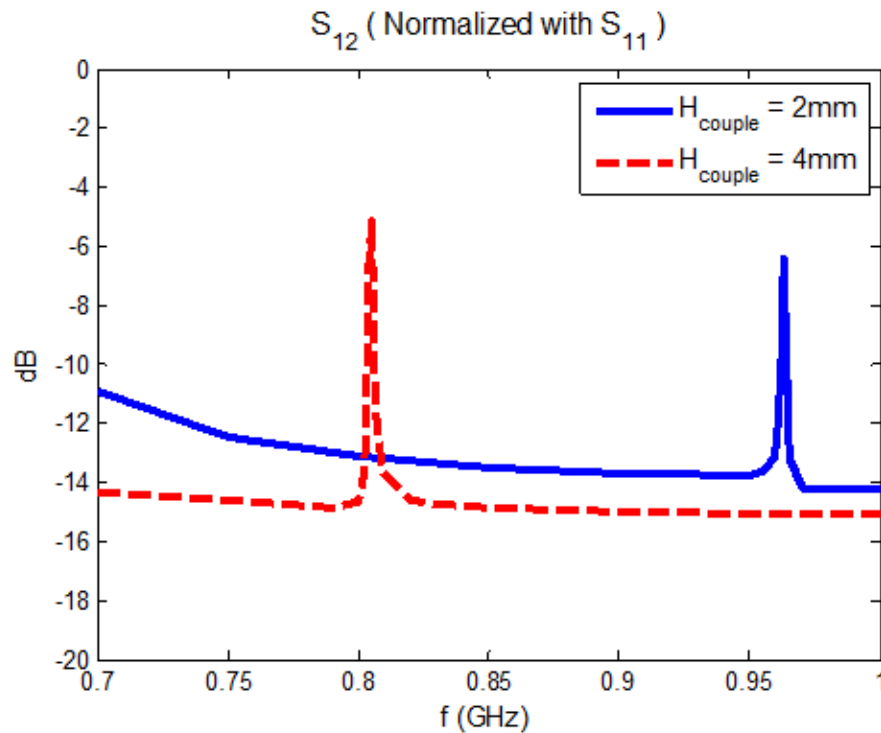


Figure 5.6: Variation of resonance frequency with coupling between dipoles.

5.3 Optimized Array with Limited Bandwidth

From the results presented in the previous section, we can estimate the available impedance bandwidth for the dual-pol array of Figure 5.1. The upper limit can be selected as the frequency where the unit-cell size is 0.5λ . Assuming $d_x = d_y = 3.45\text{cm}$ as before, this indicates $f_{high} = 4.35\text{GHz}$. At this frequency, the ground plane height (h_{sub}) should be less than 0.5λ (e.g. $0.45\lambda_{high}$ or 3.1cm). If we choose the balun width (H_{sh}) as 0.7cm ; then, from (5.1), the low frequency limit becomes $\sim 0.8\text{GHz}$. As a result, the available impedance bandwidth is $\sim 5.4:1$. Therefore, the focus of this section will be on achieving as much of this available bandwidth as possible, while scanning at least $\pm 60^\circ$ in all planes.

The simplified circuit model of the unit-cell for a single polarization is depicted in Figure 5.7. By using this simple representation of each polarization and full-wave simulations together, the input impedance (Z_{in}) is matched to 200Ω . The simulated VSWR values for different scan angles are depicted in Figure 5.8. The array can scan $\pm 60^\circ$ in H -plane, $\pm 70^\circ$ in E and D -plane. The impedance bandwidth is $4.4:1$ for $\text{VSWR} < 3$. The available bandwidth is not fully achieved due to the detuning of the array during scanning at higher end of the bandwidth. Specifically, the array starts to detune after $f > 4\text{GHz}$, rather than efficiently radiating up to the grating lobe frequency, 4.35GHz (where $d_x = d_y = 0.5\lambda$). This is due to wide scan angles causing the higher order modes to be excited strongly when the unit-cell size becomes electrically larger. However, the square unit-cell side length is $\sim 0.46\lambda_{high}$ and therefore the array can still be used for practical applications.

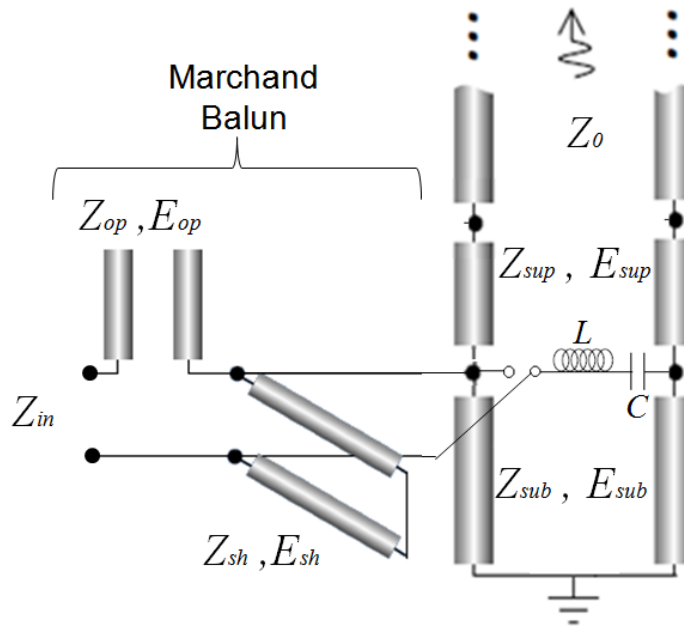


Figure 5.7: Approximate circuit model of the array in Figure 5.1. Marchand balun is modeled as a 2-stage transmission line with short and open stubs

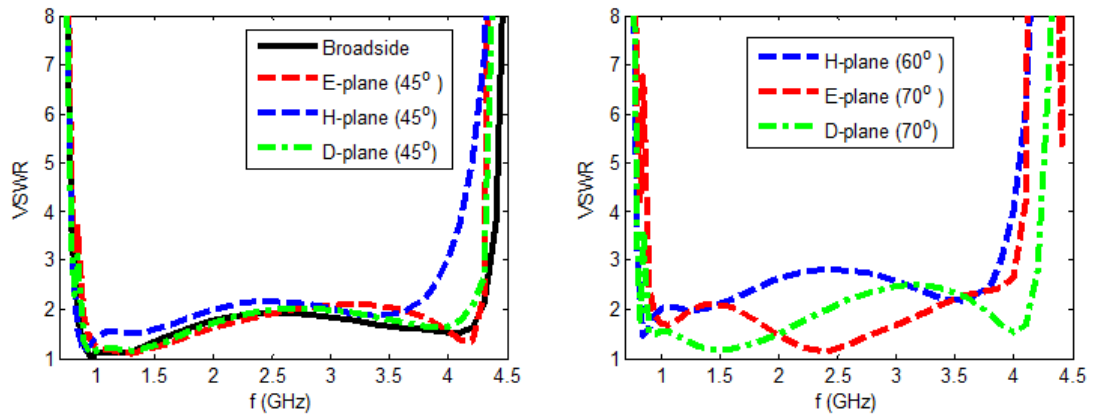


Figure 5.8: VSWR values for the optimized infinite array in Figure 5.1, for $Z_{in}=200\Omega$. Unit-cell dimensions; $d_x = d_y = 0.5\lambda$ at $f = 4.35\text{GHz}$

5.4 Design of Matching Network: Stepped Impedance Transformer

After optimizing the array with an ideal gap source excitation, we designed an impedance transformer to match the 200Ω input impedance of the balun down to 50Ω . To do this, we employed a 5-stage transmission line matching network. Note that, this is a much simpler transformer compared to the one used in Chapter 3, which had 18-stages. This is because the required bandwidth was larger and therefore more control on the impedance profile of the transformer was required for the FSS-loaded array.

To design the impedance transformer, S-parameters of the unit-cell of the dual-pol array were imported from *HFSS* into a circuit simulator (*ADS* [66]). Then, five transmission line sections were connected between 50Ω sources and the inputs of the imported component (see Figure 5.9). An integrated genetic algorithm in *ADS* was used

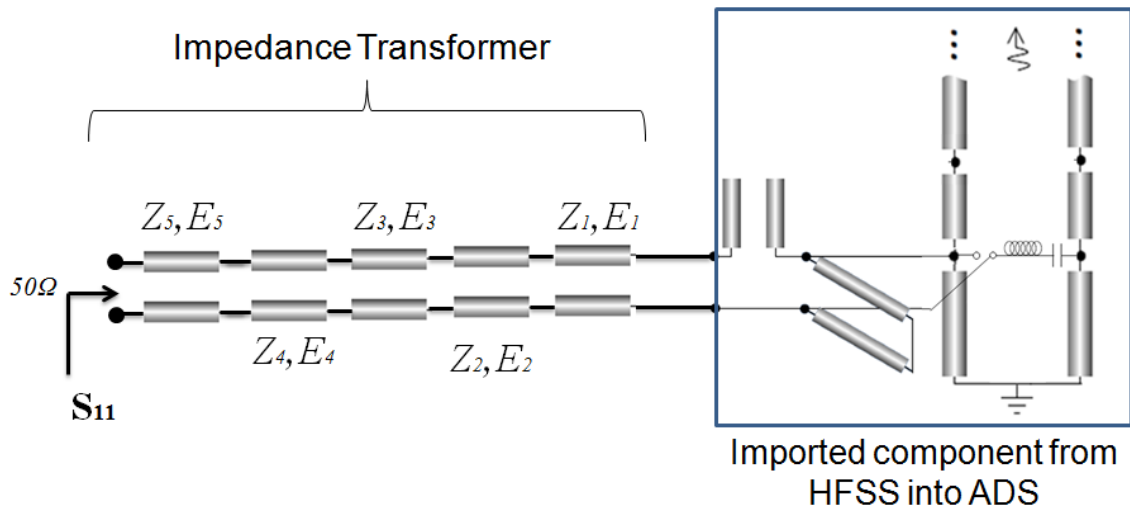


Figure 5.9: The circuit, optimized in *ADS* for minimum S_{11} . The optimization parameters are Z_i and E_i , which are characteristic impedance and electrical length of each transmission line section.

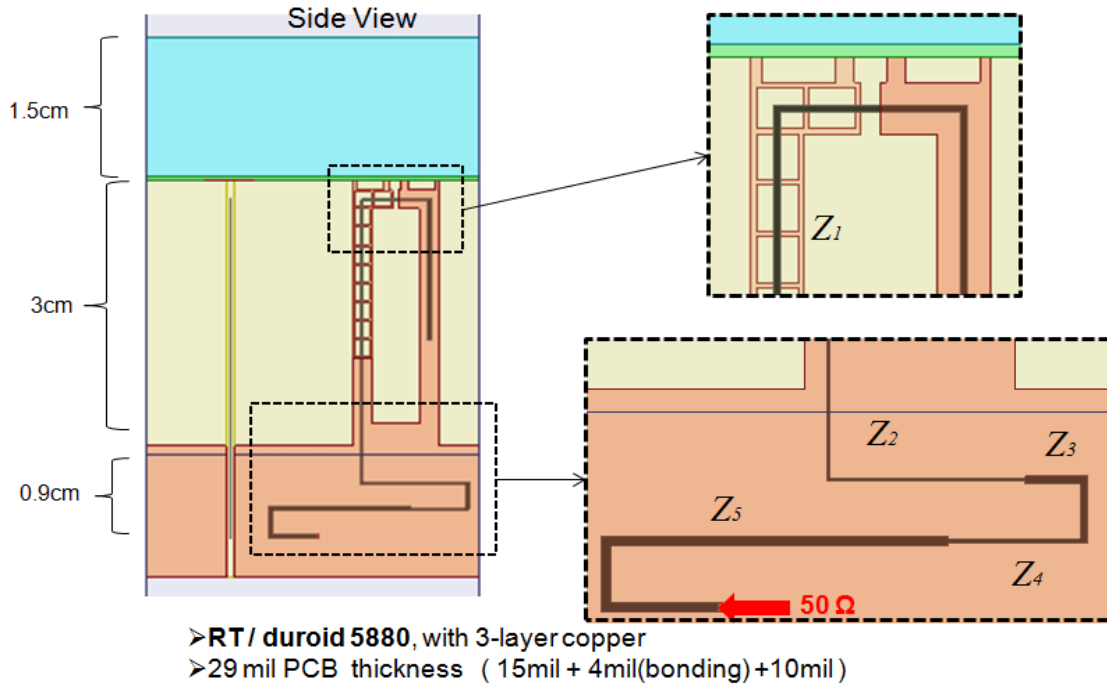


Figure 5.10: The final geometry of the dual-pol array with the balun and impedance transformer. Transformer parameters (Z_i , E_i) are obtained via optimizations in ADS

to maximize the return loss of the 50Ω sources. The optimization parameters were Z_i and E_i , characteristic impedance and electrical length of each transmission line section.

After the tuning process in ADS, the transformer was implemented in the full-wave simulator (see Figure 5.10). Similar to FSS-loaded array design, first transmission line section (Z_1 , E_1) was implemented with a perforated balun due to the required high characteristic impedance (Z_1), which is typically not practical for conventional stripline technology. The other four sections were implemented as regular strip-lines and meandered down the ground plane. The miniaturization of the array height is not in the scope of this work and as can be seen, the meandering of the transformer is not very tight.

However, one can further optimize the shape and implementation of the balun-transformer pair to minimize the extension (0.9cm) of the array below the ground plane.

Assuming a 50Ω source at the end of the transformer, the mismatch efficiency for different scan angles is plotted in Figure 5.11. As can be seen, the array can scan to 70° in E and D -planes and 60° in H -plane with less than 1.5dB mismatch loss. The overall impedance bandwidth is 4.5:1 (0.89-4GHz). As mentioned before, the lower frequency limit is determined by the loop resonance. The upper limit is due to the increasing electrical size of the unit-cell and getting close to grating lobe frequency.

In D -plane, the cross-polarized radiation and port-to-port coupling (S_{12}) between orthogonally polarized elements increase with scan angle. These are shown in Figure 5.12. There is a sharp increase in coupling and cross-polarization at the lower end of the band, due to the resonance. When, one of the dipoles is excited, a significant amount of current is coupling to the orthogonal dipole at f_{res} . This leads to a strong cross-pol radiation and leakage into the non-excited dipole input. Except for this region, S_{12} is less than -17dB and -10dB for 45° and 60° scanning in D -plane, respectively. The cross-pol radiation follows a similar pattern. It is around -20dB at 45° and -17dB at 60° scanning. These values are lower than the cross-pol radiation of the FSS-loaded array. There are two main reasons for this. One is that the number of vertically placed baluns on the ground plane is doubled as compared to a single-pol array. Therefore, the separation between the adjacent vertical feed-lines is cut by half, suppressing the common modes along these conductors and reducing the cross-pol radiation due to these undesired modes. This is the main reason why dual-pol TCDA's typically perform better than single-

pol versions in terms of cross-pol radiation. Second reason is that some portion of the undesired cross-pol field is absorbed by the orthogonally polarized elements (non-zero S_{12}), reducing the cross-polarized electromagnetic field strength in the far-field. However, this is not actually an improvement over single-pol arrays. It is merely a split of unwanted fields into two components; coupled power to the orthogonal port and cross-pol radiation.

The final design parameters of the optimized geometry are summarized in Table 5.2. It is obvious that the impedance transformer does not look like a tapered transmission line (TL). For optimum matching, it needs to have TL sections of changing length and characteristic impedance. The overall response is similar to a filter (rather than a monotonically tapered TL) to complement the response of the array/balun structure.

Table 5.2: Optimized values of the design parameters for the infinite, dual-polarized array in Figure 5.10

Parameter		Parameter		Parameter	
h_{sup}	15mm	L_{op}	15mm	Z_4	92 Ω
h_{sub}	30mm	W_{op}	0.25mm	Z_5	58 Ω
ϵ_r	1.7	W_d	5.1mm	E_1 (elec. len.)	38° (at 1GHz)
L_{sh}	23mm	H_{couple}	2mm	E_2	39°
W_{sh}	2mm	Z_1	140 Ω	E_3	9.4°
H_{sh}	9mm	Z_2	98 Ω	E_4	9.9°
d_x, d_y	35mm	Z_3	64 Ω	E_5	40°

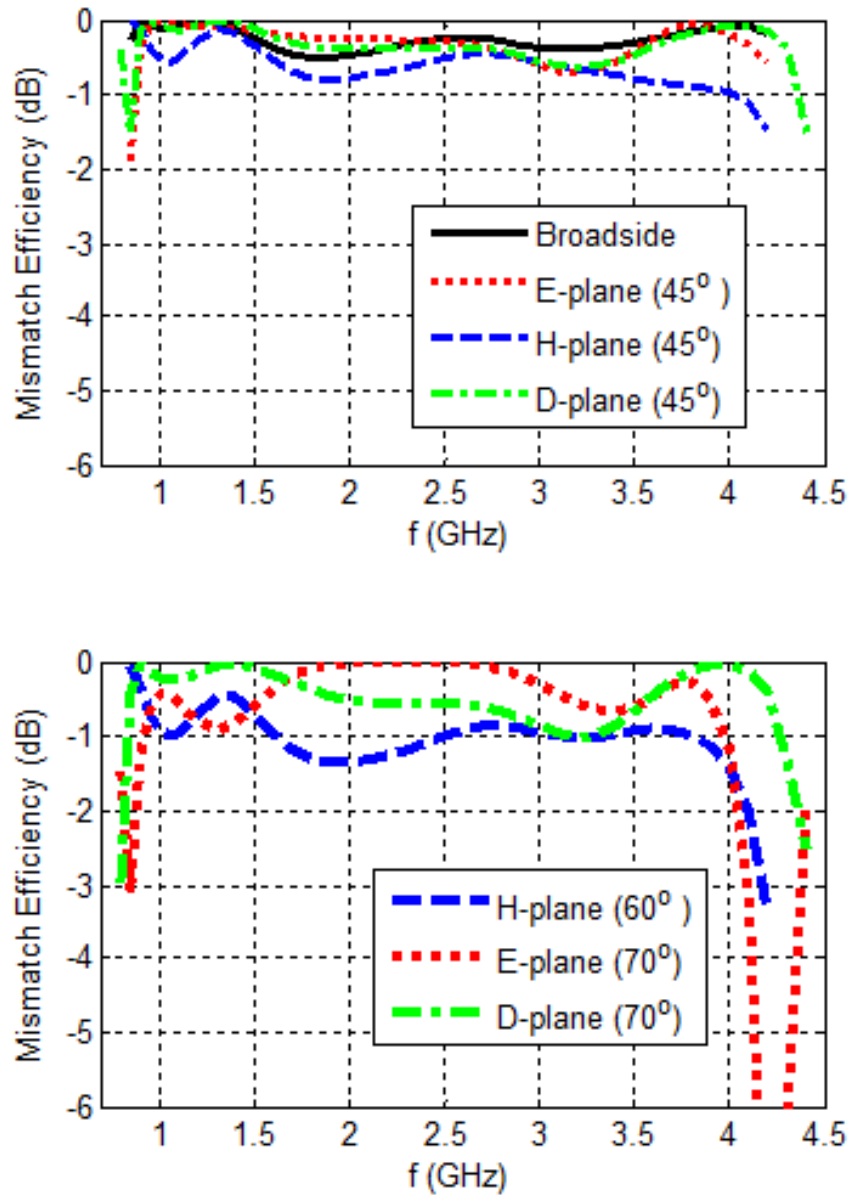


Figure 5.11: Mismatch efficiency of the dual-pol array with integrated balun and impedance transformer, for different scan angles.

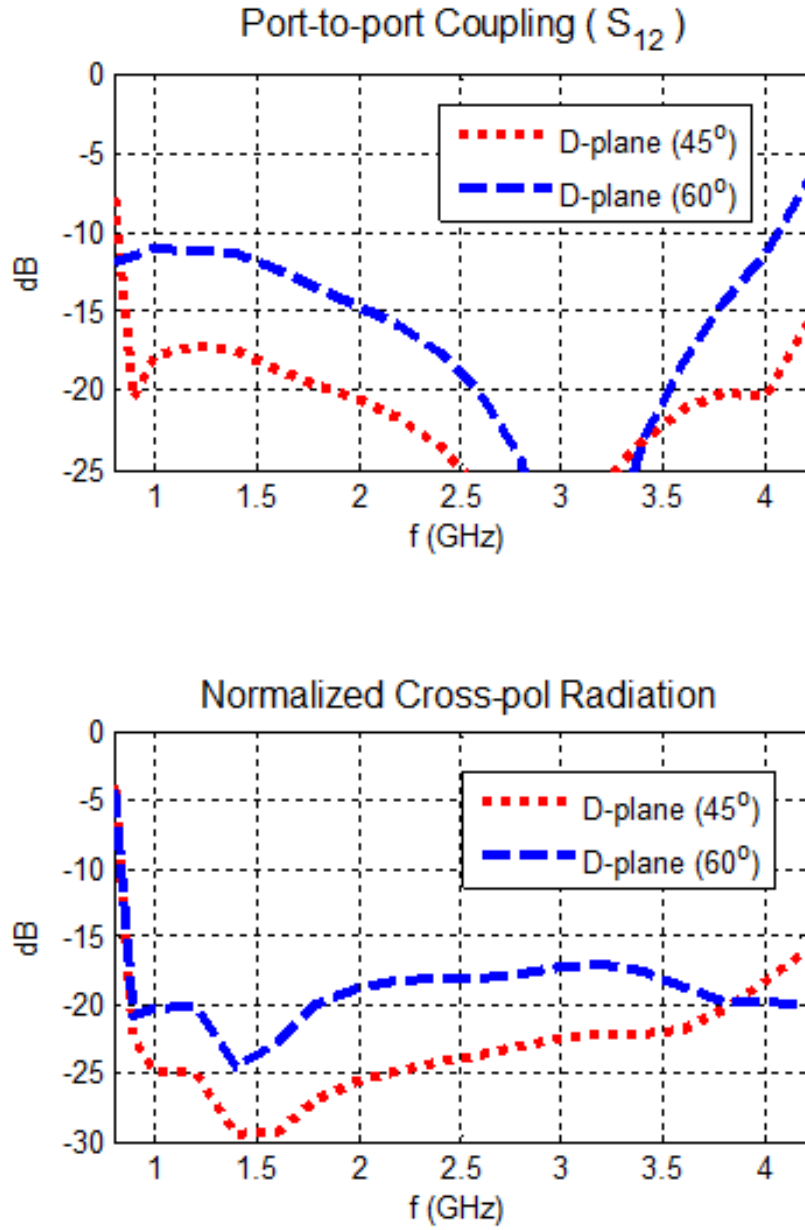


Figure 5.12: Coupling (top) between input ports of the orthogonally polarized dipoles and the cross-pol radiation (bottom) from each polarization, during *D*-plane scanning.

5.5 Dual-Polarized TCDA with FSS Superstrate

As we mentioned before, the main limitation in terms of impedance bandwidth for the dual-polarized TCDA comes from a low frequency resonance (see Figure 5.5). The available bandwidth is significantly lower than the potential of a TCDA with FSS or dielectric loading. In previous sections, we optimized the dual-pol array with dielectric superstrate and achieved $\sim 4.5:1$ bandwidth when $\theta_{max} \leq 60^\circ$ for H -plane and $\theta_{max} \leq 70^\circ$ for E and D -plane. To show that there will not be a significant difference (unless the feeding is modified) when the dielectric is replaced by any other well-designed printed superstrate, we simulated an infinite dual-pol TCDA with the same FSS introduced in Chapter 3.

The geometry of the antenna is depicted in Figure 5.13. The feeding is almost the same with the array in Figure 5.1. The difference is that the dipoles on the top PCB was moved onto the vertical PCBs and the dielectric slab ($\epsilon_r=1.7$) was replaced by the FSS. Instead of the impedance transformer, we used ideal gap sources (200Ω) at the balun inputs for the sake of simplicity. The PCB material, number of copper layers and board thickness are all the same with dielectric loaded dual-pol array.

The mismatch efficiency of the dual-pol TCDA with FSS is shown in Figure 5.13. As can be seen the impedance bandwidth (0.85-4 GHz) is about the same as before. The mismatch loss is below 0.8dB when maximum scan angle is 60° for H -plane and 70° for E and D -plane. The reason for better efficiency is exciting the array with ideal gap sources with perfect 200Ω impedance, rather than 5-stage transformer connected to a 50Ω source. The cross-pol radiation and port-to port coupling (S_{12}) values are depicted in

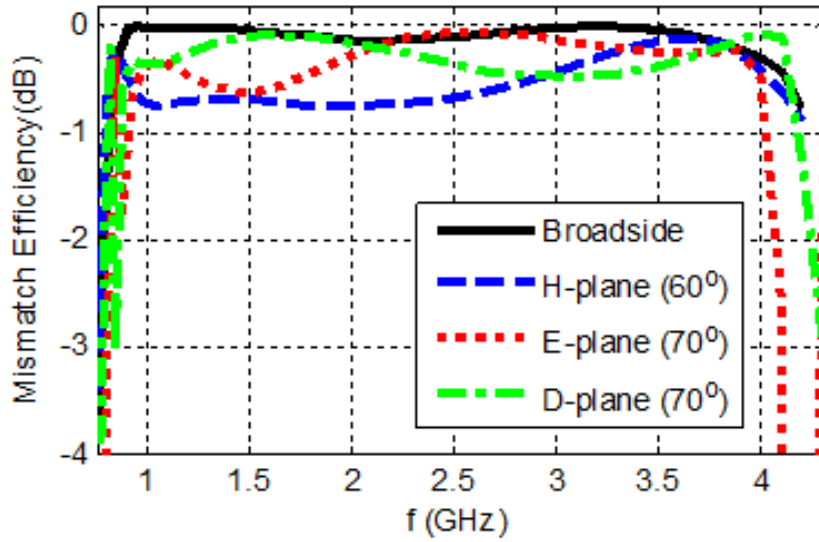
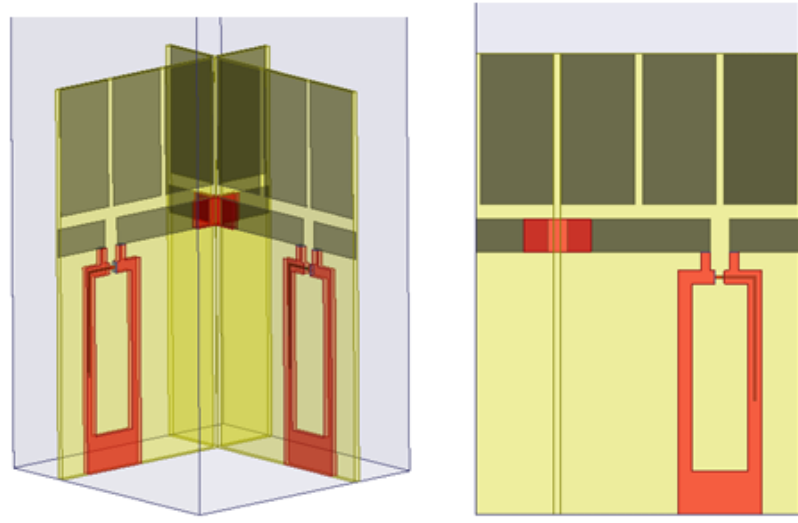


Figure 5.13: Dual-polarized TCDA (top) with FSS superstrate and the mismatch efficiency (bottom) for different scan planes. The unit-cell is excited by a 200Ω gap source. 3-layer PCB (RT/duroid 5880, 29mil thick) was used for implementation. Outer copper layers are shown with red color and middle layer is shown with black. The geometry is the same as Figure 5.1, except that the dipole elements on the top PCB are moved onto the vertical PCBs and the dielectric superstrate is replaced by FSS.

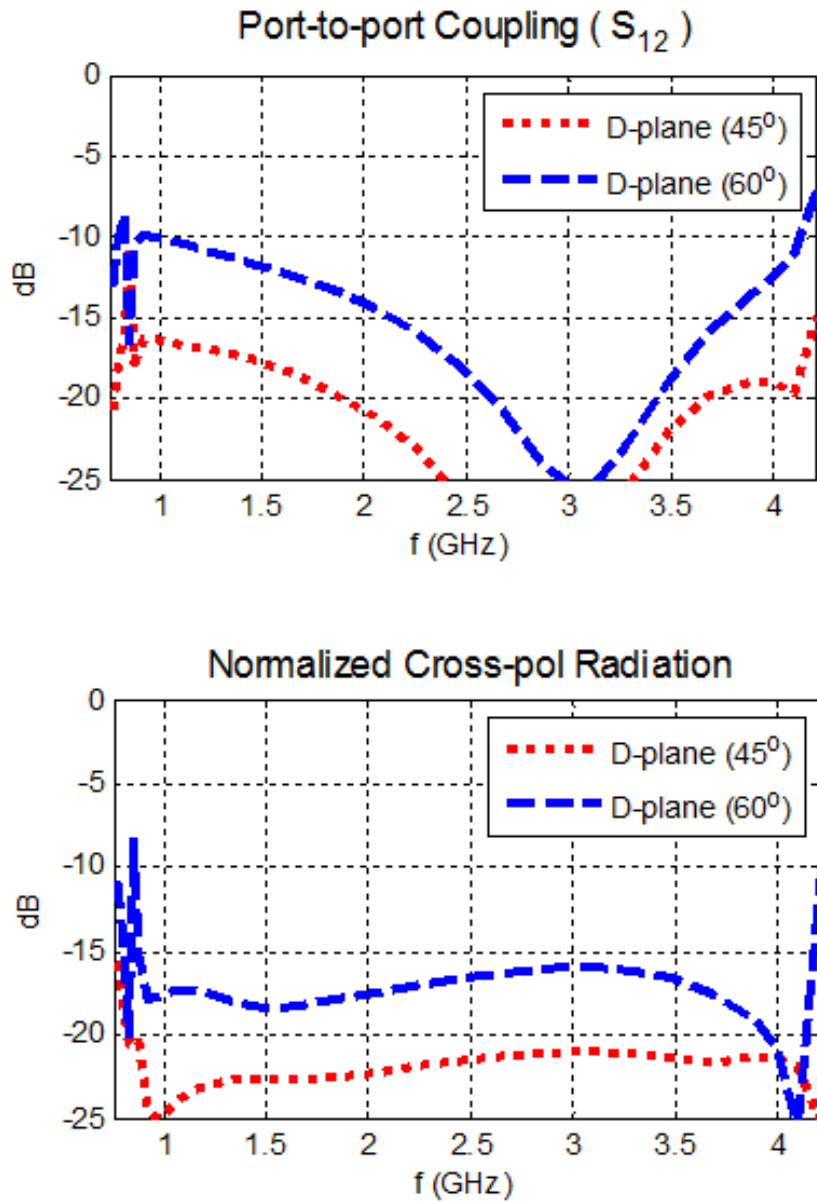


Figure 5.14: Port coupling and X-pol radiation for the infinite array in Figure 5.13.

Figure 5.14. As can be seen, they are about 1dB worse than the cross-pol and S_{12} of the dielectric loaded array. This is due to the vertical patches of the FSS-layer contributing to the X-pol radiation, as already mentioned in Chapter 3.

5.6 Summary

In this chapter, a dual-polarized TCDA using the perforated Marchand balun as wideband feed was presented. An impedance anomaly due to a low-frequency resonance, similar to the one described in [41], was identified. We note that this resonance occurs despite the balanced excitation of the array by the Marchand balun and leads to a smaller bandwidth compared to single-pol version of the same type of arrays. The overall bandwidth for broadside radiation when a dielectric superstrate is used is $\sim 5:1$. During scanning to $\pm 60^\circ$, the impedance bandwidth decreases to 4.5:1. The maximum scan angles are 60° for H -plane and 70° for E and D -plane (for $VSWR < 3$). We also showed that using an FSS superstrate instead of the dielectric results in almost the same impedance bandwidth, due to the low frequency resonance of the feed lines.

For improved bandwidth at the lower end, a feeding structure/balun with a smaller footprint (H_{sh}) might be used, as suggested by Figure 5.5a. Another option is to use dielectric loading in substrate layer of the array. This can increase the electrical length of resonant path and decrease the common mode frequency, resulting in wider available bandwidth. However, this would also result in a thick dielectric slab ($h_{sub} + h_{sup}$) backed by the ground plane, causing earlier onset of surface waves and limiting the scan range at the higher end of the frequency band.

Chapter 6 Scanning Performance of Finite TCDAs with FSS and Dielectric Superstrate

So far, we focused on infinite array designs. The measured prototype in Chapter 4 was simply fabricated by repeating the unit cell in a 12x12 form. However, practical scanning arrays with specific performance requirements (e.g. max. side lobe, pointing accuracy etc.) typically have resistively terminated edge elements around the active aperture area. This is done to mitigate the edge-born waves [39], [73] and improve the directional accuracy of the main beam. Moreover, these dummy elements may not be identical to other unit-cells. They can have different terminal resistances to suppress the edge-born waves more effectively [73]. We note that these waves only exist in finite arrays (also referred as surface waves in [73]) due to diffraction at the aperture edges and are different than more well-known surface waves [11] that can also be observed in infinite arrays.

In this part of the dissertation, we will consider realistic aperture sizes for TCDAs and study the effect of dielectric or FSS superstrate for these finite arrays. While doing so, we will consider a smaller bandwidth ($< 2:1$) where the unit-cell size is quarter wavelength or more. This is because, for very large bandwidths (e.g. 6:1), the unit-cell size of the array is very small ($< 0.1\lambda$) at the lower end of the band, resulting in an extremely dense

aperture. In this case, the finite array behavior of a connected array is mostly determined by the electrical size of the total aperture, regardless of the unit-cell design. This is not true for arrays with lattice size of $\sim 0.5\lambda$. A finite connected dipole array of $10\lambda \times 10\lambda$ can support strong edge-born waves along its entire aperture, assuming 0.5λ periodicity for the feeding points [76]. These waves cause fluctuations in the current amplitude along the array aperture, causing every unit-cell element to “see” different input impedance. As a result, the active reflection coefficient from each unit-cell is different, causing degradation in overall efficiency and radiation pattern. This problem is relatively small when the lattice size is less than 0.25λ for the same aperture size. Therefore, we will only study finite TCDAs with $> 0.25\lambda$ unit-cell size ($< 2:1$ bandwidth).

In Chapter 4, we showed radiation patterns for a 12×12 prototype. In these pattern plots, we observed that the scanning patterns were much worse for the E -plane as compared to the H -plane, for large scan angles. Therefore, the focus of this part of the dissertation will be on E -plane scanning of the finite arrays.

The chapter is organized as follows. We first show a modified version of the FSS integrated TCDA, presented in Chapter 3. This version of the array has slightly larger unit-cell and reduced bandwidth ($\sim 2:1$) but much superior mismatch efficiency. In Section 6.2, we describe the geometry for the finite array simulations. The results of full-wave simulations for FSS and dielectric loaded TCDAs are provided in Section 6.3. In Section 6.4, we propose a different FSS geometry with resistive terminations at the aperture edges, particularly useful to suppress diffractions and improve pointing accuracy. Our conclusions will be presented in Section 6.5.

6.1 FSS Integrated TCDA with Modified Feed

The unit-cell of the infinite antenna array is depicted in Figure 6.1. This is simply a TCDA using the same FSS from Section 3.2, but with different feed. Specifically, an unbalanced pair of coplanar striplines is used to feed the antenna, instead of a Marchand balun, similar to [40]. However, the shorted and open stubs are kept for impedance matching. The square unit-cell aperture is $0.45\lambda_h \times 0.45\lambda_h$ (at 2.5 GHz), chosen smaller than $0.5\lambda_h$ for better impedance matching across the large scan range of interest ($\pm 70^\circ$ from broadside). The PCB material is RO4725JXR ($\epsilon_r = 2.64$), with 3 copper layers. Minimum feature size is ~ 20 mil, (due to stripline), as shown in Figure 6.1. This indicates that, the design can be scaled up to ~ 15 GHz by replacing the PCB material with R/T duroid 5880 ($\epsilon_r = 2.2$) and minimal change in design parameters. By using perforations along the outer conductors of the stripline, the array can easily be scaled up to cover the entire Ku band (12-18GHz).

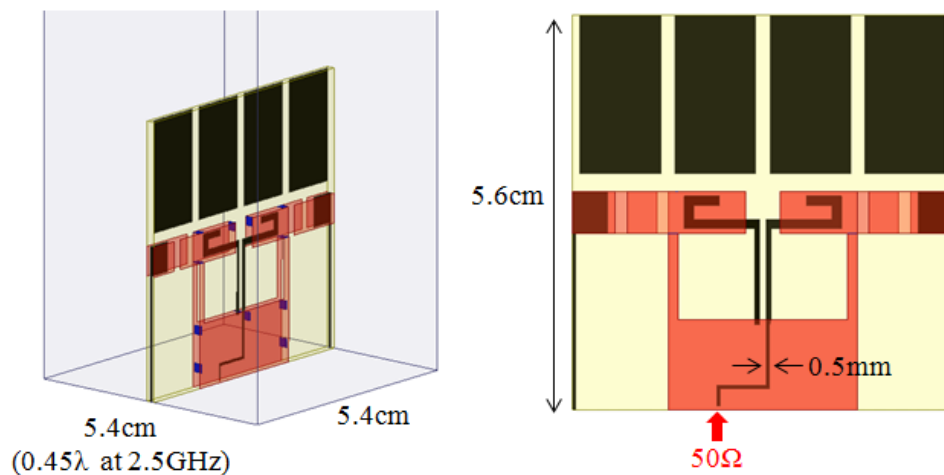


Figure 6.1: Geometry and the modified TCDA with FSS. Marchand balun was removed from the design in Chapter 3. Instead, an unbalanced pair of coplanar striplines was used to feed the dipole, similar to [40]. 3-layer of copper was used on a 68mil PCB ($\epsilon_r = 2.64$)

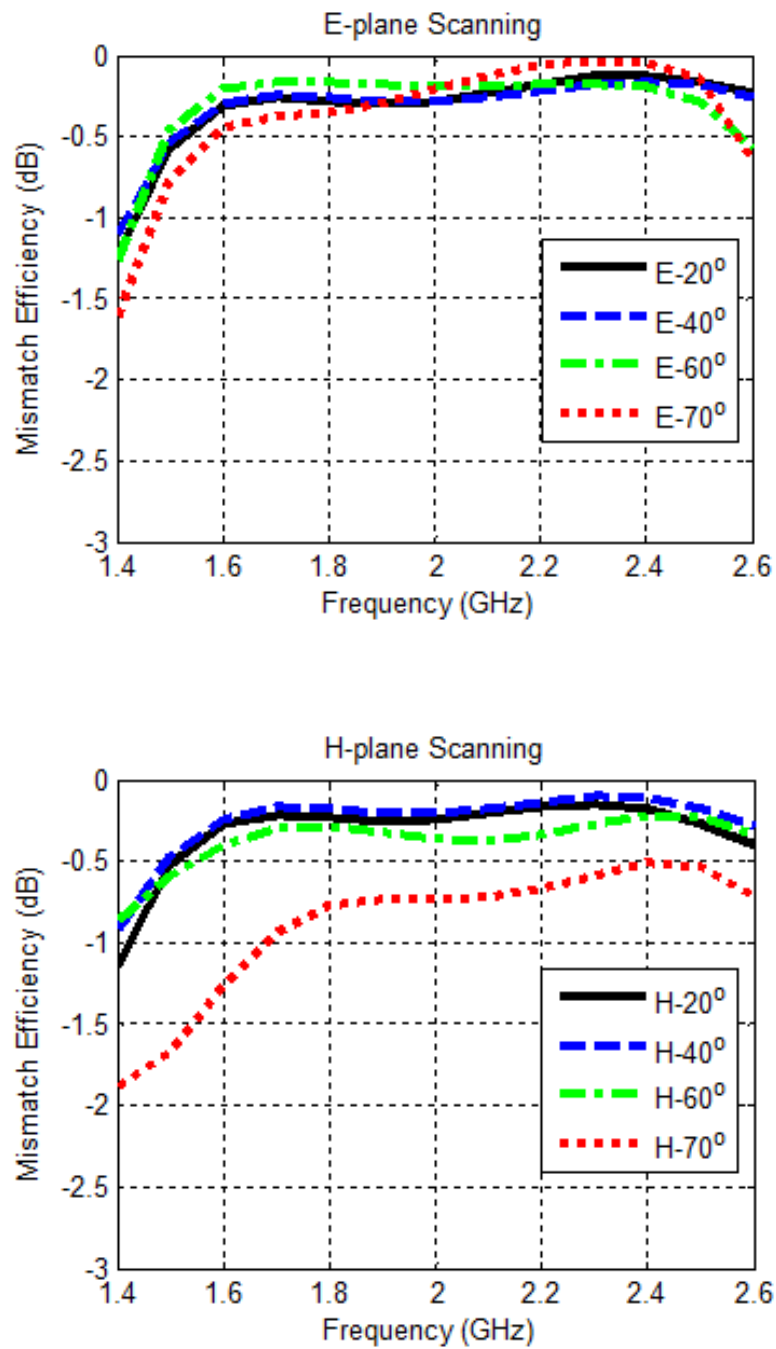


Figure 6.2: Mismatch efficiency of the array in Figure 6.1 during *E* and *H*-plane scanning.

The impedance matching of the infinite array at different scan angles (θ) is shown in Figure 6.2. The mismatch loss is less than 1.5dB for $\theta \leq 70^\circ$ across 1.5-2.5GHz. Although the bandwidth is significantly smaller than the one in Chapter 3, the impedance matching is much better. This makes sure that any issues related to the pattern of a finite aperture employing this design is due to the edge effects and not due to impedance mismatch of each unit-cell. The matching can still be improved by introducing a longer stripline transformer, but the performance is good enough for the scope of Section 6.3.

6.2 Finite Array: Simulation Setup

To determine the size of the array, we assumed a square aperture with 30dBi gain at broadside and at the highest frequency (2.5GHz) of operation. This corresponds to a $9\lambda \times 9\lambda$ aperture, indicating a 20×20 array for our design in Figure 6.1, since its unit-cell size is $0.45\lambda_{high}$. We chose 19×19 active aperture, instead of 20×20 , to have a true central element. However, this geometry is too large and it would take a very long time to do full-wave simulations. Instead, we simulated a semi-infinite array (infinite $\times 19$) to approximate the finite array's performance along a single scan plane.

The semi-infinite array geometry, used for E -plane scanning, is shown in Figure 6.3a. The array is finite along the E -plane (scanning) and infinite along the H -plane (non-scanning). For our case, the number of active and terminated elements are $N=19$ and $M=3$, respectively. The terminated elements have no feed-lines and are loaded by varying termination resistors. For comparison, we also simulated the same TCDA with a dielectric superstrate with $\epsilon_r = 1.7$ (see Figure 6.3b).

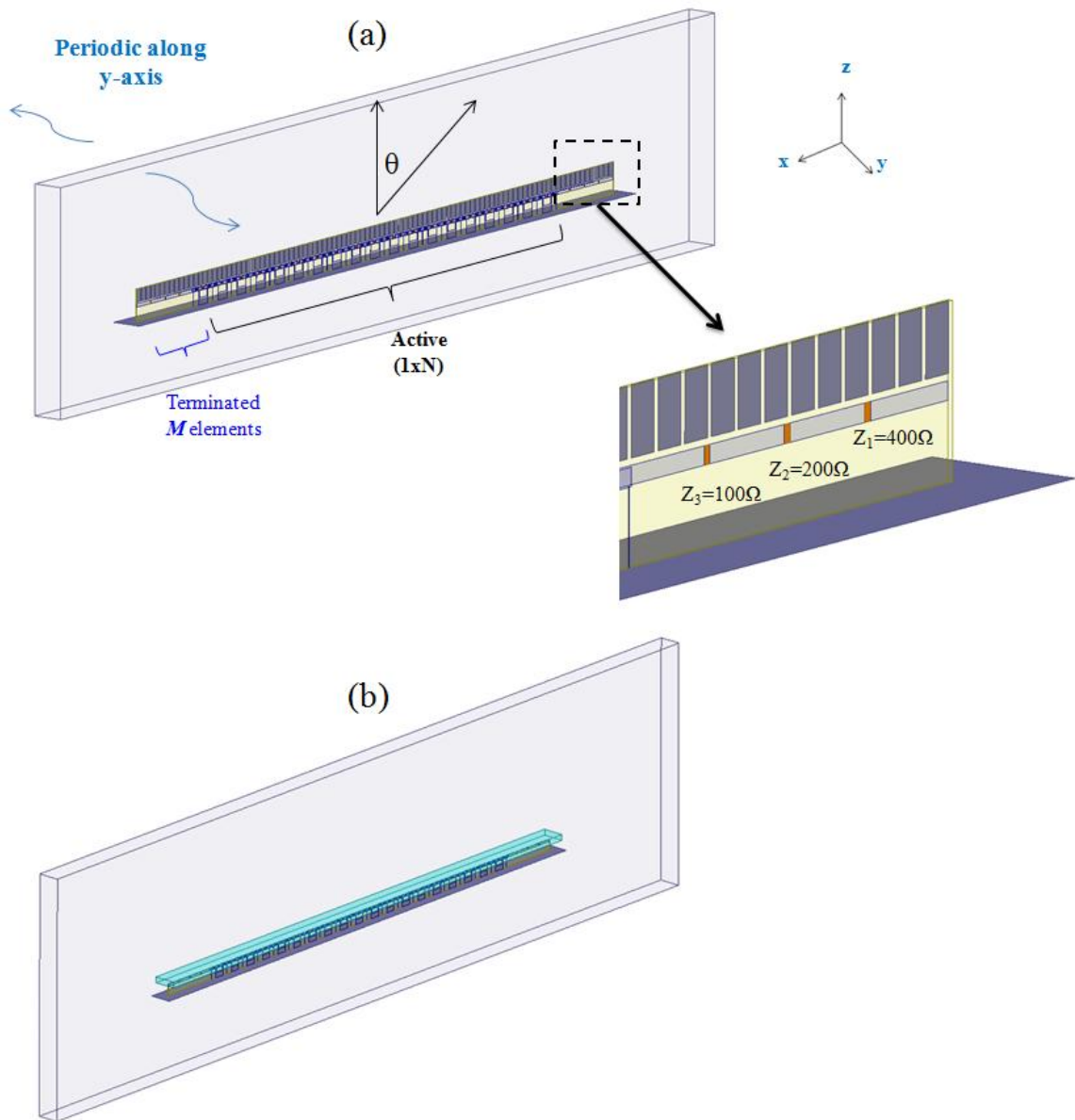


Figure 6.3: Semi-infinite array geometry for the E -plane scanning with (a) FSS superstrate and (b) dielectric superstrate. The array is finite along E -plane (scanning) and infinite along the H -plane (non-scanning).

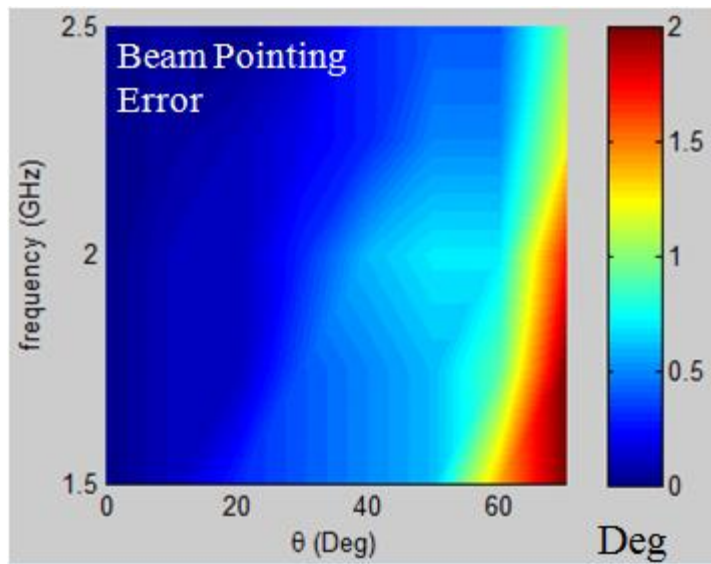
6.3 Simulation Results for Pointing Accuracy: FSS vs Dielectric

The semi-infinite arrays (TCDA with FSS or dielectric) in Figure 6.3 were excited to scan to different elevation angles up to 70° . However, the actual beam direction was slightly different than the intended one for both arrays. This pointing error (or beam squint) increased for larger elevation angles, as expected. We defined this error as follows:

$$\theta_{error} = | \theta_{intended} - \theta_{actual} | \quad (6.1)$$

Based on (6.1), the pointing error of both arrays for $\theta_{intended} \leq 70^\circ$ across 1.5-2.5 GHz is shown in Figure 6.4. It can be seen that there is not much difference between the two arrays. We observe approximately the same performance from the FSS and dielectric loaded arrays for $\theta < 50^\circ$ across the entire frequency range. However, the dielectric-loaded array performs better at higher scan angles, especially for $\theta > 60^\circ$ and for $f > 2.3\text{GHz}$. Based on these results, it seems that the low-contrast dielectric superstrate creates less diffraction at the array edges for very large scan angles, resulting in a smaller pointing error. We note that this may not be an important issue for a well-calibrated radar antenna: If the amount of beam squint is known, then the radiating elements can be phased accordingly to radiate to the exact desired direction. However, the presence of strong edge diffractions (and resulting surface waves) on finite apertures can also cause an increased scattering in the backscatter and bistatic directions [77], which may not be acceptable for certain applications. Therefore, it might be necessary to further suppress/reduce these edge-born waves along the FSS/dipoles, which will be discussed next.

(a) Dielectric Superstrate



(b) FSS Superstrate

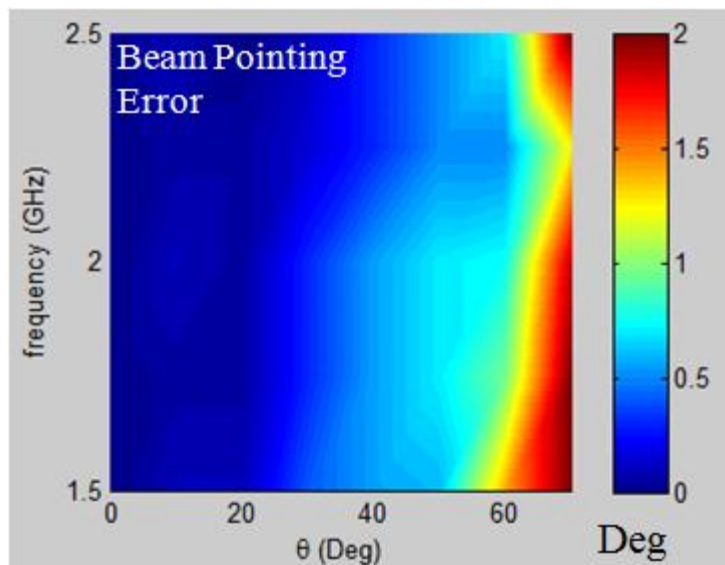


Figure 6.4: Magnitude of the beam pointing error is plotted for semi-infinite TCDAs with (a) dielectric superstrate and (b) FSS superstrate. These plots are obtained for $N=19$ and $M=3$ (see Figure 6.3)

6.4 Modified FSS with Resistive Terminations for Surface Wave Suppression

In the previous section, it was shown that at the very high end of the frequency band, the dielectric superstrate performed better for scan angles beyond 50° in terms of beam accuracy. In this section, we introduce a new FSS geometry to address this issue. Specifically, we replace the FSS of Figure 6.1 with a new one that can be resistively loaded at the aperture edges. This way, excessive diffraction introduced by the FSS can be suppressed more effectively and the beam accuracy can be improved.

The unit-cell geometry is shown in Figure 6.5. The only difference between Figure 6.1 and Figure 6.5 is the superstrate layer. The FSS with vertical stubs was replaced by FSS formed by two layers of small parasitic dipoles. From now on, this modified FSS will be

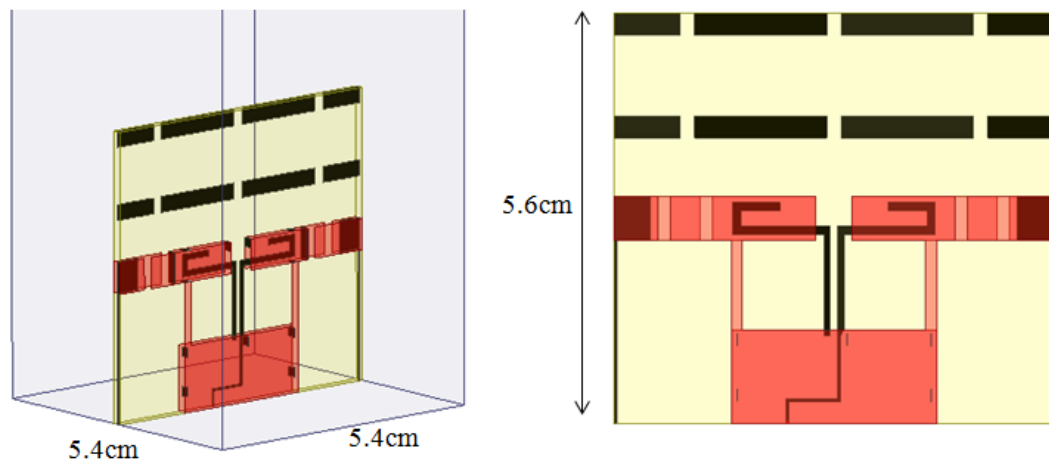


Figure 6.5: Unit cell of the TCDA with FSS-v2 This design is only different than the previous one shown in Figure 6.1 in terms of superstrate.

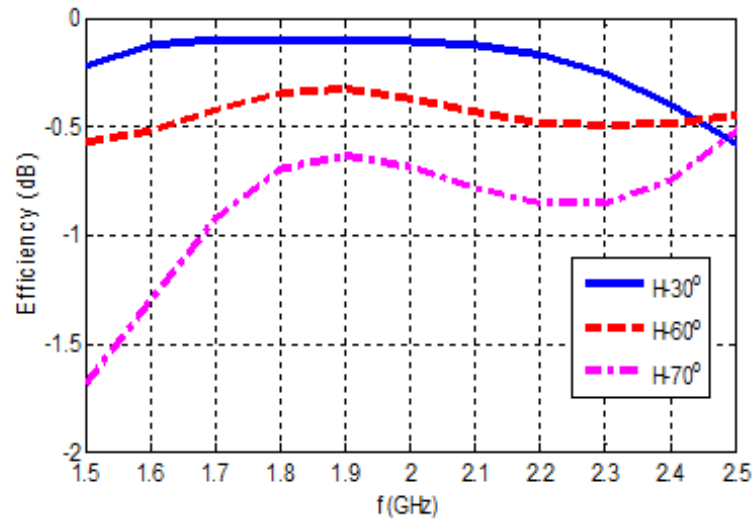
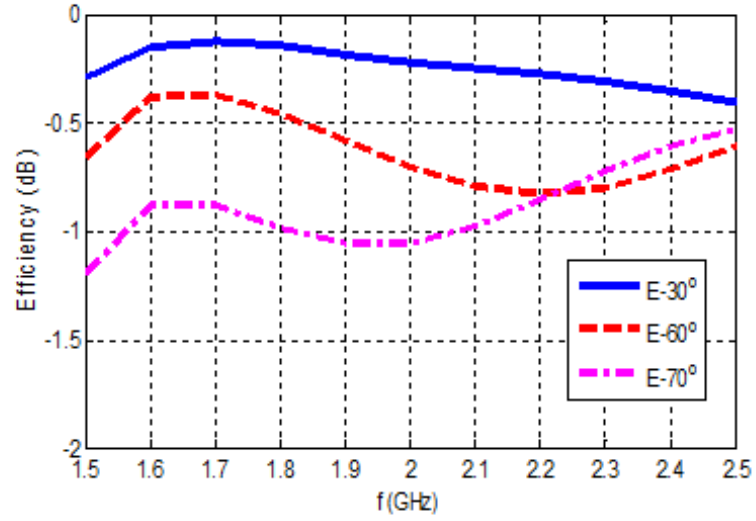


Figure 6.6: Efficiency of the array from Figure 6.5 during *E* and *H*-plane scanning.

referred to as FSS-v2. The unit-cell size and other design parameters are very similar to the previous FSS-array. The efficiency values up to 70° scan angle are depicted in Figure 6.6. As can be seen, the mismatch loss is less than 1.5dB for the frequency band of interest. We also note that FSS-v2 is formed by small dipoles that are suitable to be loaded with lumped resistors (e.g. surface mount or thin film). This can help to suppress the diffracted waves from the superstrate edges.

The semi-infinite array for the TCDA with FSS-v2 is shown in Figure 6.7. The active and terminated portions of the aperture are again 19 and 3 unit-cell long ($N=19$, $M=3$), respectively. The FSS-v2 is extended about 2 unit-cells after the active part of the aperture and terminated resistively in a tapered manner. We note that the parasitic dipoles forming FSS-v2 should be printed on the outer layers, rather than middle layer of the PCB. This facilitates the termination with surface mount resistors.

The plot for beam accuracy of the TCDA with FSS-v2 is shown in Figure 6.8, together with the dielectric superstrate as a comparison. It can be seen that the array with FSS-v2 has lower beam pointing error for $\theta \leq 50^\circ$ across the lower half of the frequency band and for $\theta \leq 60^\circ$ across the upper half of the frequency band. The dielectric superstrate still seems to be better for $\theta > 60^\circ$. However, we note that the FSS-v2 superstrate only extends 2 unit-cells from the active aperture. If the termination length of the FSS-v2 is increased, the scan area of improved performance can be also increased. The drawback for this is mostly practical. There are 6 parasitic dipoles in every unit cell, indicating 6 additional lumped resistors are required to terminate FSS-v2 of each unit-cell. Another concern might be additional loss due to the resistive loading of the FSS-v2. Fortunately,

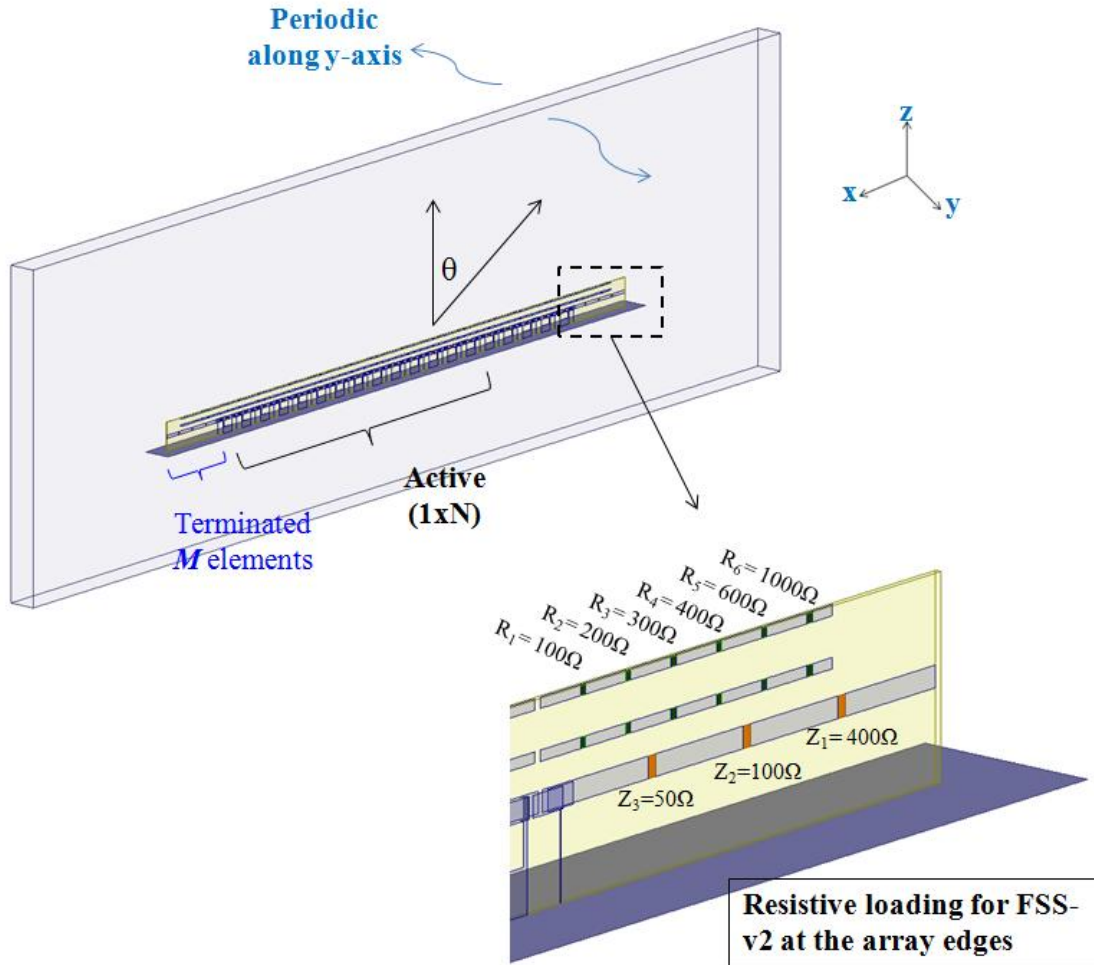
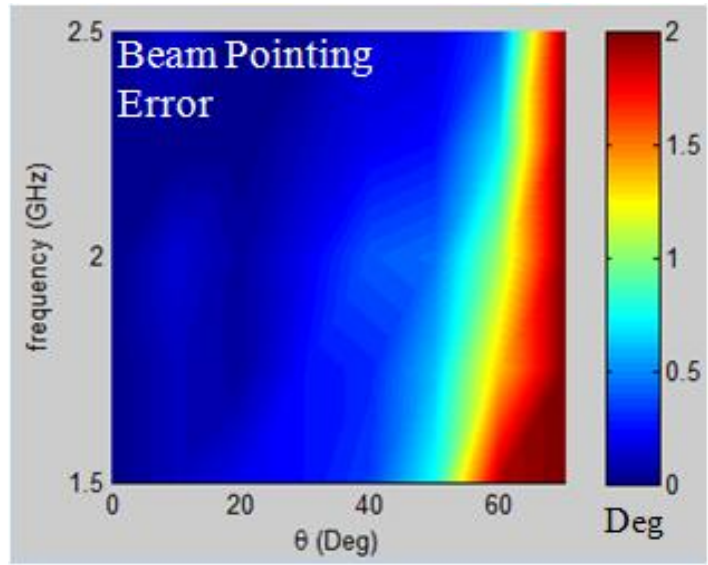


Figure 6.7: Semi-infinite array geometry of TCDA with FSS-v2. The active and parasitic dipoles at the array edges are loaded with resistors.

we found that the ohmic losses due to the loaded FSS-v2 in Figure 6.7 are less than 0.3dB, which occurs at 1.5GHz and $\theta = 70^\circ$. The average value across the whole bandwidth and scan area is less than 0.2dB, indicating that the resistively loaded portion of the FSS can be further increased without excessive loss. As noted before, the only issues are cost and size. Therefore, a trade-off between cost and performance should be made to determine how many terminated elements are acceptable.

(a) FSS-v2 Superstrate



b) Dielectric ($\epsilon_r = 1.7$) Superstrate

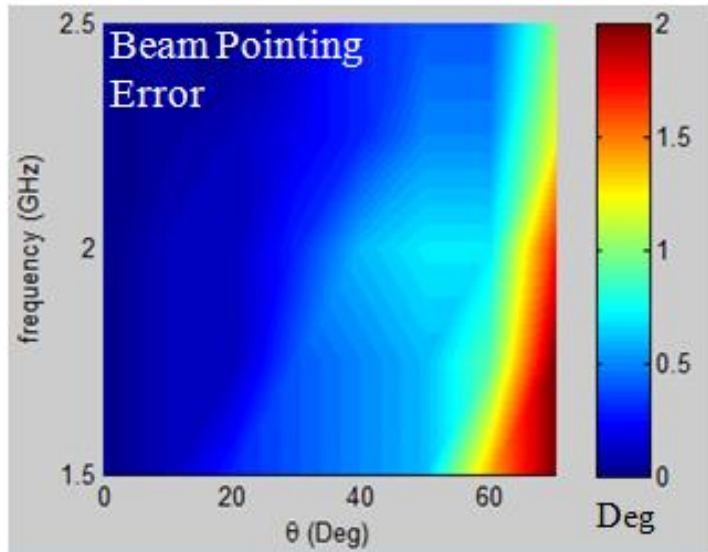


Figure 6.8: Beam pointing error for the semi-infinite array of TCDA with (a) FSS-v2 and (b) dielectric superstrate. The error values are plotted for $N=19$ and $M=3$ (see Figure 6.7)

The scanning patterns of the semi-infinite array with FSS-v2 are depicted in Figure 6.9, across 1.5-2.5GHz for $\theta \leq 60^\circ$. The array is uniformly excited with resistive terminations as described before (see Figure 6.7). The side lobe levels are less than -12dB across the whole scan area and frequency bandwidth. For smaller scan angles, side lobes are actually around -14dB. Excellent beam accuracy is observed for the whole scan range of $\theta \leq 60^\circ$.

6.5 Summary

In this chapter, finite arrays of moderate sizes (e.g. 30dBi gain) were studied. TCDAs using dielectric-loading were compared with TCDAs having different FSS superstrates. It was found that the FSS structure introduced in Chapter 3.2 were slightly outperformed by a dielectric superstrate in terms of beam pointing accuracy at scan angles beyond 50° .

To address the beam accuracy issue for large angles, another printed superstrate (FSS-v2) was introduced. FSS-v2 was formed by two layers of small parasitic dipoles, oriented horizontally across the array aperture. These were particularly suited for resistive termination and were shown to improve beam pointing accuracy for $\theta \leq 60^\circ$ with two dummy unit-cells at the aperture edges. The resistive loss due to these terminations were minimal (~ 0.2 dB), indicating additional terminated elements can be used without any excessive ohmic losses.

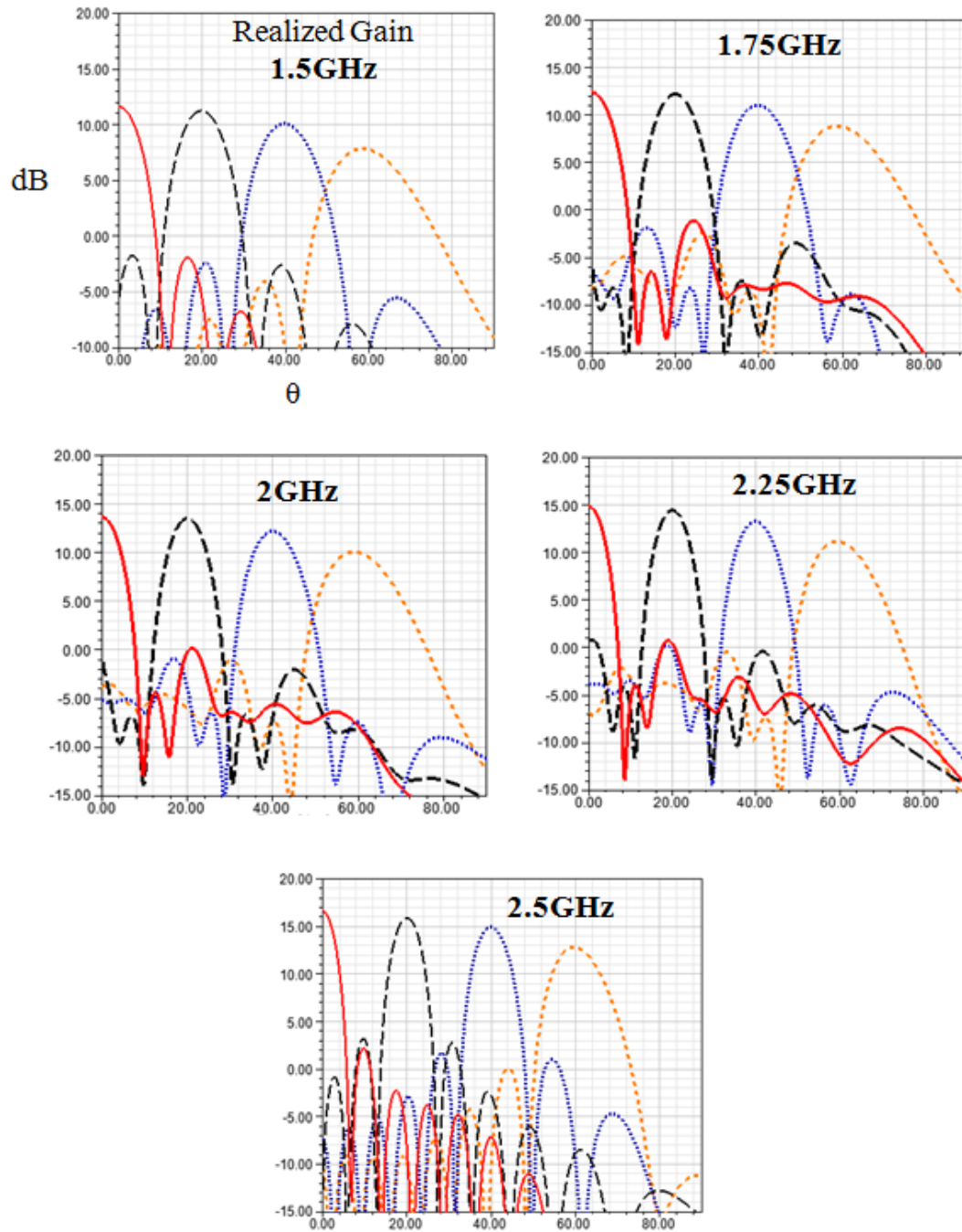


Figure 6.9: *E*-plane scanning patterns of the array of Figure 6.7 for $\theta \leq 60^\circ$

Chapter 7 Conclusions and Future Work

7.1 Summary of This Work

In the first chapter of this work, we discussed the motivation and challenges for wideband and wide-angle scanning antenna arrays. The two major problems were reviewed; surface wave and varying scan impedance. Narrow band and wideband antenna designs addressing these problems were studied. Connected arrays, tightly coupled arrays (TCA) in particular, were found to be most effective in designing apertures with low profile, large bandwidth and wide scan area.

In Chapter 2 we discussed tightly coupled dipole arrays (TCDA) in more detail. We reviewed a recently proposed analytical model [39]. We also compared this model to a more popular approximate (L - C) model [35] and verified that for tight coupling between neighboring elements, there are no significant differences. As noted before, these analytical approaches ignore vertically placed feed-lines inside the array volume. This is in fact the main limiting factor for such models. We compared full-wave simulations with the analytical model of an array with a realistic feed geometry. The effect of feed-lines for different scanning conditions was studied. We verified that the analytical model's accuracy starts to degrade when the electric field of the fundamental Floquet mode has

component parallel to the aperture normal (TM modes). In other words, the analytical approaches can be used for arrays with feed-lines but only for broadside or H -plane scanning (not for E -plane), unless vertical feed-lines are also accounted for in such models, which is not a trivial problem.

In Chapter 3, we discussed the potential of frequency selective surfaces in wide-scan antenna array designs. As mentioned in Chapter 1, most arrays use simple isotropic dielectric slabs above the array aperture for wide angle impedance matching. We introduced a simple, yet effective printed FSS geometry to replace the dielectric superstrates. The proposed FSS can be fabricated on the same PCB with the dipole and feed-lines, resulting in a low-cost, light weight design. To feed the array efficiently, we also introduced a modified Marchand balun with perforated ground planes. Overall, the proposed FSS loaded array with the new balun achieved more than $>6:1$ impedance bandwidth for $VSWR < 3.2$. The maximum scan angles (θ) were: 75° in E -plane, 70° in D -plane and 60° in H -plane.

Chapter 4 presented the fabrication and measurement procedure of a 12×12 prototype, based on the design from Chapter 3. Extensive gain and pattern measurements verified the simulated performance of the FSS loaded TCDA.

In Chapter 5, we presented a dual-polarized TCDA that utilized the modified Marchand balun. Our focus was on the challenges due to the coupling between cross-polarized elements, which was the main problem when designing dual-polarized arrays. It was found that a low-frequency resonance (like the one in [42]) was the limiting factor for the impedance bandwidth, even when balanced feed-lines were used. Based on this

limitation, we estimated $\sim 5.5:1$ maximum bandwidth. We actually achieved $4.5:1$ when scanning to $\theta \leq 60^\circ$ in H -plane and $\theta \leq 70^\circ$ in E and D -plane. We also showed that this bandwidth did not change significantly when the dielectric slab was replaced by the FSS superstrate introduced in Chapter 3, since the feed geometry was the main limitation.

In Chapter 6, we studied finite arrays with moderate sizes (e.g. 30dBi gain). Via full-wave simulations, we compared the different FSS superstrates to a low contrast ($\epsilon_r = 1.7$) dielectric superstrate. The performance metric was the beam pointing accuracy of the finite array. The FSS, introduced in Section 3.2, performed similar to dielectric for $\theta \leq 50^\circ$. However, the dielectric superstrate outperformed the FSS for larger scan angles, especially at the higher end of the band. To address the beam accuracy problem of the FSS, we proposed a new superstrate design, formed by small parasitic dipoles (FSS-v2). The latter had a suitable geometry for resistive termination. We applied a tapered resistive loading along the FSS-v2 for two unit-cells at the array edges. As a result, the FSS loaded array outperformed the dielectric for $\theta \leq 50^\circ$ at the lower half and $\theta \leq 60^\circ$ at the upper half of the frequency bandwidth. This indicates that using 3 or 4 dummy elements at the edges can give enough termination length for the resistively loaded FSS to outperform the dielectric across the whole bandwidth within the $\pm 60^\circ$ scan area.

7.2 Future Work

In this work, we showed the potential of FSS superstrates for improving scan range of tightly coupled dipole arrays (TCDA). Practical implementations of feeding geometries were also provided. However, there is still a wide range of opportunities for future research, regarding similar wide-angle arrays. Some of them are listed as following:

7.2.1 Fast Optimization of TCDAs

The proposed arrays in this work were designed and initially optimized in the full-wave domain. Then the feed-lines were designed using circuit simulators. Since the circuit simulations are much faster, the bulk of the overall optimization time is due to full-wave simulations. Therefore, moving any part of the design process into circuit simulations is highly desirable. One approach to achieve this is described in Figure 7.1. Almost all capacitively coupled parts of the full-wave model can be loaded with gap sources to extract the multi-port representation of the array into a circuit simulator. Then, the dipole coupling, FSS loading, open stub etc. can be tuned in circuit simulators, instead of full-wave domain, resulting in a much faster optimization.

7.2.2 Increasing Impedance Bandwidth of Dual-Polarized Dipole Arrays

As we noted earlier, a dual polarized TCDA with a practical, lossless feed (e.g. Marchand balun) has a potential of $\sim 5.5:1$ bandwidth due to a low frequency resonance, when the substrate region is air ($\epsilon_r = 1$). For arrays with dielectric loading in the substrate, this limit can be pushed to $6:1$ [43]. However, dielectric loading in this region is usually a limiting factor for large scan angles and should be avoided if possible. Therefore, a novel feeding scheme is needed for dual-polarized TCDAs to achieve $>6:1$ impedance bandwidth and $>60^\circ$ scan angle.

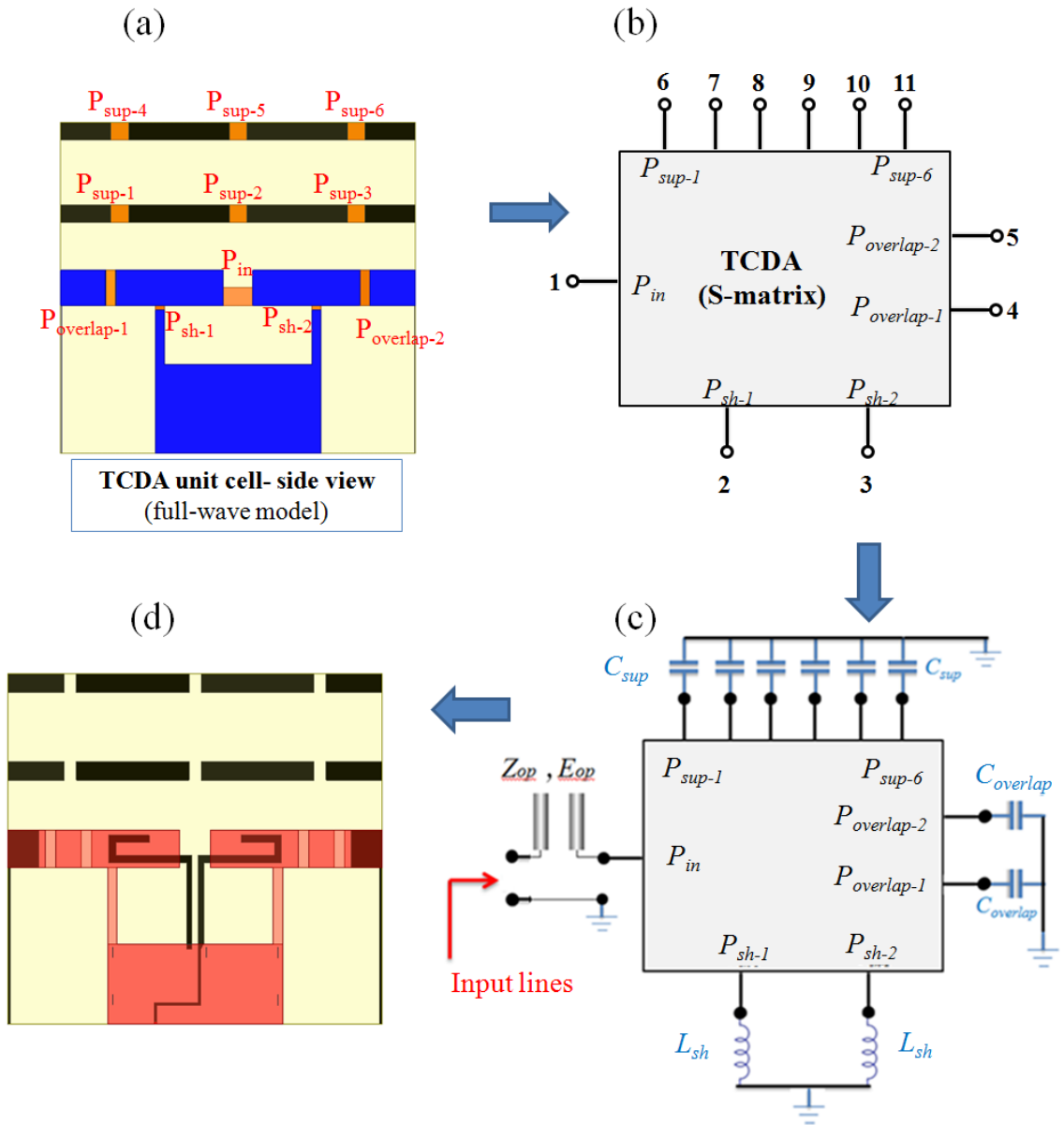


Figure 7.1: Suggested design process for faster optimization of TCDA. (a) Initial full-wave model, loaded with lump ports (b) Extracted S-parameters of the full-wave model (c) Tuning of the array by capacitive or inductive terminations, except the input, using a circuit simulator. (d) Implementation & validation of the optimized design via full-wave simulations. For simplicity, we excluded feed-lines from (a), (b) and (c)

7.2.3 FSS Designs for mm-Wave

The arrays shown in Chapter 3 and Chapter 5 are suitable for working below 10 GHz. The FSS loaded array in Section 6.1 can be scaled to higher frequencies (~20 GHz) due to the modified feed. For even higher frequencies, both feed lines and FSS should be changed since fully planar/conformal PCB layers are typically the most practical implementations for mm-Wave applications. Therefore, both the feed-lines and the vertical FSS should be implemented using embedded vias. Additional challenges due to dielectric loading, limited number of printed layers and fabrication tolerances should also be addressed.

7.2.4 Reducing Aperture Density

It is well-known that most wideband arrays have unit-cell sizes of $<0.5\lambda$ at the highest frequency of operation. This implies extremely dense arrays at lower end of the band. As an example, consider an array of 7:1 bandwidth with unit-cell size of $0.45\lambda_h$. Due to the large bandwidth, the unit-cell size becomes 0.065λ at the lowest frequency. A non-uniform distribution of unit-cell sizes along the aperture can help to minimize the number of feeding points (T/R modules). However, this type of array thinning can be quite challenging for wideband, wide scan arrays since increasing element spacing and improving bandwidth are typically opposing phenomena. Another option might be an adaptive feed network to dynamically switch some of the elements ON/OFF depending on the frequency and scan angle of operation, potentially reducing the total number of active elements at a time.

Bibliography

- [1] G. C. Tavik, C. L. Hilterbrick, J. B. Evins, J. J. Alter, J. G. Crnkovich Jr, J. W. de Graaf, W. Habicht II, G. P. Hrin, S. A. Lessin, D. C. Wu, S. M. Hagedwood, "The advanced multifunction RF concept," *IEEE Trans. Microw. Theory Tech.*, vol. 53, no. 3, pp.1009-1020, March 2005.
- [2] D. Update. (2009) "EL/M-2248 MF-STAR naval multi-mission radar," [Online]. Available: <http://defense-update.com/directory/mf-star.htm>.
- [3] M. T. Frankford, N. Majurec, and J. T. Johnson, "Software-defined radar for MIMO and adaptive waveform applications," *IEEE Radar Conference*, pp. 724-728, May 2010.
- [4] P. S. Hall, P. Gardner and A. Faraone, "Antenna requirements for software defined and cognitive radios," *Proceedings of the IEEE*, vol. 100, pp. 2262-2270, July 2012.
- [5] S. Kandeepan, L. De Nardis, M. Di Benedetto, A. Guidotti and G. E. Corazza, "Cognitive satellite terrestrial radios," *IEEE Global Telecommunications Conference (GLOBECOM)*, pp. 1-6, Dec. 2010.
- [6] D. S. Zrnic, J. F. Kimpel, D. E. Forsyth, A. Shapiro, G. Crain, R. Ferek, J. Heimmer, W. Benner, T. J. McNellis, and R. J. Vogt, "Agile-beam phased array radar for weather observations," *Bull. Amer. Meteor. Soc.*, vol. 88, no. 11, pp. 1753–1766, Nov. 2007.
- [7] J. Herd , D. Carlson, S. Duffy, M. Weber, G. Brigham, M. Rachlin, D. Cursio, C. Liss and C. Weigand, "Multifunction phased array Radar (MPAR) for aircraft and weather surveillance," *IEEE Radar Conference*, pp. 945-948, May 2010.
- [8] J. J. Lee, "Ultra wideband arrays," in *Antenna Engineering Handbook*, 4th ed., J. L. Volakis, Ed. McGraw Hill Professional, 2007.
- [9] R. Hendrix, "Aerospace system improvements enabled by modern phased array radar," *Northrup Grumman white paper*, 2002.

- [10] H. A. Wheeler, "Simple relations derived from a phased-array antenna made of an infinite current sheet," *IEEE Trans. Antennas Propag.*, vol. 13, no. 4, pp. 506–514, 1965.
- [11] D. M. Pozar and D. H. Schaubert, "Scan blindness in infinite phased arrays of printed dipoles," *IEEE Trans. Antennas Propag.*, vol. 32, no. 6, pp. 602 – 610, June 1984.
- [12] P. W. Hannan and S. P. Litt, "Capacitive ground plane for a phased-array antenna," *IEEE Antennas Propag. Soc. Int. Symp.*, vol.6, pp. 115-123, Sept. 1968.
- [13] R. F. Harrington, "Plane wave functions" *Time-Harmonic Electromagnetic Fields*, McGraw-Hill, 1961, ch. 4, pp. 143-186.
- [14] A. Hessel and G. H. Knittel, "A loaded ground plane for the elimination of blindness in a phased-array antenna," *IEEE Antennas Propag. Soc. Int. Symp.*, vol. 7, pp. 163-169, Dec. 1969.
- [15] S. Edelberg and A. A. Oliner, "Mutual coupling effects in large antenna arrays II: Compensation effects," *IRE Trans. Antennas Propag.*, vol. 8, no. 4, pp. 360 – 367, Sept. July 1960.
- [16] P. W. Hannan, D. S. Lerner and G. H. Knittel, "Impedance matching a phased-array antenna over wide scan angles by connecting circuits," *IEEE Trans. Antennas Propag.*, vol. 13, no. 1, pp. 28 – 34, Jan. 1965.
- [17] E. G. Magill and H. A. Wheeler, "Wide-angle impedance matching of a planar array antenna by a dielectric sheet," *IEEE Trans. Antennas Propag.*, vol. 14, no. 1, pp. 49 – 53, Jan. 1966.
- [18] B. A. Munk, T. W. Kornbau and R. D. Fulton, "Scan independent phased arrays," *Radio Science*, vol. 14, no. 6, pp. 979 – 990, Nov. 1979.
- [19] S. D. Targonski, R. B. Waterhouse and D. M. Pozar, "Design of wide-band aperture-stacked patch microstrip antennas", *IEEE Trans. Antennas Propag.*, vol. 46, pp.1245 -1250, 1998.
- [20] L. Infante, A. De Luca and M. Teglia, "Low-profile ultra-wide band antenna array element suitable for wide scan angle and modular subarray architecture", *Proc. IEEE Phased Array Systems and Technology (ARRAY)*, pp.157 -163, Oct. 2010.
- [21] R. Erickson, R. Gunnarsson, T. Martin, L. G. Huss, L. Pettersson, P. Andersson and A. Ouacha, "Wideband and wide scan phased array microstrip patch antennas for small platforms," *European Conference on Antennas & Propagation (EuCAP)*, Nov. 2007.

- [22] M. J. Povinelli, "Wideband dual polarized apertures utilizing closely spaced printed circuit flared slot antenna elements for active transmit and receive phased array demonstration," in *Proc. Antenna Applicat. Symp.*, Allerton Park, IL, 1989.
- [23] D. H. Schaubert, S. Kasturi, A. O. Boryssenko and W. M. Elsallal, "Vivaldi antenna arrays for wide bandwidth and electronic scanning," *European Conference on Antennas & Propagation (EuCAP)*, Nov. 2007.
- [24] R. W. Kindt and W. R. Pickles, "Ultrawideband all-metal flared-notch array radiator," *IEEE Trans. Antennas Propag.*, vol. 58, no. 11, pp. 3568 - 3575, Sept. 2010
- [25] H. Holter, "Dual-polarized broadband array antenna with BOR- elements, mechanical design and measurements," *IEEE Trans. Antennas Propag.*, vol. 55, no. 2, Feb. 2007.
- [26] R. W. Kindt and D. Taylor, "Polarization correction in dual-polarized phased arrays of flared notches," *Proc. IEEE Antennas Propag. Soc. Int. Symp.*, July 2011.
- [27] J. J. Lee, S. Livingston, and R. Koenig, "A low-profile wide-band (5:1) dual-pol array," *IEEE Antennas Wireless Propag. Lett.*, vol. 2, pp. 46-49, 2003.
- [28] M. W. Elsallal and J. C. Mather, "An ultra-thin, decade (10:1) bandwidth, modular BAVA array with low cross-polarization," in *Proc. IEEE Antennas Propag. Soc. Int. Symp.*, pp. 1980-1983, July 2011.
- [29] C. E. Baum, "Some characteristics of planar distributed sources for radiating transient pulses," *Sensor and Simulation Note 100*, Mar. 1970.
- [30] A. Neto and J. J. Lee, "Infinite bandwidth long slot array antenna," *IEEE Antennas Wireless Propag. Lett.*, vol. 4, pp. 75-78, 2005.
- [31] A. Neto and J. J. Lee, "Ultrawideband properties of long slot arrays," *IEEE Trans. Antennas Propag.*, vol. 54, no. 2, pp. 534-543, Feb. 2006.
- [32] J.J. Lee, S. Livingston, R. Koenig, D. Nagata, and L. L. Lai, "Compact light weight UHF arrays using long slot apertures," *IEEE Trans. Antennas Propag.*, vol. 54, no. 7, Jul. 2006.
- [33] J. J. Lee, S. Livingston, and D. Nagata, "A low profile 10:1 (200-2000) wide band long slot array," *Proc. IEEE Antennas Propag. Soc. Int. Symp.*, Jul. 5-11, 2008.
- [34] B. Munk, R. Taylor, T. Durham, W. Crosswell, B. Pigon, R. Boozer, S. Brown, M. Jones, J. Pryor, S. Ortiz, J. Rawnick, K. Krebs, M. Vanstrum, G. Gothard and D. Weibelt, "A low-profile broadband phased array antenna," in *Proc. IEEE Antennas Propag. Soc. Int. Symp.*, Jun. 2003, vol. 2, pp. 448-451.

- [35] B. A. Munk, "Broadband wire arrays," in *Finite Antenna Arrays and FSS*, 1st ed. Wiley-IEEE Press, Jul. 2003, ch. 6, pp. 181-213.
- [36] ———, *Frequency Selective Surfaces: Theory and Design*, 1st ed. Wiley-Interscience, Apr. 2000.
- [37] M. Jones and J. Rawnick, "A new approach to broadband array design using tightly coupled elements," in *MILCOM 2007 - IEEE Military Communications Conference*, pp. 1-7, Oct. 2007.
- [38] J. P. Doane, "Wideband low-profile antenna arrays: Fundamental limits and practical implementations," Ph.D. dissertation, The Ohio State University, 2013.
- [39] D. Cavallo, "Connected array antennas: Analysis and design," Ph.D. dissertation, Technische Universiteit Eindhoven, 2011.
- [40] S. S. Holland and M. N. Vouvakis, "The banyan tree antenna array," *IEEE Trans. Antennas Propag.*, vol. 59, no. 11, pp. 4060-4070, Nov. 2011.
- [41] ———, "The planar ultrawideband modular antenna (PUMA) array," *IEEE Trans. Antennas Propag.*, vol. 60, no. 1, pp. 130-140, Jan. 2012.
- [42] S. S. Holland, "Low-profile, modular, ultra-wideband phased arrays" PhD dissertation, University of Massachusetts Amherst, 2011.
- [43] J. Logan, "A new class of improved bandwidth planar ultrawideband modular antenna (PUMA) arrays scalable to mm-waves," Masters Thesis, University of Massachusetts Amherst, 2013.
- [44] J. B. Muldavin, T. J. Ellis, and G. M. Rebeiz, "Tapered slot antennas on thick dielectric substrates using micromachining techniques," *Proc. IEEE Antennas Propag. Soc. Int. Symp.*, Jun. 1997.
- [45] J. A. Kasemodel, C.C. Chen, J. L. Volakis, "Wideband planar array with integrated feed and matching network for wide-angle scanning", *IEEE Trans. Antennas Propag.*, vol. 61, no. 9, pp. 4528 – 4537, Sept. 2011.
- [46] J. P. Doane, K. Sertel and J. L. Volakis, "A wideband, wide scanning tightly coupled dipole array with integrated balun (TCDA-IB)", *IEEE Trans. Antennas Propag.*, vol. 61, no. 9, pp. 4538 – 4548, Sept. 2013.
- [47] N. Marchand, "Transmission-line conversion transformers", *Electronics*, vol. 17, pp. 142-146, Dec. 1944.

- [48] W. F. Moulder, K. Sertel and J. L. Volakis, "Ultrawideband superstrate enhanced substrate loaded array with integrated feed," *IEEE Trans. Antennas Propag.*, vol. 61, no. 11, pp. 5802 – 5807, Aug. 2013.
- [49] J. J. Schuss and J. D. Hanfling, "Nonreciprocity and scan blindness in phased arrays using balanced-fed radiators," *IEEE Trans. Antennas Propag.*, vol.35, no.2, pp.134-138, Feb. 1987.
- [50] J. G. Maloney, B. N. Baker, R. T. Lee, G. N. Kiesel and J. J. Acree , "Wide scan, integrated printed circuit board, fragmented aperture array antennas," *Proc. IEEE Antennas Propag. Soc. Int. Symp.*, July 2011.
- [51] B. Riviere, H. Jeuland, S. Bolioli, B. Gabard and V. Gobin, "Ultrawideband multilayer printed antenna arrays with wide scanning capability," *IEEE Antennas Propag. Soc. Int. Symp.*, July 2015.
- [52] I. Tzanidis, K. Sertel, and J. L. Volakis, "Interwoven spiral array (ISPA) with a 10:1 bandwidth on a ground plane," *IEEE Antennas Wireless Propag. Lett.*, vol. 10, pp. 115-118, 2011.
- [53] H. Steyskal, J. Ramprecht, and H. Holter, "Spiral elements for broad-band phased arrays," *IEEE Trans. Antennas Propag.*, vol. 53, no. 8, Aug. 2005.
- [54] M. H. Novak, J. L. Volakis, "Ultrawideband antennas for multiband satellite communications at UHF-Ku frequencies," *IEEE Trans. Antennas Propag.*, vol. 63, no. 4, pp. 1334-1341, April 2015.
- [55] D. Cavallo, A. Neto, and G. Gerini, "Green's function based equivalent circuits for connected arrays in transmission and in reception," *IEEE Trans. Antennas Propag.*, vol. 59, no. 5, pp. 1535-1545, May 2011.
- [56] *Ansys HFSS 15.0*, <http://www.ansys.com/>
- [57] J. L. Volakis, A. Chatterjee and L. C. Kempel, *Finite Element Methods for Electromagnetics: Antennas, Microwave Circuits and Scattering Applications*, 1st ed. Wiley-Interscience, June 1998.
- [58] J. -F. Lee, R. Lee, V. Rawat, K. Sertel, and F. L. Teixeira, "Numerical methods in antenna modeling," in *Frontiers in Antennas: Next Generation Design and Engineering*, F. B. Gross, Ed. McGraw Hill Professional, 2011, ch.11, pp. 443-502.
- [59] D. Cavallo, A. Neto and G. Gerini, "Analytical description and design of printed dipole arrays for wideband wide-scan applications," *IEEE Trans. Antennas Propag.*, July 2012.

- [60] D. Cavallo, A. Neto, G. Gerini and F. Smits, "Connected arrays of dipoles for broad band, wide angle scanning, dual polarized applications: A novel solution to the common mode problem," *IEEE Int. Sym. Phased Array Systems and Technology*, pp. 906-910, Oct. 2010.
- [61] A. Ludwig, "The definition of cross polarization," *IEEE Trans. Antennas Propag.*, vol. 21, no. 1, pp. 116–119, Jan. 1973.
- [62] H. Holter and H. Steyskal, "On the size requirement for finite phased-array models," *IEEE Trans. Antennas Propag.*, vol.50, no.6, pp.836-840, June 2002.
- [63] *ETS-Lindgren Dual Polarized Horn, Model 3164-03*, user manual available at <http://www.ets-lindgren.com/manuals/3164-04.pdf>.
- [64] *8 way-0° Power Splitter/Combiner*, part number ZN8PD1-53+, datasheet available at <http://www.minicircuits.com/pdfs/ZN8PD1-53+.pdf>.
- [65] *ECCOSTOCK® LoK*, <http://www.eccosorb.com/products-eccostock-lok.htm>.
- [66] *Agilent ADS 2012.08*, <http://www.keysight.com/en/pd-2151427/ads-2012-product-release?cc=US&lc=eng>.
- [67] D. F. Kelley and W. L. Stutzman, "Array antenna pattern modeling methods that include mutual coupling effects," *IEEE Transactions on Antennas and Propagation*, vol. 41, no. 12, pp. 1625-1632, 1993.
- [68] W. E. Kock, "Metallic delay lenses," *Bell Syst. Tech. J.*, vol. 27, no. 1, pp. 58–82, Jan. 1948.
- [69] J. Brown, "The design of metallic delay dielectrics," *Proc. IEE*, vol. 97, no. 45, pt. 3, pp. 45-48, Jan. 1950.
- [70] W. H. Syed and A. Neto, "Front to back ratio enhancement of planar printed antennas by means of artificial dielectric layers," *IEEE Trans. Antennas Propag.*, vol. 61, no. 11, pp. 5408-5416, Nov. 2013.
- [71] D. Cavallo, W. H. Syed, and A. Neto, "Closed-form analysis of artificial dielectric layers—Part I: Properties of a single layer under plane-wave incidence," *IEEE Trans. Antennas Propag.*, vol. 62, no. 12, pp. 6256–6264, Dec. 2014.
- [72] ———, "Closed-Form analysis of artificial dielectric layers—Part II: extension to multiple layers and arbitrary illumination," *IEEE Trans. Antennas Propag.*, vol.62, no.12, pp.6265-6273, Dec. 2014.

- [73] B. A. Munk, "Surface waves on passive surfaces of finite extent," in *Finite Antenna Arrays and FSS*, 1st ed. Hoboken, NJ, USA: Wiley-IEEE Press, 2003, ch. 4, pp. 84-135.
- [74] D. S. Janning and B. A. Munk, "Effects of surface waves on the currents of truncated periodic arrays," *IEEE Trans. Antennas Propag.*, vol.50, no.9, pp.1254-1265, Sept. 2002.
- [75] O. A. Civi and P. H. Pathak, "Array guided surface waves on a finite planar array of dipoles with or without a grounded substrate," *IEEE Trans. Antennas Propag.*, vol.54, no.8, pp.2244-2252, Aug. 2006.
- [76] R. C. Hansen, "Linear Connected Arrays," *IEEE Antennas Wireless Propag. Lett.*, vol.3, no.1, pp.154-156, Dec. 2004.
- [77] B. A. Munk, D. S. Janning, J. B. Pryor and R. J. Marhefka, "Scattering from surface waves on finite FSS," *IEEE Trans. Antennas Propag.*, vol. 49, no. 12, pp. 1782-1793, Dec. 2001.